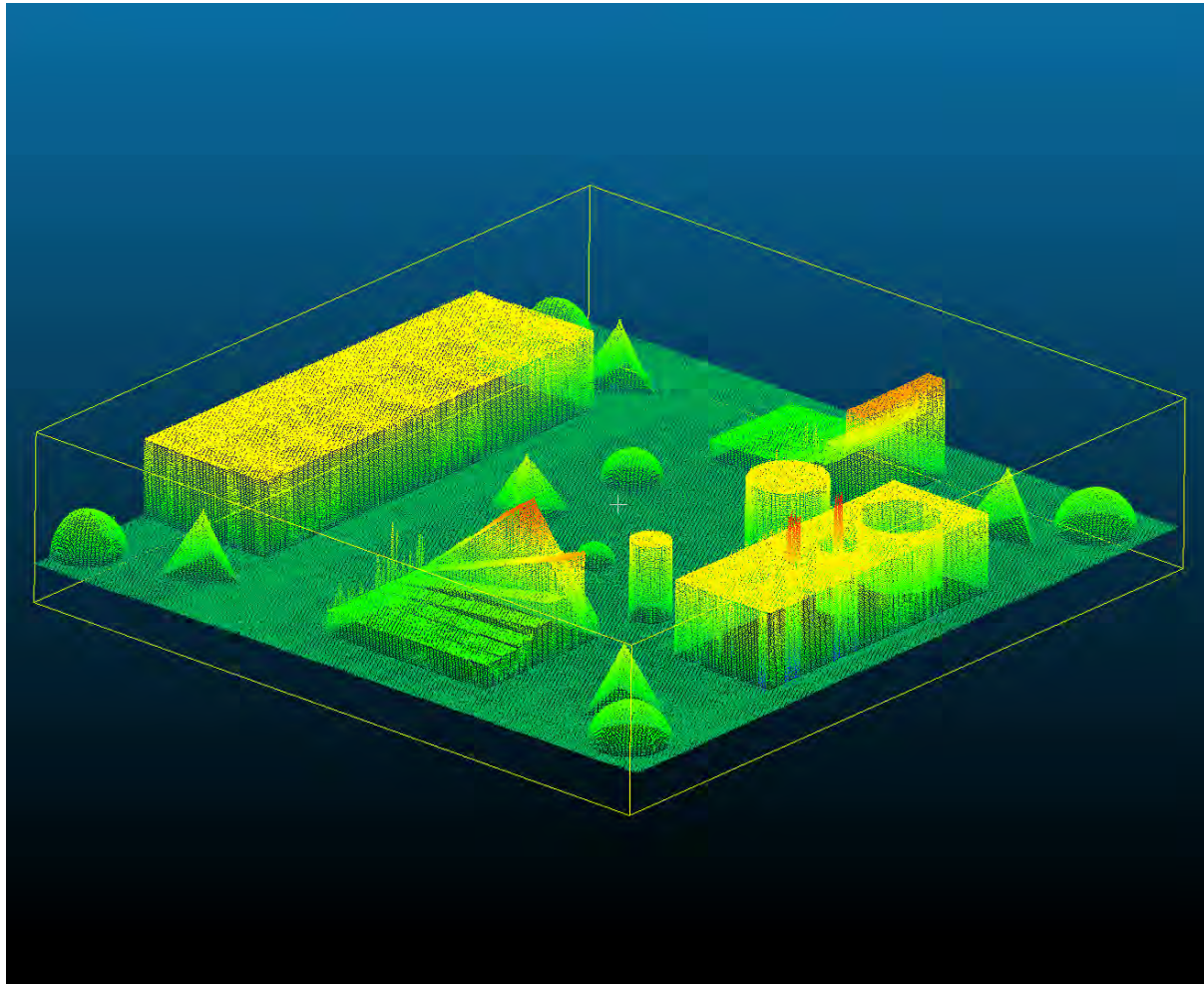


Advancements in Shape-From-Focus Based Profilometry for Additive Manufacturing Metrology

Ing. Jona Gladines



Supervisor **prof. dr. S. Vanlanduit**

Thesis submitted in fulfilment of the requirements for the degree of doctor in applied engineering
Faculty of Applied Engineering | Antwerpen, 2023



Faculty of Applied Engineering

Advancements in Shape-From-Focus Based Profilometry for Additive Manufacturing Metrology

Thesis submitted in fulfilment of the requirements for the degree of
doctor in applied engineering
at the University of Antwerp

Ing. Jona Gladines

Antwerpen, 2023

Supervisor
prof. dr. S. Vanlanduit

Jury

Chairman

prof. dr. R. Penne, University of Antwerp, Belgium

Supervisor

prof. dr. S. Vanlanduit, University of Antwerp, Belgium

Members

dr. Ing. B. Ribbens, University of Antwerp, Belgium

prof. dr. J. Dirckx, University of Antwerp, Belgium

prof. dr. N. Paone, Università Politecnica delle Marche, Italy

prof. dr. H. Haitjema, Katholieke Universiteit Leuven, Belgium

prof. dr. ir. De Baere, Vrije Universiteit Brussel, Belgium

Contact

Ing. Jona Gladines

University of Antwerp

Faculty of Applied Engineering

Invilab

Groenenborgerlaan 171, 2020 Antwerpen, België

M: jona.gladines@uantwerpen.be

T: +32 265 93 66

© 2023 Ing. Jona Gladines

All rights reserved.

Dutch title:

Verbeteringen van profilometrie
gebaseerd op Shape-From-Focus
voor metrologie voor 3D printen

Contents

1	Introduction	7
1.1	Dimensional metrology	7
1.2	Comparing optical dimensional metrology solutions for AM	10
1.3	Problem statement	14
1.4	Scientific contributions	15
1.5	Outline	16
1.6	Publications	16
2	Shape-From-Focus	19
2.1	Introduction	19
2.2	Shape-from-focus explained	20
2.2.1	Basic optical principle	20
2.2.2	Methodology	22
2.3	Parameters for shape-from-focus	23
2.3.1	Determining the number of images in a focus volume	24
2.3.2	The focus measure operator	25
2.3.3	Focus measure kernel size	28
2.4	Design and realization of the measurement setup	29
2.4.1	Selecting the camera	30
2.4.2	Selecting the objective	31
2.4.3	Illumination	33
2.4.4	Controlling the focus distance	34
2.4.5	Characterization and calibration of a tunable-lens-based shape- from-focus setup	36

2.4.6	Measurement target	44
2.5	Conclusion	45
2.5.1	Final component selection	45
3	Optimising shape-from-focus processing using phase correlation	47
3.1	Introduction	47
3.2	The focus curve	48
3.3	Shifted phase correlation	50
3.4	Experimental setup	53
3.4.1	Evaluation methods	53
3.4.2	Used hardware and measurement procedure	55
3.5	Results and discussion	56
3.5.1	Comparison using synthetic data	56
3.5.2	Comparison using synthetic data with noise	58
3.5.3	Comparison using real-world measurements	59
3.6	Conclusion	61
4	Focus measure operator speed-up for shape-from-focus using GPU with Py-Torch	63
4.1	Introduction	63
4.2	Implementation	66
4.2.1	Selected focus measure operators	66
4.3	Experimental setup	69
4.4	Results and discussion	69
4.5	Conclusion	73
5	Combining shape-from-focus with laser triangulation	75
5.1	Introduction	75
5.2	Proposed Method	76
5.2.1	Measurement system setup	77

5.2.2	Two-step shape-from-focus	80
5.2.3	Experimental setup	82
5.3	Results and discussion	83
5.4	Conclusion	87
6	A continuous motion shape-from-focus based profilometry method	89
6.1	Introduction	89
6.2	Design of the setup and experiment	91
6.2.1	Measurement system setup	91
6.2.2	Image processing	94
6.2.3	Experimental setup	95
6.3	Results and discussion	96
6.4	Conclusion	99
7	General conclusions	101
7.1	Conclusions	101
7.2	Future work	103

Acknowledgements

I am profoundly grateful to all those who have supported me throughout this academic journey, enabling me to reach this significant milestone in my life. Their unwavering encouragement, guidance, and love have been instrumental in making this accomplishment possible. To some specific people, I would like to express my heartfelt appreciation:

First and foremost, I extend my deepest gratitude to my Promotor Prof. dr. Steve Vanlanduit. His boundless knowledge, dedication, and constant encouragement have been invaluable in shaping my research and academic growth. His unwavering support and insightful feedback have undoubtedly enhanced the quality of this thesis.

Next, I want to extend my love and gratitude to my wife and my children. Your unyielding support, patience, and understanding during the long hours and countless challenges of pursuing this doctorate have been my rock. Your belief in me and your sacrifices are the driving force behind my determination to succeed. I could not have asked for a better family to share this journey with.

I would also like to thank the rest of my friends and family for their continuous support and encouragement. Their belief in my abilities has been a great source of motivation throughout my academic pursuits.

To my dear colleagues and friends, your camaraderie and intellectual discussions have enriched my research experience. I am grateful for the collaborative environment we shared, pushing each other to reach new heights. Your feedback and constructive criticism have been vital in refining my ideas and methodologies.

Finally, I am indebted to the participants of Hi-Pas, whose willingness to take part in this project made this work possible. Your contributions have a significant impact on the field, and I am grateful for your involvement.

To all those who have played a part in my academic endeavor, whether directly or indirectly, please accept my heartfelt thanks. This achievement would not have been possible without your support, and I am deeply appreciative of your presence in my life.

Thank you all from the bottom of my heart.

Abstract

Additive manufacturing (AM) is a rapidly growing field with increasing demands for high precision and accuracy in the production of parts. However, there aren't many of the existing precise and reliable metrology methods that are also integrated in the AM process for quality monitoring. Shape-from-focus (SFF) profilometry is a promising technique for online monitoring of the AM process, as it can provide high-resolution 3D surface reconstructions of printed parts. However, state-of-the-art implementations of SFF are considered time consuming as the reconstruction of a 3D profile requires the processing of a large number of images (100+). Additionally current implementations require the object to be stationary during a measurement. This does not reconcile with the nature of additive manufacturing where continuous motion of the printed part or print head is required for the manufacturing process.

This thesis presents a thorough evaluation of the accuracy and precision of the SFF technique in comparison to traditional metrology methods (Laser triangulation, Structured Light Profilometry, ...). We also propose solutions to overcome the mentioned limitations and adapt the state-of-the-art SFF profilometry method to inline metrology. We show that the measurement accuracy can be improved by using a phase correlation algorithm for data reduction during image processing. Through improvements to the image acquisition we show that the required amount of data for a measurement can be greatly reduced. In addition, we show that the traditionally stationary measurement method can be converted to a continuous scanning method without a significant loss in measurement quality. With these innovations, we were able to reduce the initial measurement time to fully measure a 100 by 100 mm characterization target from 4250 to 175 seconds. An improvement in measurement duration of 24x.

The results of this thesis demonstrate that SFF profilometry can provide fast, highly accurate and precise measurements of the 3D surface of printed parts and is a reliable metrology method for online monitoring of the AM process.

Samenvatting

Additive Manufacturing (AM) ook wel 3D printen genoemd, is een snel groeiend veld met hoge eisen voor precisie in de productie van onderdelen. Echter, het gebrek aan een betrouwbare metrologiemethode voor online monitoring van het AM-proces is een belangrijke uitdaging. Shape-from-focus profilometrie is een veelbelovende metrologie techniek voor online inspectie van het AM-proces, aangezien het oppervlakterconstructies van de geprinte onderdelen kan verstrekken met hoge resolutie. Echter, de state-of-the-art implementaties van Shape-From-Focus (SFF) kunnen als tijdrovend worden beschouwd, aangezien voor de reconstructie van een 3D vorm, meerdere afbeeldingen moeten worden gemaakt en verwerkt. Bovendien vereist de standaard shape-from-focus implementatie dat het object tijdens een meting stil moet staan, wat in strijd is met het 3D print process waar een continue beweging van de printkop vereist is.

Dit werk presenteert een evaluatie van de nauwkeurigheid van de SFF techniek in vergelijking met traditionele metrologiemethoden. We stellen ook oplossingen voor voor de eerder genoemde beperkingen en presenteren methodes om de state-of-the-art SFF profilometriemethode aan te passen aan online metrologie. We laten zien dat de meetnauwkeurigheid kan worden verbeterd door een fasecorrelatie-algoritme te gebruiken voor het genereren van de 3D map. Tevens tonen we aan dat door de beeldacquisitie aan te passen, de vereiste hoeveelheid gegevens voor een meting sterk gereduceerd kunnen worden. Daarnaast laten we zien dat de traditionele statische metingmethode kan worden omgezet in een continue scanningsmethode zonder significant verlies van meetkwaliteit. Dankzij deze ontwikkelingen, hebben we de totale meettijd voor een karakterisatie target van 100 mm bij 100 mm kunnen verlagen van 4250 naar 175 seconden. Dit betekent een verbetering van de meetsnelheid van 24 keer.

De resultaten van deze thesis laten zien dat SFF profilometrie zeer nauwkeurige en precieze metingen van de vorm en het oppervlak van 3D geprinte onderdelen kan verstrekken en een betrouwbare metrologiemethode is voor online monitoring van het AM-proces.

List of abbreviations

- 1D: One-Dimensional
- 2D: Two-Dimensional
- 3D: Three-Dimensional
- AM: Additive Manufacturing
- CAD: Computer Aided Design
- CMM: Coordinate Measurement Machine
- CORR: Correlation Coefficient
- CPU: Central Processing Unit
- CUDA: Compute Unified Device Architecture
- DCT: Discrete Cosine Transform
- DED: Direct Energy Deposition
- DFF: Depth-from-focus
- DOF: Depth of Field
- ETL: Electronically Tunable Lens
- FFT: Fast Fourier Transform
- FMO: Focus Measure Operator
- FOV: Field Of View
- FP: Fringe Projection
- fps: frames per second
- FV: Focus Variation
- GLVM: Modified Gray Level Variance
- GPS: Geometrical Product Specification
- GPU: Graphical Processing Unit
- GRA: Gradient based FMO
- ICP: Iterative Closest Points
- ISO: International Standard Organisation
- ITF: Instrument Transfer Function
- LAP: Laplacian Based FMO
- LED: Light Emitting Diode

- LT: Laser Triangulation
- Matlab: Mathworks software development environment
- MISC: Miscellaneous
- NA: Numerical Apperture
- OCT: Optical Coherence Tomography
- PC: Phase Correlation
- PCT: Portable Characterisation Target
- PE: Perspective Error
- PSF: Point Spread Function
- PSNR: Peak Signal To Noise Ratio
- Python: Programming language
- RSME: Root Mean Square Error
- SFF: Shape-from-focus
- SoL: Sheet of Light
- SPC: Shifted Phase Correlation
- STA: Statistical Based FMO
- SV: Stereo Vision
- TENV: Tenengrad Variance
- VIM: Vocabulaire International des termes fondamentaux et généraux de Métrologie
- WAV: Wavlet Based FMO
- WLI: White Light Interferometry
- WSI: Wavelength Scanning Interferometry

1.1 Dimensional metrology

Over the past decades, the landscape of industrial manufacturing has changed substantially, with the introduction and adaptation of additive manufacturing (AM). One key aspect which is applicable to all forms of industrial manufacturing is dimensional metrology [1, 2]. It is a crucial aspect of quality control and assurance in various industries, including manufacturing, engineering as well as AM. Dimensional metrology involves the precise measurement and assessment of physical dimensions, geometrical characteristics, and surface features of objects or components.

Accurate dimensional metrology is essential for ensuring product quality, functionality, and compliance with design specifications. It plays a vital role in validating manufacturing processes, maintaining precision in component assembly, and facilitating seamless interchangeability of parts. Dimensional metrology also aids in identifying defects, optimising production processes, and minimising rejections or recalls, thereby enhancing overall productivity, customer satisfaction, and cost-effectiveness.

There are a few key criteria that govern dimensional metrology: measurement accuracy, repeatability, reproducibility and traceability. Measurement accuracy is defined in the international vocabulary of metrology (VIM) [3] as "*closeness of agreement between a measured quantity value and a true quantity value of a measurand*", followed by these notes:

- *Note 1: The concept 'measurement accuracy' is not a quantity and is not given a numerical quantity value. A measurement is said to be more accurate when it offers a smaller measurement error.*
- *Note 2: The term "measurement accuracy" should not be used for measurement trueness and the term "measurement precision" should not be used for 'measurement accuracy', which, however, is related to both these concepts.*
- *Note 3: 'Measurement accuracy' is sometimes under-stood as closeness of agreement between measured quantity values that are being attributed to the measurand*

The term measurement accuracy is often misrepresented and confused with measurement precision, which is defined in the VIM [3] as “closeness of agreement between *indications* or *measured quantity values* obtained by replicate *measurements* on the same or similar objects under specified conditions”. This confusion is comprehensible given the very similar definitions between the terms. A recent publication by Shirmohammadi, Mari and Petri [4], gives an explanation about how and why these terms are misrepresented and misunderstood. Similar to “Note 2” of the above definition of accuracy, their work proposes a new interpretation in which measurement accuracy is a combination of trueness and precision as visualised in Figure 1.1.

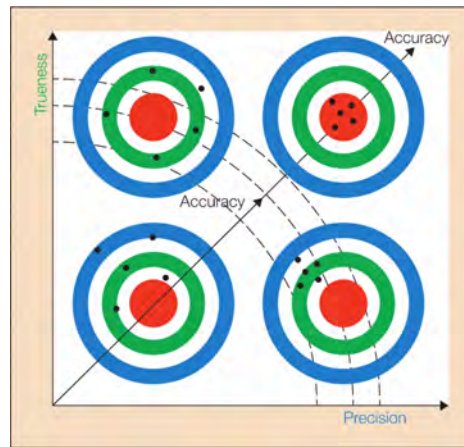


Figure 1.1: New representation of measurement accuracy as proposed in [4], based on the often-used bull’s eye representation of precision and accuracy.

A second principle is repeatability. It is defined in the VIM as “*measurement precision under a set of repeatability conditions of measurement*”, or how close agreeing multiple measurements are of the same characteristic under identical conditions. The identical conditions include: The same measurement procedure, same operators, same measuring system, same operating conditions and same location. The repeatability measurements are required to be measured on the same or similar objects over a short period of time. Thirdly, there is reproducibility. Similar in nature to repeatability, however, it refers to “*measurement precision under reproducibility conditions of measurement*”, in which the reproducibility conditions include: different locations, different operators, different measurement systems, yet still using the same or similar objects. The last, yet, most important key principle is traceability. Measurements should be traceable to a recognised standard, typically maintained by national or international metrology institutes. Traceability ensures the comparability and consistency of measurements across different laboratories and locations. An example of such a standard governing the metrology of areal topography measuring methods is ISO 25178-700 Geometrical product specifications (GPS) — Surface texture: Areal — Part 700: Calibration, adjustment, and verification of areal topography measuring instruments [5] Its content is discussed in 2.4.5

Types of dimensional metrology

In the current industrial field, different methods are used to determine the size, shape and other characteristics of various parts and other items. The most basic metrology methods are contact-based methods, which involve physically touching the object with a measuring instrument. Instruments such as callipers, micrometres, and height gauges are used to measure linear dimensions, diameters, thicknesses, and other features. These methods of dimensional metrology are often employed for quality monitoring on a statistical basis. Samples are randomly picked from a production line and checked for defects. A more automated method of metrology involves the use of coordinate-measuring machines (CMMs). CMMs use tactile or optical probes in combination with a motorised mechanical system to accurately probe objects in predefined locations. Using CMMs it is possible to do a statistical analysis of an object's characteristics over the complete part instead of only in a limited amount of locations.

Optical metrology, also known as non-contact metrology, is another type of measurement technique that does not require physical contact with the object being measured. Instead, optical metrology methods utilise a combination of lighting such as lasers or projectors and cameras to capture measurements. These methods include laser triangulation, confocal microscopy, interferometry, and structured light profilometry, among others. Optical metrology methods offer several benefits over contact metrology. Firstly, due to the measurement being non-contact, there is no risk for the object to be damaged or deformed while measuring. Next, while CMMs deliver sparse datasets, optical metrology methods can quickly capture a large number of data points. Optical methods also offer increased accessibility to complex geometries. Since they don't require physical contact, they can measure objects from various angles and perspectives, even if there are obstructions or limited access. This is especially valuable in the context of AM in which the manufacturing of complex geometries is a major asset. Lastly, some optical metrology methods offer real-time measurement capabilities, allowing for immediate feedback and adjustments. This is another major benefit in the context of AM, as deviations or errors can be detected during manufacturing and corrected in real time, minimising waste and improving efficiency. Contrary, optical metrology methods also have drawbacks. For example, any optical inspection or metrology method is susceptible to reflections. Unwanted reflections can cause parts of the images to be saturated, resulting in a loss of information. In some cases polarizing filters can help to eliminate reflections, as un-polarized light becomes polarized with specular reflections. With diffuse reflections however, there is no dominant polarization vector to eliminate the reflections using a polarizing filter

Dimensional metrology is a critical discipline that ensures the accuracy, quality, and conformity of manufactured components. By employing precise measurement techniques and instruments, dimensional metrology aids in maintaining product integrity, optimising manufacturing processes, and meeting industry standards. In the context of AM, it is obvious that optical methods are more suited to automate the metrology process due to their advanced capabilities in comparison to traditional contact methods.

1.2 Comparing optical dimensional metrology solutions for AM

Over the last twenty-five years, 3D optical scanning methods have become a key tool for many different applications, such as archaeology, video games, security systems and industrial production processes in general [6, 7, 8]. These industries rely on some form of 3D metrology to measure or verify the dimensions of products and components. Most optical methods are developed for inspection and metrology of finished parts or for reverse engineering purposes. To improve the quality of additively manufactured products it is of interest to develop these shape recovery techniques for use in in-line or even online metrology. The list of optical metrology methods is extensive and can generally be divided into two categories: active methods that require a (modulated) light source and passive methods. The active group includes well-known methods such as laser triangulation [9], fringe projection [10, 11, 12, 13] or time-of-flight [14, 15], while other well-known methods such as photogrammetry [16], stereovision [9, 17] or shape from focus (SFF)[18, 19] can be classified into the passive group. Although comparing all potential optical methods is unfeasible, we aim to assess commonly used techniques regarding their suitability for full-field metrology of additively manufactured components during printing. Our evaluation will be based on various capabilities, such as field of view (FOV) and measurement resolution, as well as implementation complexity. Apart from the technical aspects to guarantee measurement accuracy and speed, it is important that the selected measurement method is capable to work in the conditions specific to AM. The AM process results in a high temperature measurement environment and can cause unwanted vibrations.

Laser Triangulation

One of the most commonly used methods for parts inspection [20, 21] or profilometry in general is laser triangulation (LT) [22, 23, 24]. It involves projecting a laser line onto the surface of an object and capturing its deformation using a camera. By analysing the displacement of the laser line, the surface profile can be reconstructed (Figure 1.2). Laser triangulation is known for its simplicity, fast acquisition speed, and compatibility with various materials. However, it may encounter difficulties with highly reflective or transparent surfaces. LT does not provide full-field measurements. Every single measurement contains a single line of information. By translating or rotating an object, a 3D profile can be reconstructed. Like many methods, it is based on triangulation. Therefore, it requires careful calibration of the camera and laser line to perform accurate measurements. Another drawback of any triangulation-based method is the risk of occlusions. The laser line for LT is tilted compared to the camera. The amount of tilt determines the height accuracy and precision for LT measurements. However, with increasing tilt comes a higher risk of occlusions. This is explained in more detail in Chapter 5.

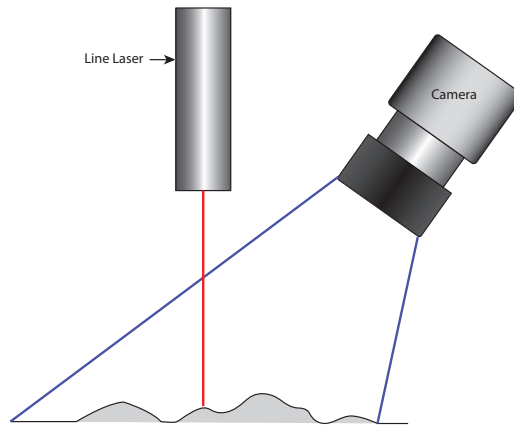


Figure 1.2: The principle of laser triangulation, where the position of a reflected laser line on a camera sensor is a function of the profile height. Based on an image from Sun B. and Li B. [12].

Fringe Projection

Similar in nature to LT, is fringe projection (FP) also known as structured light profilometry [25, 26, 27]. FP uses the projection of a known pattern, instead of a laser line, onto the object's surface, capturing its deformation through a camera (Figure 1.3). By analysing the deformed pattern, the surface profile can be extracted. This method provides high-resolution measurements with good accuracy. It is capable of handling complex surface geometries and can operate at different scales. However, structured light profilometry can struggle with glossy or specular surfaces due to light scattering and can be sensitive to ambient lighting conditions. Measurements are in general faster with FP compared to LT, with FP being a full-field measurement method.

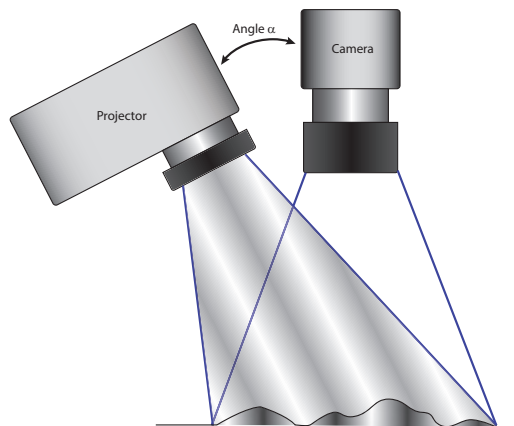


Figure 1.3: The principle of fringe projection, where a pattern, projected onto an object, is deformed by the object and this deformation is measured by a camera. The depth map can be calculated after the calibration of the camera and projector.

With FP being also based on triangulation, it suffers from the same occlusion problem as LT. Various options exist to position the projector and the camera. The optimal solution is extensively calculated and described in [28]. It is possible to center the projector above the target add a second camera opposite the projector to eliminate these occlusions. Adding a camera adds processing complexity since two point clouds must be aligned and combined.

White Light Interferometry

White light interferometry (WLI) measures the interference pattern produced by splitting a light beam into a reference and sample beam (Figure 1.4). By analysing the interference, the surface profile can be obtained with sub-micrometer resolution. This technique excels in measuring highly reflective and transparent surfaces, providing excellent axial resolution. However, it is more complex to set up, requires precise calibration, and is sensitive to vibrations and environmental disturbances like temperature.

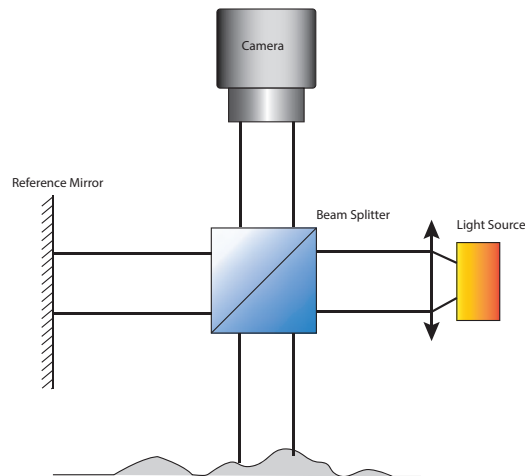


Figure 1.4: The basic setup for white light interferometry where a broad band white light source is split into a reference beam to the reference mirror and a sample beam to the object. The returning light waves interfere when recombined in the beam splitter and a fringe pattern is projected on the camera sensor. A 3D profile can be reconstructed from that fringe pattern.

Apart from WLI, other interferometric methods exist such as "wavelength scanning interferometry (WSI)" and "optical coherence tomography (OCT)". The main drawback for using any interferometry method is the complexity of the setup. Both WSI and WLI can be considered full field measurement methods, where OCT only measures single points. WSI is typically slower and more complex to setup compared to WLI, yet, WSI is usually has higher precision and accuracy.

Stereovision

Next to the active methods mentioned above, one of the most frequently used passive methods is stereovision (SV). The principle is similar to human vision where two (or more) cameras are spaced by a known distance and with careful calibration can triangulate the position of every image point (Figure 1.5). With it being also a full-field measurement method, data acquisition and reduction can be considered rapid compared to LT. However, highly accurate measurements with SV are only possible with very precise calibration, which is a time-consuming and complex process in itself. Additionally, SV also requires texture and features to be able to match image points in the images of the two camera's

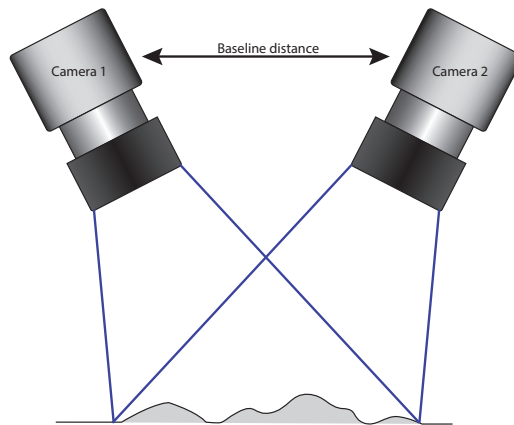


Figure 1.5: The basic setup for stereovision profilometry. Two cameras with the same FOV but from a different perspective. The 3D coordinates of object points are triangulated after careful calibration of the intrinsic camera parameters and the extrinsic setup parameters such as the baseline distance.

Shape From Focus

Throughout the different techniques for optical shape recovery, shape-from-focus (SFF) otherwise known as depth from focus (DFF) or focus variation microscopy (FV) is somewhat of an outsider. Its working principle and implementation are detailed in **Chapter 2**. ISO25178-606:2015: Geometrical product specification (GPS) — Surface texture: Areal — Part 606: Nominal characteristics of non-contact (focus variation) instruments [29], defines the metrological characteristics and the sources of measurement error of such devices. In brief, SFF tries to recover the camera-object distance based on the focus level of pixels [30, 31, 32]. In terms of precision and repeatability compared to other previously mentioned methods, SFF is a good candidate for micrometre precision measurements for AM [33, 34, 35]. Additionally, SFF has fewer problems with occlusions compared to triangulation-based methods, can measure very steep angles and has the possibility to create an all-in-focus image that could be used in the analysis for surface defects.

Shape-from-focus is a non-contact technique that does not require complex hardware setups, making it relatively easy to implement. Additionally, SFF can provide high-

resolution measurements and is suitable for surfaces with complex geometries. One of the main advantages of SFF is its ability to capture fine details on the surface, making it useful for inspecting AM parts with intricate features. It is particularly beneficial for applications where surface roughness or small-scale defects need to be evaluated. Moreover, SFF can handle a wide range of materials, making it versatile for different AM processes. Another potential benefit of SFF compared to the other methods is that existing camera optical ports in metal additive manufacturing machines can potentially be used to integrate SFF into the machine. This could make implementing the method in existing machines easier and more cost effective. One drawback of the basic shape-from-focus implementation is that it requires surface texture to work. Usually in the case of AM this is not a problem. However, when parts are milled or made optically smooth in another way, shape-from-focus might not have sufficient texture to measure accurately. A solution to this problem already exists in the form of projecting a pattern onto an object and using that pattern to estimate the focus [36].

1.3 Problem statement

As previously mentioned, the in-line or online monitoring of the AM process output requires an adequate 3D profilometry method to accurately measure the printed shapes. Through the literature review, five different methods were identified and compared for their applicability in the AM process monitoring. From these five methods, SFF was identified as the most promising method based on its inherent measurement accuracy and lack of issues with occlusions. Alternatively, WLI could also be an interesting candidate for in-line monitoring if its temperature and vibration dependencies are solved. Thus, for this research we opted to proceed with SFF. However, SFF also has limitations.

- It requires multiple images at different focal planes, which can increase acquisition time compared to other optical profilometry techniques.
- The data processing is also time-consuming compared to other methods that require far fewer images to produce a 3D profile
- Although the claimed accuracy and precision of commercial SFF devices [37] are on par with what is expected for AM, the measurement area of these commercial devices is far from the capabilities of current AM machines.
- The principle of SFF, with its increased acquisition time, requires the subject to be stationary during a measurement. This does not align with the continuous motion nature of AM.

The primary objective for an online or in-line metrology method for AM is to produce a highly accurate 3D profile in a limited time-frame, enabling potential adjustments to the printing process if issues are identified. This necessitates enhancing the speed of SFF measurements to minimise their influence on the AM process. Additionally, the measurement strategy of SFF must be tailored to align with the principles of AM, leading to the formulation of the central research question.

Problem Statement

How can we adapt the shape-from-focus method to make it suitable for fast and high-precision metrology for online or in-line monitoring of the AM process?

In order to effectively address the problem statement, it was split into two parts. The first part includes a comprehensive study of the SFF method to identify which parameters influence the measurement speed and quality in order to optimise the processing of SFF data. The second part of this thesis involved optimising the measurement strategy for its application in the AM process.

1.4 Scientific contributions

This dissertation presents several significant contributions to the field of shape-from-focus (SFF) and its application in additive manufacturing. Firstly, it offers a comprehensive overview of the theoretical foundations of SFF, including the key parameters that influence measurements. This overview guides the selection of components for constructing a custom SFF system and provides insights into calibration for metrology purposes.

Furthermore, this thesis introduces an innovative methodology based on phase correlation to enhance the precision of SFF measurements without compromising processing speed. By analysing the phase information of SFF data, it achieves more accurate depth determinations. Additionally, an extended processing step is presented to further enhance results, albeit with a slight decrease in processing speed. Comparative analyses are conducted using both simulation data and real measurements, employing standard analytical measures commonly used in the SFF field.

To expedite SFF data processing, the thesis transitions from traditional CPU-based methods to GPU-based processing, leveraging a modern framework initially developed for neural networks. This transition simplifies the conversion process and elevates the processing speeds to meet the requirements for real-time monitoring of the additive manufacturing process.

The dissertation also introduces a method to reduce the measurement time of large-area SFF scans by incorporating laser triangulation measurements into the measurement planning for SFF. Utilising coarse 3D profile data from the laser triangulation sensor optimises the measurement range for various SFF scans, eliminating non-contributory data. Validation is performed by comparing the output data from the custom-built system with measurements obtained from a commercial metrology system.

Lastly, the thesis presents a method to transform the state-of-the-art SFF approach from a slow and discrete process into a continuous scanning method, aligning with the continuous motion inherent to additive manufacturing. This method involves synchronising focus scanning and data capture at high speeds, aligning measurement speed with current metal additive manufacturing printing speeds. Results demonstrate the effectiveness of this approach and compare measurement quality with the discrete method using the same system.

In summary, this dissertation describes substantial advancements in both the speed and quality of SFF metrology systems for additive manufacturing, thereby contributing to the overall improvement of the additive manufacturing process. Importantly, the technology developed here extends beyond AM monitoring, holding the potential for enhancing quality and speed in profile measurements for various inspection processes across different industries.

1.5 Outline

This dissertation consists of three distinct parts: Part one consists of this introduction and the detailed explanation of shape-from-focus, Part two discusses two methods for improving the quality and measurement speed of SFF measurements and lastly, part three explores two methods to improve the applicability of SFF for online additive manufacturing. This introduction and Chapter 2 aim to provide the reader with context for the rest of the thesis. Chapter 2 also provides the reader with details on the setup and calibration methods that were used throughout the rest of this research. Chapter 3 explains a method to improve the quality of SFF measurements without impacting the processing time. Chapter 4 details an easy-to-implement method to reduce the processing time of SFF measurements by using a graphical processing unit (GPU). Chapter 5 discusses a method to improve the acquisition speed of large-area SFF measurements using a two-step approach with LT. The last main chapter, Chapter 6, explains a method to overcome the inherent discrete nature of SFF and adapt it to the continuous motion nature of AM. This dissertation then finishes with a concluding statement and possible topics for future research.

1.6 Publications

A1 Journal Papers

First author

1. Gladines, J.; Sels, S.; Blom, J.; Vanlanduit, S. A Fast Shape-from-Focus-Based Surface Topography Measurement Method. *Sensors* **2021**, *21*, 2574. <https://doi.org/10.3390/s21082574>
2. Gladines, J.; Sels, S.; Hillen, M.; Vanlanduit, S. A Continuous Motion Shape-from-Focus Method for Geometry Measurement during 3D Printing. *Sensors* **2022**, *22*, 9805. <https://doi.org/10.3390/s22249805>
3. Gladines, J.; Sels, S.; De Boi, I.; Vanlanduit, S. A phase correlation based peak detection method for accurate shape from focus measurements. *Measurement*, **2023**, Volume 213, 112726, ISSN 0263-2241, <https://doi.org/10.1016/j.measurement.2023.112726>.

co-author

4. De Kerf, T.; Gladines, J.; Sels, S.; Vanlanduit, S. Oil Spill Detection Using Machine Learning and Infrared Images. *Remote Sens.* 2020, 12, 4090. <https://doi.org/10.3390/rs12244090>
5. Verspeek, S.; Gladines, J.; Ribbens, B.; Maldague, X.; Steenackers, G. Dynamic Line Scan Thermography Optimisation Using Response Surfaces Implemented on PVC Flat Bottom Hole Plates. *Appl. Sci.* 2021, 11, 1538. <https://doi.org/10.3390/app11041538>
6. Baleani, A.; Paone, N.; Gladines, J.; Vanlanduit, S. Design and Metrological Analysis of a Backlit Vision System for Surface Roughness Measurements of Turned Parts. *Sensors* 2023, 23, 1584. <https://doi.org/10.3390/s23031584>
7. Hillen, M.; De Boi, I.; De Kerf, T.; Cardenas De La Hoz E.; Gladines, J.; Sels, S.; Steenackers, G.; Penne, R.; Vanlanduit, S. Detected Checkerboard Enhancement using Gaussian Processes. *Mathematics*, **2023**, Volume 11(22), 4568. <https://doi.org/10.3390/math11224568>

P1 Conference Proceedings

co-author

8. Baleani, A.; Paone, N.; Gladines, J.; Vanlanduit, S. Surface roughness measurements of turned parts through a vision-based measurement system: uncertainty analysis and performance comparison with state-of-the-art instruments. 2022 IEEE International Workshop on Metrology for Industry 4.0 & IoT (MetroInd4.0&IoT), Trento, Italy, **2022**, pp. 17-22, doi: 10.1109/MetroInd4.0IoT54413.2022.9831674.

Shape-From-Focus

2.1 Introduction

Shape-from-focus (SFF) is a metrology method that uses focus information to retrieve a 3D profile of an object. The requirement of having to focus a lens on a subject when using a camera determines that there is a fixed relationship between the lens focus position and the distance of an object to the camera. Therefore after careful calibration of the focus positions of a camera with respect to object distance, it is possible to determine the distance of an object point to the camera, by focusing a lens on that point and reading the focus position of the lens. Calculating the camera-object distance for every point in the field of view (FOV) of the camera then results in a 2D map with depth information. This map can then be converted into a 3D surface profile. The concept of shape-from-focus was presented in 1992 by Shree K. Nayar et al. [38] based on a publication about "depth from focus" from P. Grossmann from 1987 [39]. SFF was presented to be used primarily for the profilometry of small objects with rough surfaces using optical microscopes. For example the inspection of printed circuit boards or quality control of cutting edges of machining tools[40].

In this chapter, we will first discuss the optical principle on which SFF is based and explain the method of recovering a surface profile from a set of images. Next, we will describe the design and development of the SFF setup that was built for this research. Lastly we will review the possible methods for calibrating a tunable-lens-based SFF system and characterising it for accurate and precise measurements. The goal of this chapter is to provide the reader with a detailed understanding of the basic shape-from-focus method.

2.2 Shape-from-focus explained

Chapter 1 emphasizes that traceability to standards is a fundamental principle of metrology. The ISO standard 'Geometrical product specification (GPS) — Surface texture: Areal — Part 606: Nominal characteristics of non-contact (focus variation) instruments' [5] discusses the shape-from-focus method, also known as focus variation method, and its application in areal surface texture instruments. This section provides a comprehensive explanation of the method, starting from its basic optical principles and delving into the finer details of image processing and component selection for accurate surface profile analysis.

2.2.1 Basic optical principle

Starting from the thin lens model (Figure 2.1), the distance (u) from an object to the lens and the lens's focal length (f) determine the distance of the projected image to the lens (d), also known as the focal plane. When a sensor is placed in the focal plane, the image is projected in focus onto the sensor. Any distance in front or behind the focal plane will project an image out of focus. This relationship between u , f and d is given by the Gauss lens law.

$$\frac{1}{f} = \frac{1}{u} + \frac{1}{d} \quad (2.1)$$

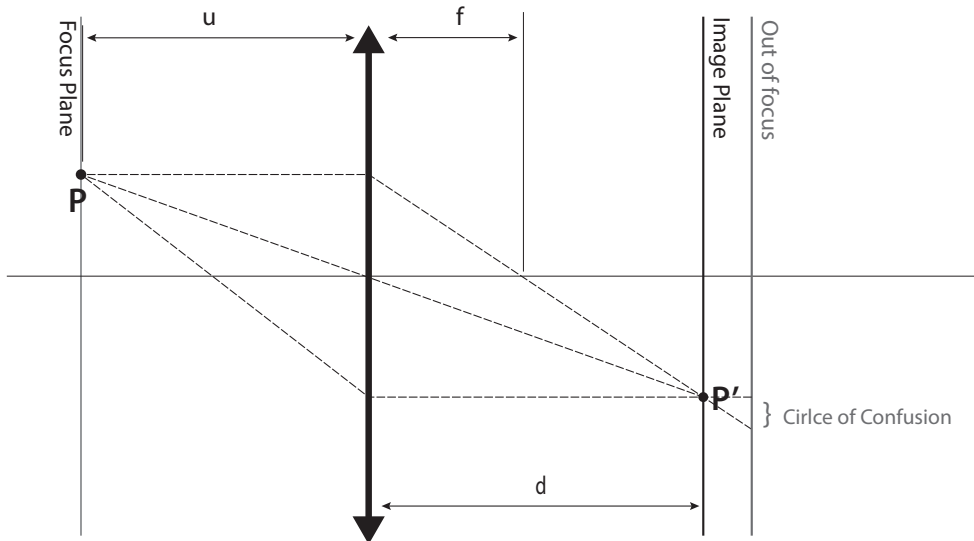


Figure 2.1: Thin lens model explaining how an image of point P is formed in the focal plane depending on the lens focal length f and the object lens distance u .

Also from this thin lens model (Figure 2.1), we can see that the light of a single point on the image is spread over a larger surface when out of focus. This is also known as the circle of confusion. The way in which light from a point source is spread when out of focus is determined by the point spread function (PSF). This PSF is unique for every optical assembly. The PSF can empirically be determined by applying an impulse, a true point source, to an optical system. However, in many cases, the PSF is approximated by a Gaussian function. For example, Equation 2.2 represents an equation to calculate a symmetrical, two-dimensional, Gaussian distribution where μ is the mean and σ is the standard deviation respectively.

$$f(x, y) = \frac{1}{2\pi\sigma^2} e^{-[(x-\mu_x)^2 + (y-\mu_y)^2]/(2\sigma^2)} \quad (2.2)$$

From Equation 2.1 and Figure 2.1 we can also see that, at least theoretically, point P is only in focus at distance d from the lens. In reality, due to diffraction, a true point source will not be projected as a point but rather as an Airy disk for circular apertures. The size of this Airy disk can be approximated with Equation 2.3

$$\sin \theta \approx 1.22 \cdot \frac{\lambda}{NA} \quad (2.3)$$

With θ being the angle of the first minimum of the Airy disk. λ is the wavelength used and NA is the aperture of the lens. The image of a point source can go out of focus, as long as the circle of confusion is smaller than the Airy disk, the image can be considered fully resolved or in focus (Figure 2.2). Thus a point can be considered in focus over a range of distances to the lens. This range is called depth of field (DOF).

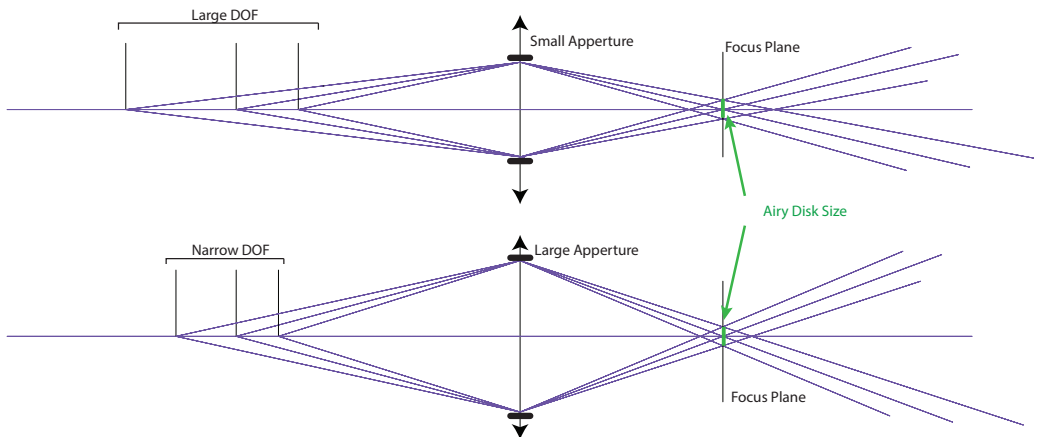


Figure 2.2: Thin lens model explaining how the aperture of a lens controls the depth of field (DOF). A narrow DOF is obtained with large apertures and smaller apertures result in a large DOF.

The size of the Airy disk depends on the aperture of the lens, thus in practice, the numerical aperture (NA) of an objective limits the depth of field. For example, the depth of field δ_z of a microscope objective can be approximated by:

$$\delta_z \approx \frac{\lambda}{NA^2} \quad (2.4)$$

A practical example of how aperture controls the DOF is shown in Figure 2.3. When the aperture is small, the depth of field is large and when the aperture is large, the depth of field is very narrow. For an application like shape-from-focus, it is important to have a very narrow DOF, this will be explained further in this chapter. Thus for SFF choosing an objective with a high NA is paramount.

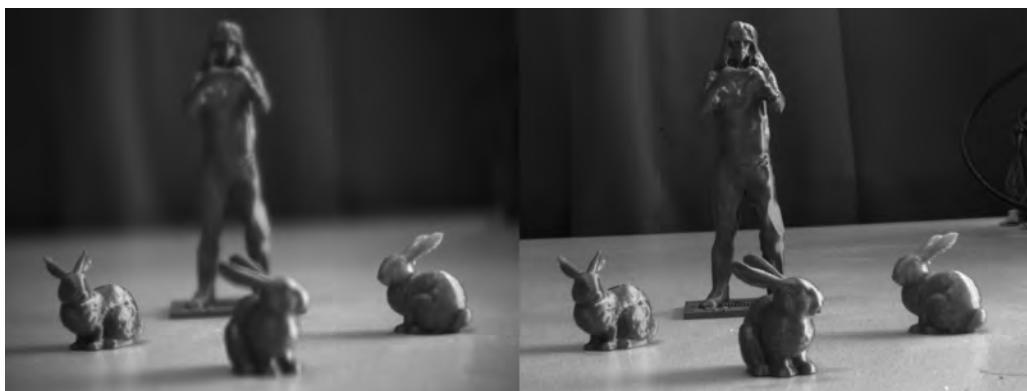


Figure 2.3: Left: large aperture ($f/1.4$) resulting in small DOF of about 2cm, Right: small aperture ($f/22$) approaching pinhole model camera, resulting in large, almost infinite, DOF

2.2.2 Methodology

As discussed, Shape-from-focus takes advantage of the relationship that exists between lens focus and the distance of an object in focus to the camera. When capturing an image using a camera equipped with a lens featuring a wide aperture and resulting shallow DOF focused at a specific distance from the camera, all the pixels in focus within the image can be regarded as being at that precise distance from the camera. By creating a series of images at different focus distances, by refocusing the lens or by moving the object along the optical axis through the focal plane of the lens, a focus volume is created (see Figure 2.4 left). Next, by estimating the pixels in focus for each image in this volume using algorithms called focus measure operators (FMO), a camera-object distance can effectively be determined for every pixel. The 3D profile of the object is then determined by extracting the relative pixel-to-camera distances in the form of a depth map (see Figure 2.4 right). This is the basic concept of SFF.

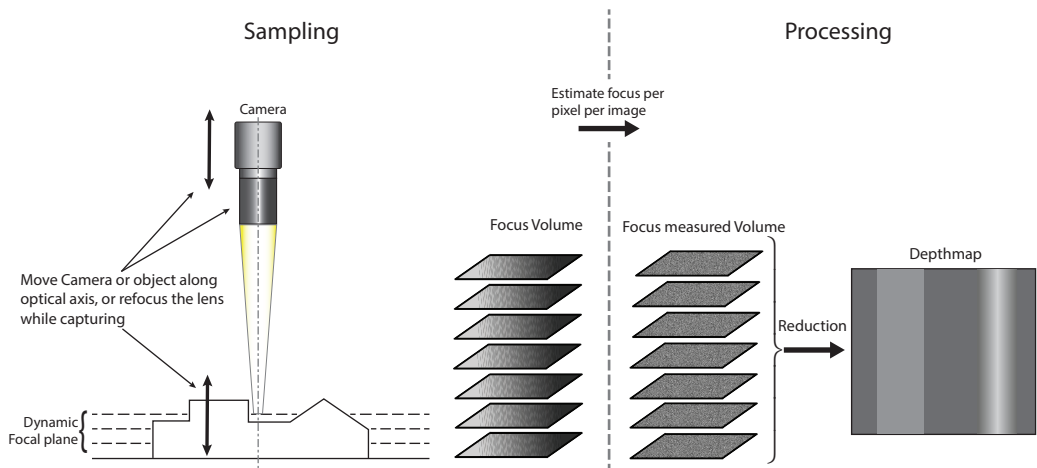


Figure 2.4: To recover a profile using shape-from-focus sampling, the object is first sampled at different focal distances(left) and then processed using an FMO into a 3D profile (right).

2.3 Parameters for shape-from-focus

Several parameters influence the process and results of SFF measurements. Among these parameters, several hold particular significance:

- **Camera:** The characteristics of the camera, including its sensor size, resolution, and sensitivity, substantially impact the quality of SFF results.
- **Objective:** The chosen objective lens affects magnification and resolution, thereby influencing the level of detail captured during SFF analysis.
- **Subject Illumination:** The method of illuminating the subject surface significantly influences the visibility of surface features and texture in SFF imaging.
- **Focus Distance Control Method:** The method employed to control the focus distance during image acquisition plays a critical role in achieving accurate SFF results.
- **Focus Step Size:** Determining the incremental distance between focus positions is pivotal, affecting the precision of SFF reconstructions.
- **Number of Images in Focus Volume:** The number of images acquired within a designated focus volume contributes to the fidelity of the resulting 3D surface representation.
- **Focus Measure Operator:** The choice of algorithm for evaluating focus across images profoundly impacts the accuracy of SFF-derived surface details.
- **Kernel Size for Focus Measure Operator:** The size of the kernel utilised within the focus measure operator bears weight on the granularity of focus assessment.

The first four parameters: Camera, Objective, Subject Illumination, and Focus Distance Control Method, are intrinsic to the hardware setup and are usually immutable. These parameters are comprehensively discussed in Section 2.4. On the other hand, the latter parameters are flexible and subject to software control. The following subsections address them.

2.3.1 Determining the number of images in a focus volume

One question that might arise when researching SFF, is how many images are required in a focus volume. That question however is difficult to answer. It all depends on the height range one wants to measure, the height resolution and the strength of the processing methods. The focus volume will always be a discrete set of images representing a continuous range of heights. Thus one can infer that capturing more images, at least theoretically will result in a better height resolution. This is clearly shown in Figure 2.5, where the same object is measured using SFF with varying amounts of images. The first measurement (left) contains 20 images measured over a 10 mm height range, for a height resolution of 0.5 mm. The second measurement (right) contains 150 images, for a height resolution of approximately 0.067 mm. These measurements were processed using the most basic method to determine the relative point-to-point height, by using the focus distance of the image with the best focus for every pixel. The reduced set of images results in a reduced height resolution of the 3D profile.

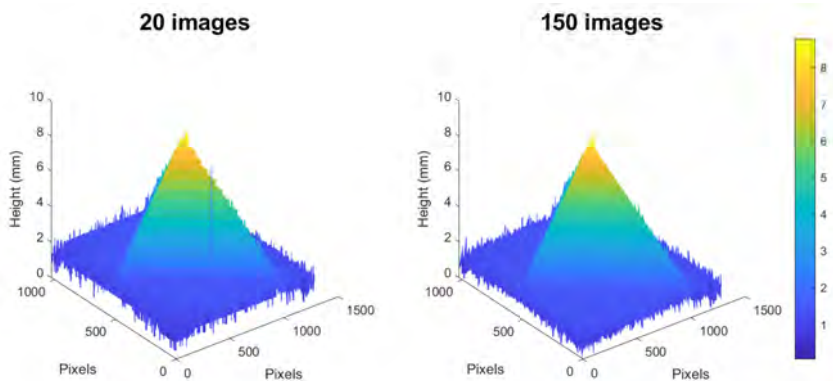


Figure 2.5: The results of an SFF measurement to visually compare depth map quality and height resolution vs. the amount of captured images. Left: fewer images, low height resolution. Right: more images, better height resolution

Reducing the amount of images focus volume can potentially be beneficial, as fewer images to capture and process can greatly improve the measurement speed of a system. This subject is explored in Chapter 5. Chapter 3 explores the realm of interpolating between pixel focus measurements, to improve the measurement quality, especially when trying to reduce the amount of images in a focus volume. Additionally, some processing methods also rely on the 3D neighbourhood around a pixel to measure the depth which then requires a certain minimum amount of images [41, 42].

2.3.2 The focus measure operator

The theoretical value for the amount of pixel focus is determined by applying a focus measure operator (FMO) to every image of the focus volume. FMO algorithms return a value based on the differences between the pixel and neighbouring pixels. A higher value returned by the FMO means a better focus of the pixel. From this, we can infer that finding the pixel depth can be achieved by locating the maximum response to the FMO for every pixel across the focus volume.

These Focus measure operators are computational algorithms used to evaluate and quantify the sharpness or focus of an image or pixels within an image. By measuring various aspects of the image, such as contrast, edge sharpness, or high-frequency content, a focus measure operator provides a numerical value that represents the degree of focus or blur present in the image. From a computer perspective, most FMOs are implemented as convolutions of a convolution kernel with an image. Chapter 4 elaborates on this implementation and proposes a method for improving the processing speed. A detailed review of different FMOs used for SFF is given in the works of S. Pertuz et al. [43]. They categorise the different FMOs into Six different categories:

- Gradient based (**GRA**): GRAE [44], GRAT [45], GRAS [46], TENG [47], TENV [48]
- Laplacian (**LAP**): LAPM [49], LAPV [48], LAPD [50]
- Wavelets (**WAV**): WAVS [51], WAVV [51], WAVR [52]
- Statistical Operators (**STA**): GLVA [47], GLLV [48], GLVN [45], GLVM [43], HISE [47], HISR [53]
- DCT (Discrete Cosine Transform) (**DCT**): DCTE [54]
- Miscellaneous (**MISC**): BREN [45], HELM [55], SFRQ [46]

Gradient-based operators (**GRA**) operate under the assumption that focussed images exhibit more pronounced edges than blurred ones. Consequently, the gradient or first derivative is employed to quantify the degree of focus. Laplacian-based operators (**LAP**), use the second derivative or Laplacian to gauge the amount of edges in an image. Wavelet-based operators (**WAV**) employ the discrete wavelet transform to extract frequency and spatial information from images. Statistical operators (**STA**) exploit various image statistics as texture descriptors to calculate the focus level. DCT operators (**DCT**) use the summation of the frequency components of the discrete cosine transform as a focus measure. Yet the DCT operators, as proposed in [56], were extremely time consuming and therefore not used in this work. The other operators such as BREN and HELM could, according to [43], not be attributed to one of the previous categories and were subsequently placed un the term miscellaneous (**MICS**).

These FMO's all have advantages and disadvantages that make them more or less suited for use in online AM inspection. Unfortunately no objective criterion exists to determine which FMO is the most optimal choice for use in AM. Therefore we opted to compare the existing FMOs based on these ability to qualitatively reproduce a depth map from a metal 3D printed target (Subsection 2.4.6) and the speed at which they do so.

For the experiments, we first evaluated all implemented FMOs as introduced by S. Pertuz et al. [56]. We compared the depth map quality (Figure 2.6), processing time (Figure 2.7) and root mean square error (RSME) to a reference depth map (Figure 2.8), by processing data captured on our own system (Section 2.4). Some of the FMOs implemented in [56], were excluded from the evaluation because they were: incompatible with our data, impractically slow or delivered extremely bad depth maps. From the results in Figure 2.6 and Figure 2.8, we conclude that BREN, GLVM, HELM, HISR, LAPD, TENG, TENV and WAVR produce the lowest noise, highest quality depth maps. Although WAVR delivers excellent quality depth maps, Figure 2.7 shows that the processing time for WAVR is considerably longer compared to the other FMOs. Thus, in this dissertation, we have limited the scope to two different focus measure operators, namely: Modified Gray Level Variance (GLVM, **STA**) and Tenengrad Variance (TENV, **GRA**), for their depth map quality, fast processing times and easy implementation.

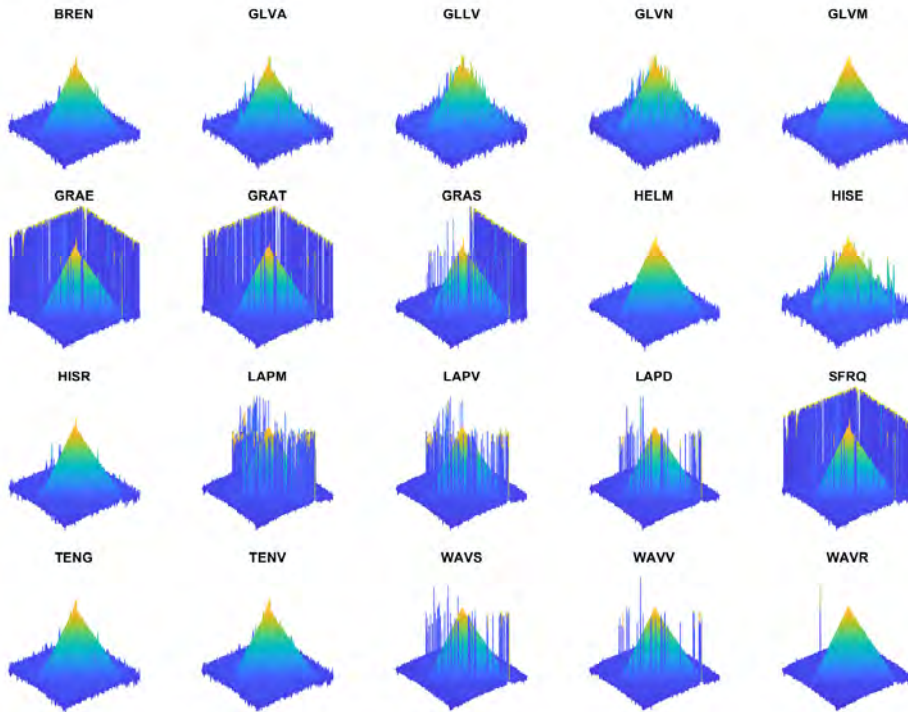


Figure 2.6: Comparison between the available FMO from [56]. A set of 150 images captured with our custom build measurement system is processed using the different FMOs, with kernel size 9×9 . Visually it is possible to see differences in noise in the produced depth maps, yet an objective analysis using RSME and processing time is key to select the best FMO.

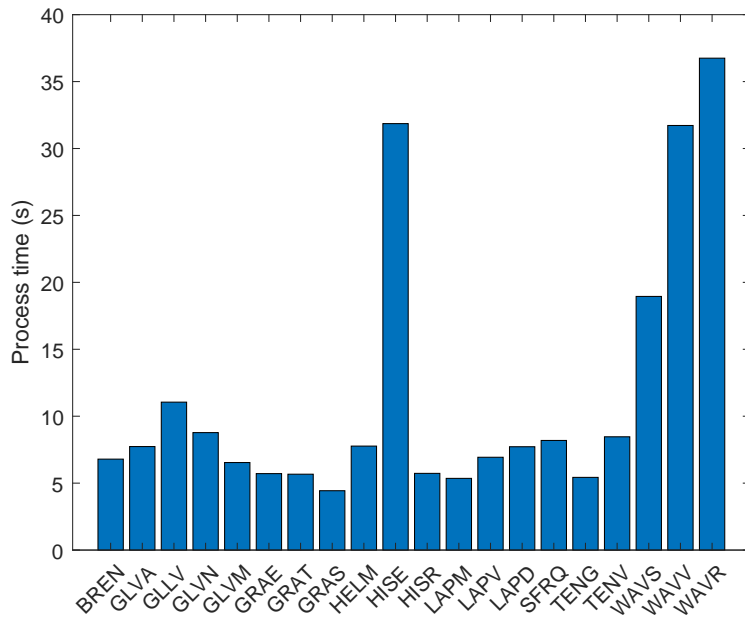


Figure 2.7: Processing duration for the generation of the different depth maps in Figure 2.6.

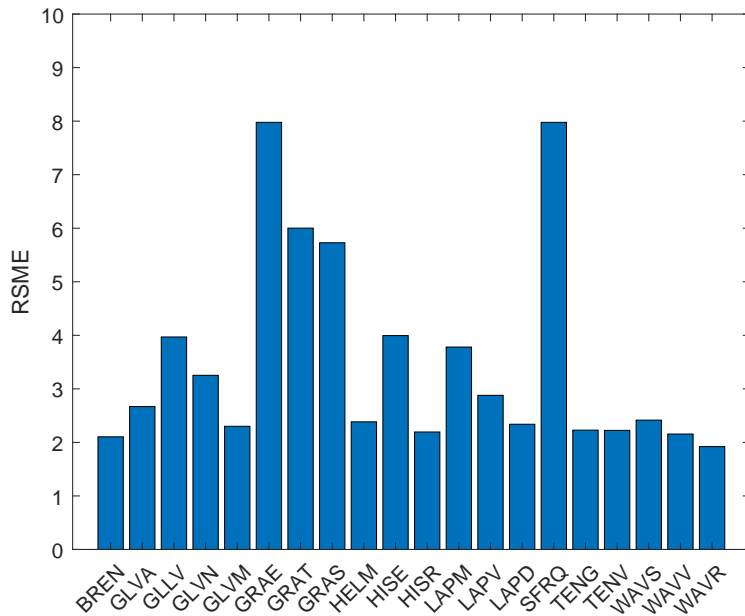


Figure 2.8: Root Mean Square Error (RSME) of the different depth maps in Figure 2.6 compared to a reference depth map.

2.3.3 Focus measure kernel size

Most focus measure operators reviewed by S. Pertuz et al. [43] require only one parameter, the kernel size. The question of what is the optimum kernel size is similar to the question about the amount of images required in a focus volume. It all depends on the texture of the object's surface, the lighting, the topographic spatial resolution required, the amount of noise that can be tolerated and more. Figure 2.9 shows the difference in depth map quality when varying the kernel size. The 3D profile on the left is the result of a measurement with a larger kernel size, resulting in a blurrier but less noisy depth map. The measurement on the right uses a smaller kernel size, resulting in a sharper, more detailed but also more noisy depth map.

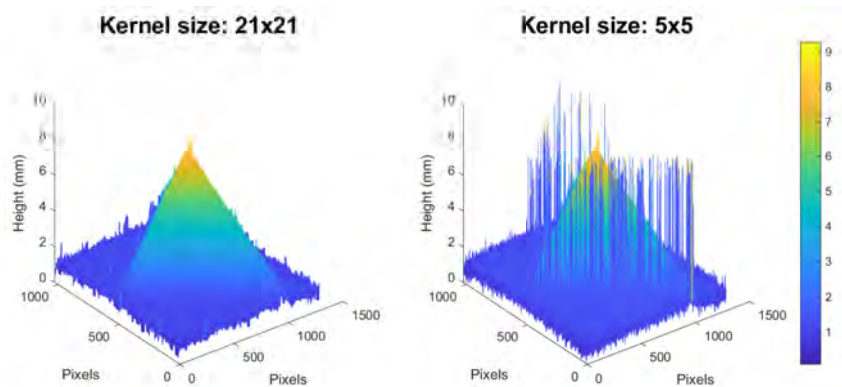


Figure 2.9: The results of an SFF measurement to visually compare depth map quality vs. kernel size. Larger kernel sizes (Left) result in a less noisy depth map, however, don't allow smaller features to be detected. Smaller kernel sizes (Right) allow for smaller features to be measured, yet, result in noisier depth maps

We can evaluate the RMSE for a given FMO and different kernel sizes. This evaluation is shown in Figure 2.10 for the two selected FMOs (GLVM, TENV). Using the same dataset that was used for the previous evaluations, we generated different depth maps with the selected FMO and different kernel sizes. The resulting depthmaps are then compared to the reference depth map to calculate the RMSE. From Figure 2.10 it is clear that for both FMOs the RMSE is high for a kernel size of 3 or 5. At a kernel size of 7 or 9 both FMOs reach their optimal performance with this data after which the RSME increases again for larger kernel sizes. From this we can conclude that using a kernel size of 7 or 9 for these FMOs is best.

The size of the FMO kernel not only has an effect on the depth map quality and resolution but also on the processing time. Larger kernels require more values to be evaluated in the convolution resulting in a longer processing time on the same hardware. This effect is also studied in Chapter 4

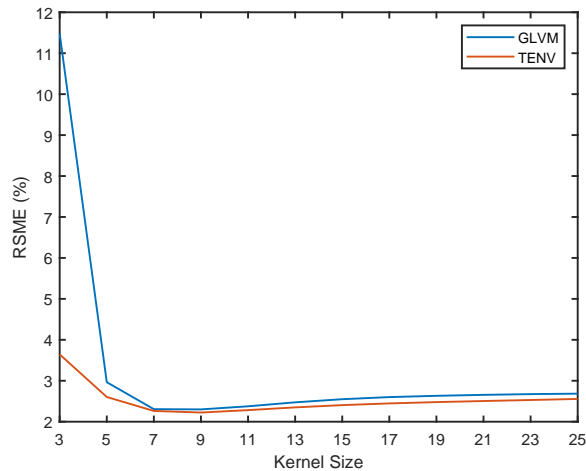


Figure 2.10: The evaluation of the effect of the kernel size on the depthmap quality for GLVM and TENV. The kernel size was varied from 3 to 25 in increments of 2. The optimal kernel size for our data appears to be 7 or 9.

In conclusion to this section, after capturing the images for the focus volume, every image of that volume is focus measured and the maximum response to the selected focus measure operator is located within the volume. The location or index of this maximum response is then a measure for the camera-to-object point distance. The true distance or relative distances between the points are only found after calibration of the setup. The relevant information on how to design, develop and calibrate an SFF setup is described in the following section.

2.4 Design and realization of the measurement setup

As discussed in the previous section, some of the parameters that determine the accuracy of SFF measurements are the result of choices made when building the setup. The practical considerations that are discussed, are key to a successful implementation of a shape-from-focus system. These include:

1. The selection of the camera
2. The selection of the objective
3. Illumination sources
4. Controlling the focus distance
5. The capturing of the images
6. The basic processing of images to a depth map
7. The calibration of an SFF system.

As has been established in Chapter 1, this dissertation delves into the realm of micrometre (μm) precision metrology for additive manufacturing. Achieving shape-from-focus (SFF) at this scale necessitates the use of microscopy objectives, which typically yield limited fields of view. Consequently, the rest of this work will exclusively discuss SFF microscopy applications. This will be further clarified in the following subsections.

2.4.1 Selecting the camera

A camera has multiple important parameters including, but not limited to: pixel size, quantum efficiency, sensor size, bit depth and frame rate. The pixel size is of importance because, in conjunction with the optics, they decide the optical and lateral sampling interval and FOV of the measurements. A modern camera has a typical pixel size around $3\ \mu\text{m}$. In combination with an objective with a magnification of $1\times$, a camera with a pixel size of $3\ \mu\text{m}$ would produce images with a pixel resolution of $3\ \mu\text{m}$. In an optimally designed system, the pixel size of the camera is at least smaller than the half of the airy disk size of the objective, which is known as the Nyquist-Shannon Sampling limit. Thus preferably we would want small pixels. When the pixels of a camera are larger than the airy disk of the optics, a system is called 'pixel limited'.

Using smaller pixels can have a drawback. The surface area and quantum efficiency (QE) of the pixel determines how much light can be converted into electrical signal. Larger pixels can gather more light in a given time period than smaller pixels. The QE determines how many of the received photons are converted into signal. A sensor with higher a QE converts more of the incoming light into signal than with lower QE. For fast image acquisition rates, gathering and converting as much light as possible within the possible exposure time is key to get source images with good signal to noise ratio. Two possibilities exist to lower the exposure time when using smaller pixels, use a camera sensor with a higher QE or add more light onto the target.

The camera sensor is a major contributor to image noise, in order to get qualitative results using SFF it is key to obtain low noise source images. As explained in the previous paragraph, adding enough light and setting the right exposure time is key for good signal to noise ratio. Additionally, the gain setting of the sensor and by extension, the readout noise of the sensor also determine part of the noise level. It is beneficial to keep the gain setting as low as possible.

The sensor size is also an important factor, because the magnification of the objective and the sensor size determine the FOV of the measurement system. For AM we want to measure areas of $100\ \text{mm}$ by $100\ \text{mm}$ and above. Consequently, to reduce the measurement time to measure these larger areas, we would like a larger FOV. Since magnification and sensor size determine the FOV, we can choose between using a lower magnification or use a large camera sensor. Choosing a lower magnification will result in a decreased lateral resolution, thus, to retain the lateral resolution of the measurement system, a larger camera sensor is preferred. However, the combination of small pixels and large sensor size results in a camera with a high number of pixels. High-resolution images require more computer memory and processing power. As a result, selecting a camera with the optimal pixel size and sensor size is a trade-off between determined by the required specifications of the measurement system. Which usually results in either high-resolution, small FOV or lower resolution and larger FOV for a similar processing speed.

The bit depth of the camera determines how much gray levels can be represented per pixel by the camera. For example an 8-bit camera has 256 different gray levels per pixel, while a 12 bit camera has 4096 grey levels per pixel. In the context of SFF microscopy, having a higher bit depth camera might be beneficial in capturing more details and nuances in the acquired images, which can be advantageous during subsequent image processing steps. However, the impact of bit depth is generally secondary to other factors such as the optical quality, resolution, and the precision of the focusing mechanism. Thus, while a higher bit depth camera can contribute to image quality, it should be considered as part of an overall imaging system rather than a stand-alone factor influencing focus variation microscopy.

Lastly Frame rate is an important factor when targeting fast measurement speeds with SFF. Since SFF requires to capture multiple images for a single measurement, higher camera frame rates directly influence SFF measurement rates.

For this research we chose to work with a Allied Vision Mako U-130B Camera with a 10-bit, 6.32 mm by 4.74 mm, 1.3 Mpixel sensor (1280x1024), 4.8 μm pixel size, a 55% peak QE and a maximum frame rate of 168fps. Ideally one would prefer pixels of 3 μm or smaller, a larger sensor with preferably a higher QE and a higher frame rate.

2.4.2 Selecting the objective

The first practical consideration to be made is the selection of the objective. For microscopy applications, we discuss three possible objective combinations that can be used for SFF:

1. Finite conjugate microscope objectives
2. Infinity corrected microscope objectives
3. Telecentric objectives.

Each objective type's advantages and disadvantages with respect to the shape-from-focus application are discussed in the following paragraphs.

Finite conjugate microscope objectives

The overall most cost-effective solution is to use a finite conjugate microscope objective lens, which directly focuses light onto a camera sensor or eye-piece (Figure 2.11). A finite conjugate objective lens has two major drawbacks which can be overcome with either additional optics or in software through multiple calibration steps. The first drawback is the curved focal plane. Due to the spherical surfaces used in the optics, when bringing the datum plane into focus in the centre of the FOV, an image point on the outside of the FOV will, most often, not be in focus. This is an effect called spherical aberration, which is common in many optics. It can be solved by introducing aspherical optical elements which can significantly increase the cost of the optical assembly. In Subsection 2.4.5 we will elaborate on a method of correcting for this aberration using calibration.

The second major drawback of finite conjugate optics is that objectives are not telecentric, meaning that when changing the focus distance, the FOV also changes. This is known as perspective error (PE). PE in object points not being in the same location when changing focus thus compromising the focus measure operation. It is possible to neglect this problem, but this results in an increase in measurement error and a decrease in the quality of the depth map.

Infinity-corrected microscope objectives

Like finite conjugate objectives, infinity-corrected optics can also be used for SFF (Figure 2.11). This solution is more expensive as not only the objectives are more expensive, but an additional lens called a tube lens is required to form an image onto the camera sensor. Infinity-corrected optics suffer from the same aberrations as finite conjugate objectives but have an important advantage. Due to the nature of the infinity correction, light rays from an object point are parallel between the objective and the tube lens. Therefore it is easy to introduce additional optical components in that region like coaxial lighting and or filters without changing the parameters of the optical system.

Telecentric

The third option is using telecentric lenses. Due to their optical design, they feature almost no spherical aberration. The telecentricity or lack of perspective error is a major benefit of these lenses. They are however the most expensive option.

The cost of microscopy objectives thus varies depending on their type and quality. Quality finite conjugate objectives, generally fall within the price range of €150 to €600. In contrast, infinity-corrected objectives, which offer advanced optical features, are typically priced between €800 and several thousand euros. Telecentric objectives, recognised for their precision and specialised capabilities, consistently exceed the €2000 mark in terms of cost.

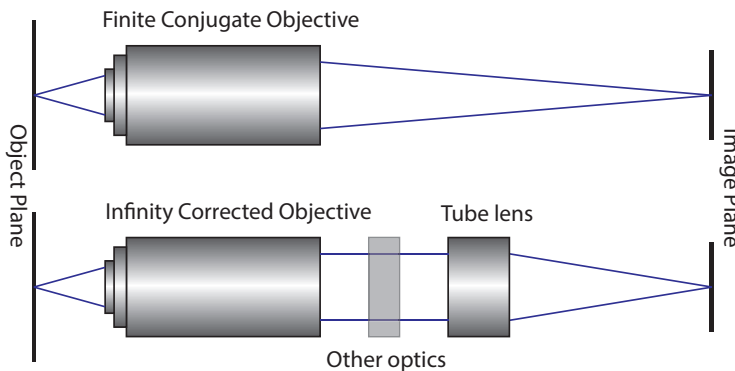


Figure 2.11: Schematic representation of a Finite Conjugate Objective versus an Infinity Corrected Objective. Infinity corrected objectives allow other optics, such as filters or beam-splitters, in the optical path, in contrast to finite conjugate objectives.

Numerical aperture is the second important parameter for objectives. SFF requires a **narrow DOF**. The DOF for a microscope objective is typically below 10 μm [57]. As discussed in Section 2.2, objectives must have a high Numerical aperture (NA) for a resulting narrow DOF.

The third important parameter of the objective is the **magnification factor**. The magnification factor is meaningful in the case of a visual microscope, where one can calculate the full magnification based on the magnification factors of the objective and eyepiece(s). It is less meaningful in the case of an imaging microscope. The objective at a specific distance in combination with a specific camera sensor size will determine the FOV that the camera sees. When this image is projected onto a display of a certain size, the full magnification of a system can be calculated. Using the same optics with a larger sensor will deliver a larger FOV. When that larger FOV is projected on the same display the magnification of the full system has decreased. The magnification factor of the objective towards the sensor, however, has not altered. Changing the distance of an objective to the camera sensor also changes the system's magnification. E.g. in this research, we use 2x and 3x microscope objectives at magnification factors lower than 1 by reducing the distance to the sensor. Thus when specifying the magnification of an imaging microscope system it is beneficial to specify the FOV and the camera sensor size S as the optics magnification M is given by

$$M = \frac{S}{FOV} \quad (2.5)$$

Another parameter to consider is the Working distance of the objective. This is defined as the distance from the objectives front lens to the target's surface when in focus. Preferably in the case of SFF for AM, we would like to have a working distance of sufficient height to overcome potential obstacles when integrating the measurement system in an AM machine. E.g. for this research we have used an Edmund Optics 0.75X MercuryTL Liquid Lens Telecentric Lens which has a minimum working distance of 85 mm.

Ultimately, the selection of the objective comes down to budget and the amount of permissible measurement error. While it is determining the the measurement accuracy and and measurement uncertainty for each type of objective is challenging as will be explained in Subsection 2.4.5.

2.4.3 Illumination

An important factor for successfully developing a shape-from-focus instrument is illumination. Both the type of illumination and the wavelength are important factors. For the illumination type, three major possibilities exist, namely: **oblique illumination, coaxial lighting or ring light illumination**. Since the the working principle of SFF relies on contrast in images to find pixels in focus, oblique illumination, where light is projected from a steep angle might be the preferred choice as it can reveal very fine surface detail. However, with oblique illumination, larger structures will cast large shadows on other parts of the object, which will affect the focus measure operation and the amount of measurement noise. The second option is using coaxial lighting, which only possible with infinity-corrected objectives. It is possible to place a beamsplitter into the optical

path in the infinity zone of such objectives. The advantage of coaxial lighting is that the FOV is always well-lit without shadows. The drawback of this method of illumination is that intricate surface details are not revealed and that it can cause specular reflection on shiny surfaces. The third option is to use a ring light. This type of light provides even lighting across a larger surface, it enhances surface texture compared to coaxial lighting.

Also the illumination wavelength is an important aspect. As can be seen in Equation 2.4, the airy disk size and therefore the resolving power of the microscope is wavelength dependent. Shorter wavelengths lead to a higher resolving power. This research does not focus on optimizing the illumination for shape-from-focus.

2.4.4 Controlling the focus distance

Shape-from-focus requires to have accurate control of the focus plane of the camera system. Two major options exist for that purpose: **translation-stage** or **tunable lenses**. Firstly there are translation-stages, described in [29] as vertical scanning. By controlling the actual height of the camera above an object with either the camera or object attached to the translation-stage one controls the position of the focus plane with respect to the object. The positional accuracy of the translation-stage, usually a few μm , will partly determine the height resolution of the measurement system. More details on the height resolution are given in Subsection 2.4.5. Another important specification of the translation-stage is the lateral stability of the carriage. In microscopy applications, a slight wiggle of the carriage can cause the resulting images to be misaligned.

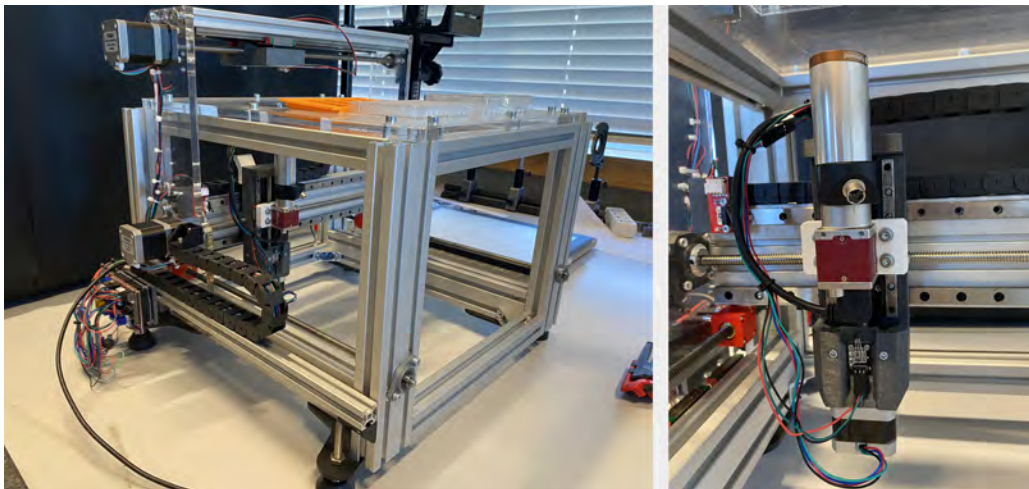


Figure 2.12: **Left:** An SFF microscope instrument using a 3D printed translation stage, developed for structure recovery of biological samples like organoids and spheroids. **Right:** The 3D printed translation-stage to create focus volumes.

Figure 2.12, shows a microscope that was created as part of this research project for the purpose of assessing the structure of biological samples, such as organoids and spheroids. This microscope incorporates a 3D printed translation-stage for vertical scanning, which offers a remarkably economical alternative (costing approximately €50) in contrast to a commercially available precision translation-stage. One limitation of the 3D printed translation-stage is that it may result, as mentioned before, in slight misalignment among the images within the focus stack. Nevertheless, this issue can be mitigated to some extent through software-based alignment techniques like phase correlation. As a result, the outcome is a highly cost-effective instrument capable of performing SFF imaging.

A second option to vary the focus plane of a camera system is to use focus tunable lenses[34]. These pieces of optical equipment are lenses that can be varied in terms of focal length. Different options exist to vary the focal length of a lens [58]. Liquid crystals can be used to change the refractive index of a medium and therefore the focal length. An optically transparent elastomer can be changed in shape, either electrically or mechanically. Or a volume consisting of transparent membranes can be filled with an optically transparent liquid and its shape can then also be controlled electronically or mechanically. For this research we selected to work with the Optotune EL-10-30C tunable lens. This lens consists of two optically transparent membranes filled with a liquid. The lens is controlled using a constant current source.

The main advantages of using tunable lenses over translation-stages is that there are no moving parts and a setup is usually a lot more compact. They are usually less expensive compared to translation-stages with similar range and precision. The biggest disadvantage is that the focus tuning range is usually limited and dependent on the objective it is combined with. Another disadvantage is the temperature dependency. Tunable lenses that are controlled electrically tend to slightly heat up when controlled. A change in temperature also causes a slight change in focal length. Therefore it is necessary to calibrate or compensate for changes in temperature. This calibration of a tunable lens is a complex procedure that involves setting the control current while simultaneously controlling the temperature of the lens. Using this procedure it is possible to produce a lookup table for a required control current given the requested focal length and the current lens temperature. The lens can then be converted to voltage control either using a voltage controlled current source or via an adc and digitally controlled current source. In the case of the Optotune lens, the calibration is done in the factory and the lens driver measures the voltage using an ADC and uses a microcontroller to control the current. This method is explored in Chapter 6.

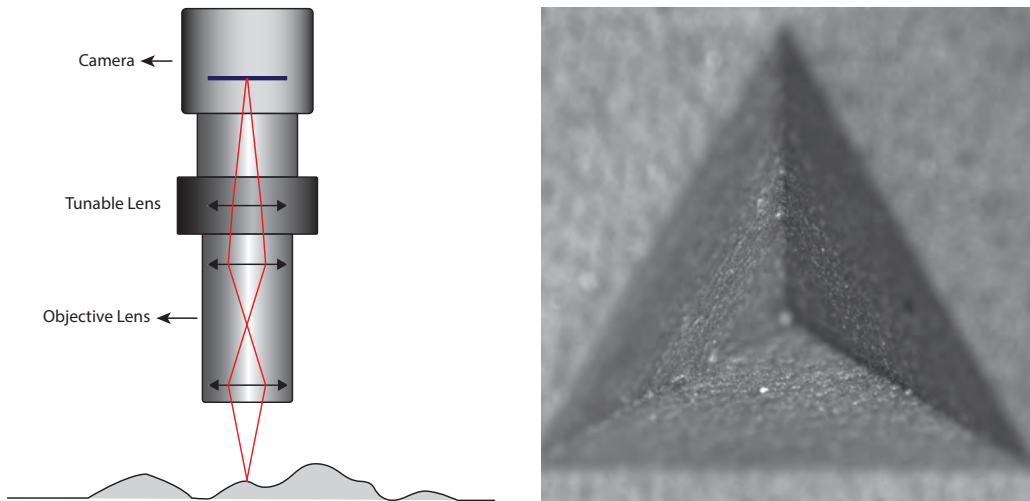


Figure 2.13: **Left:** a schematic representation of the tunable-lens-based shape-from-focus system used for this research. **Right:** an image with a narrow depth of field from such a tunable-lens-based shape-from-focus system

The last step to successfully build a working SFF setup is the synchronization between the focus control and the image capturing. In the case of a translation stage, synchronization can be done by controlling the translation stage to a specific height and then triggering the camera to capture an image. thus ensuring that the image is captured at the requested focus distance. The triggering can be done using software or trigger signals can be send by an external system. In the case of the tunable lens, the working principle is very similar. The driver is instructed to output a specific current or to hold the lens at a specific diopter setting after which the camera is triggered. This again ensures that the synchronization is kept between the focus control and the imaging. Or as in the case of Chapter 6. The triggering and control can both be synchronized using an external source.

2.4.5 Characterization and calibration of a tunable-lens-based shape-from-focus setup

Calibrating a measurement system's metrological characteristics is essential for verifying the system's specifications and subsequently comparing measurements. Additionally, the calibration process facilitates the comparison of systems produced by different manufacturers, even if these systems are based on distinct measurement principles. ISO 25178-700 [5], establishes standard procedures for calibrating, adjusting, and verifying surface topography measuring instruments. These procedures involve the use of material measures that can be traced back to the meter through a national metrology institute or a qualified laboratory. They are recommended when no other calibration procedures have been explicitly defined. ISO25178-700 encompasses the calibration, adjustment, and verification processes specifically applicable to topography measuring instruments such as SFF devices.

The metrological characteristics that are detailed in ISO25178-700, encompass all influence quantities, which are all factors that can potentially affect a measurement result. With these characteristics, it is possible to specify a measurement model which can be used to evaluate the measurement uncertainty of an instrument. It's important to note that calibration represents just one aspect of determining the overall uncertainty of a measurement. A comprehensive evaluation of measurement uncertainty includes other factors such as operator variability, variations in environmental conditions, the impact of thermal and mechanical stresses on the sample part, and other influences that aren't addressed by instrument calibrations.

In this section, we elaborate on the most basic metrological characteristics as listed in Chapter 4 of ISO 25178-600 Geometrical product specifications (GPS) — Surface texture: Areal — Part 600: Metrological characteristics for areal topography measuring methods [59]: The response function, amplification coefficient and linearity deviation in xyz , the field curvature, the measurement noise and lastly the topographic spatial resolution. More details on these calibration parameters can also be found in the work of R. Leach et al. [60].

Determining the response function, amplification coefficient a_z and linearity deviation in z

As previously discussed, SFF is based on the inherent relationship between lens focus and the distance of an object to the optical centre of a camera. Since we are measuring relative distances between object points, the absolute distance of the object to the camera is irrelevant. Yet, an accurate characterization of control input and focus distance is required. Figure 2.14 displays the results of a measurement to calibrate the focus distance of the tunable lens and microscope objective combination to varying control inputs. This measurement was done using the EL-10-30C tunable lens in combination with a 0.75x Telecentric objective from Edmund Optics and a Mako U-130B Camera.

An electronically tunable lens in combination with any objective has an unknown relationship between focus distance and control signal. Additionally, the response of the lens to a linear input is not necessarily linear. This relationship is defined as the response function of a measurement system. The amplification coefficient a_z defines the slope of the linear regression of the response function.

To determine this response function, we can put different gauge blocks with calibrated height under the SFF camera. Next, the maximum focus position for each gauge block height is determined by creating a focus volume and calculating a focus curve in the centre of the volume. To reduce the amount of noise on the signal, the average focus curve of a group of pixels in the centre of the image is preferred. We can plot these focus curves in relationship to the control signal (Figure 2.14a). The maximum of each focus curve determines the focus position for a given height and control signal. From these measurements, we can also determine the linearity of the lens's response (Figure 2.14b). To analyse the linearity of the measurements, we execute a linear regression to find the best fitting linear function. As mentioned above, the slope of this function denotes the amplification coefficient. In order to determine the actual linearity of the response function, we calculate the Pearson correlation coefficient between the response function and the linear regression, which returns a value between 0 and 1 to describe the linearity

of the data, with 1 being perfectly linear. The measurement of the lenses response function showed a correlation coefficient of 0.99993, from which we can conclude that the response function can be considered to be linear.

Given that the calibration process establishes the response function for a linear input and this response function is subsequently applied to process the measurements, the amplification coefficient becomes practically one. This method has a small drawback. Gauge blocks typically have polished reference surfaces that cannot be measured using SFF. To overcome that issue, an object with a flat, yet textured surface is placed on top of the gauge blocks. An example of such an object is the ground side of a larger gauge block. Reusing that block for every measurement guarantees a constant offset to the measurements. Thus, this additional gauge block has no effect on the calibration step.

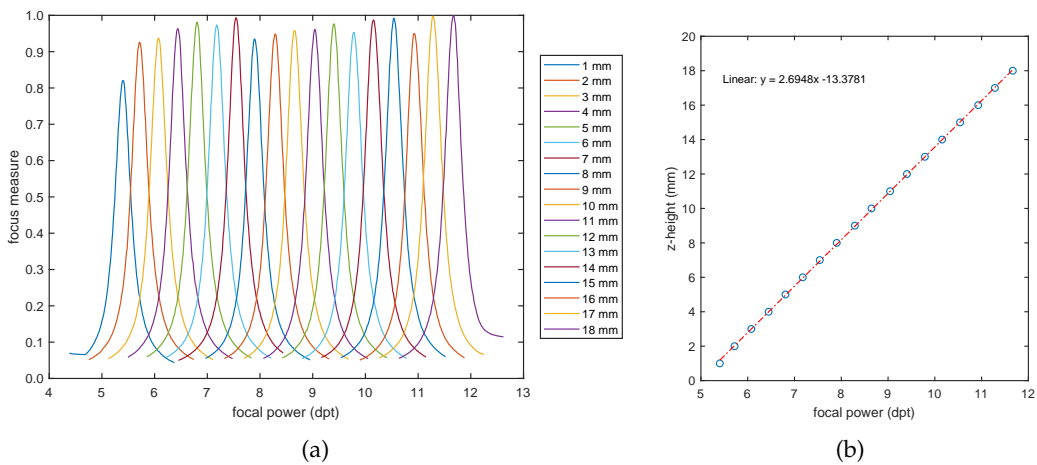


Figure 2.14: **Left:** The focus curves of measurements for focus distance calibration **Right:** Linearity analysis of these measurements by plotting the located maxima vs. the actual gauge block height.

Determining the amplification coefficients a_x and a_y in x - and y -direction

The previous calibration step sets the response function of the measurement system in the z -direction. Yet, for accurate areal topography measurements, the scale and deviations in the lateral directions must also be calibrated. a_x and a_y are equivalent to a_z and are the result of a linear regression on the calibration in lateral directories. According to [5], the default method to determine these characteristics is by using measurements of material measures with calibrated distances in the xy -plane. A precision checkerboard (Figure 2.15a) can be used for this purpose. We used one from Edmund Optics (PN #12-198), printed on opal, with 0.4 mm sized checkers with a precision of 0.002 mm. A checkerboard is a calibration target consisting of a pattern of alternating white and black squares with known sizes.

To calibrate the SFF measurement system using a checkerboard, the calibration target is placed under the measurement system and put into focus using the tunable lens. Next, an image is acquired. That image is then processed using a checkerboard detector

algorithm, which will find the points where squares of the same colour touch. These detected points are called checkerboard points. We assume that the response function in the lateral direction is linear by default. Thus, from the detected checkerboard only the outermost points are used (Figure 2.15b) for the calibration. The Euclidean distance (in pixels/image coordinates) between points on the same row or column is calculated. The actual distance between the same points in real-world coordinates is calculated by counting the amount of checkers in between the points and multiplying it by the size of the checkers. The lateral scale in mm/pixel is then calculated by dividing the real-world distance between two points by the pixel distance. The FOV is then calculated by multiplying the size of the image in pixels with the lateral scale. It is important to mention that the lateral scale is not equal to the lateral resolution of the measurement system.

The amount of distortion in the xy -plane can also be calculated using the detected checkerboard points. This method of calibration can also be used to significantly reduce the effects of perspective error that finite conjugate and infinity-corrected objectives exhibit. The lateral scale and by extension the measurement system's FOV can be measured on multiple focus distances. With that information, it is possible to crop and scale the images of a focus volume to retain the lateral scale over the full measurement range.

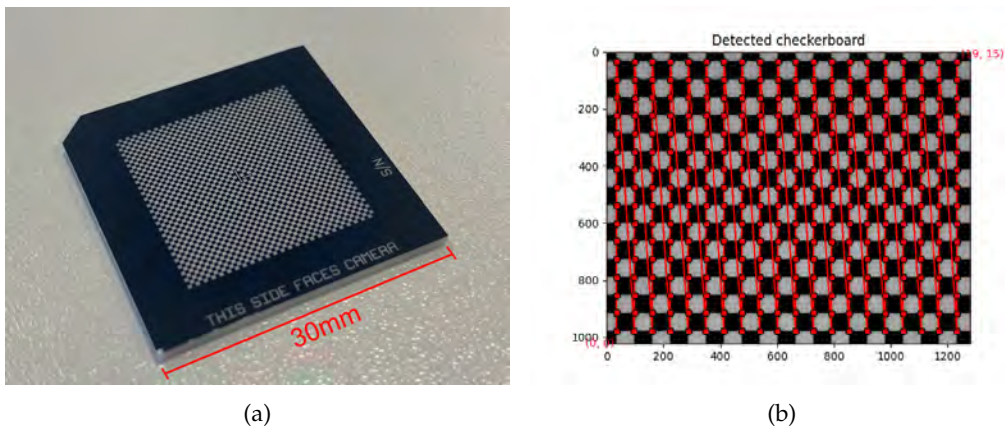


Figure 2.15: **Left:** A precision checkerboard with 0.4 mm sized checkers with a precision of 0.002 mm **Right:** A section of the checkerboard as viewed by the measurement system using the Mako U-130B, the EL-10-30C and the Edmund Optics 0.75x telecentric lens.

The measurement characteristics that are determined using the calibration method detailed above, are determined on the 2D source images, and not on the depth map or point cloud of the processed measurement. As such it is possible that this determination of the measurement characteristics is less accurate. A second possible method for calibrating the lateral scale is described in the works of Alburayt et al. [61]. Using a calibration target with precise hemispherical calottes (Figure 2.16), it is possible to determine the distance between two or more calottes by fitting spheres in the point cloud of the measurement. The lateral scale is then determined in a similar way to the method described above by dividing the real-world distance between two calottes by the distance found in the measurement. Yet, the advantage is that the calibration is performed on the actual 3D measurement.

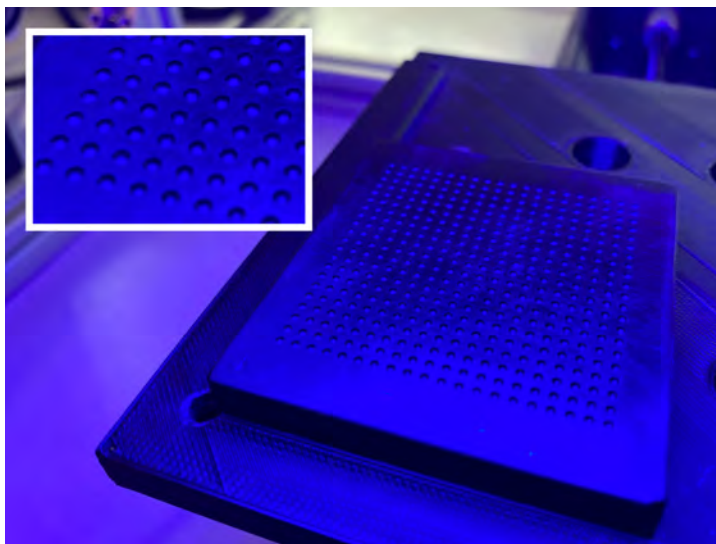


Figure 2.16: Calibration target with hemispherical calottes used for calibrating the amplification coefficients a_x and a_y as proposed by [61]. The inset image shows a closeup of the calottes

Determining and correcting field curvature

It has been established in Subsection 2.4.2 that finite conjugate objectives often suffer from a curved focal plane also called field curvature. This is an example of an optical aberration that causes flatness deviation on individual measurements as the the curved focal plane results in an incorrectly measured focus distance for points on the edge of the FOV compared to the center of the FOV.

Thus, when an individual measurement of a flat reference standard is made using an objective that exhibits a curved focal plane, the resulting depth map will be curved. This curved depth map describes the field curvature but can also be used to correct it by subtracting that measurement from subsequent measurements. Although it is possible to correct the field curvature using the measurement of the flat reference directly as described in [34]. This will likely increase the amount of measurement noise. The method provided by Angot-Petit et al. can be improved by fitting a 2D curved plane in the measurement data of the flat reference.

Ideally, as described in [5], a measurement standard is preferred to be optically smooth. However, if the measurement principle requires a textured surface, as is the case with SFF, the flat reference standard does not need to be optically smooth. Preferably we would use a roughness flatness standard. This research used the ground side of a gauge block, as it provides a flat and textured surface. The flatness of this gauge block side was measured to be within 0.001 mm using a dial indicator (Figure 2.18). Figure 2.17a shows the curved surface of a measurement using the Mako U-130b, the Optotune EL-10-30C and the mitutoyo 3x finite conjugate objective. The z-scale in this figure is exacerbated for viewing purposes. After quadratic regression, the correction map can be generated (Figure 2.17b).

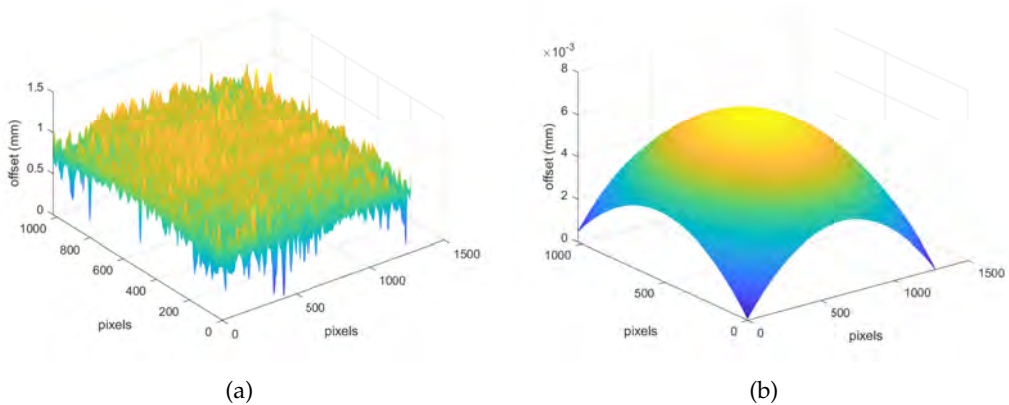


Figure 2.17: **Left:** Result of an unfiltered measurement of a flat surface to calibrate the curved focal plane. **Right:** Correction map after quadratic regression.



Figure 2.18: Measurement of the flatness of the ground side of a gauge block using a dial indicator to serve as flat calibration object.

The flatness deviation as represented in Figure 2.17, is thus presumably caused by the Mitutoyo 3x Compact objective. Yet, The focus tunable lens (Optotune EL-10-30C) could also cause some additional curvature of the focal plane. By replacing the focus tunable lens in the optical assembly with a spacer, it is possible to evaluate which of the optical elements is the major contributor to this curved focal plane. Unfortunately due to time constraints, this analysis was not carried out for this research.

The approach described above is a first order approach to correct for the curved focal plane. Yet, the curvature of the focal plane might be different at different focal distances. Thus a more advanced method to correct the curved focal plane should be researched.

Measurement noise

Any measurement system induces a specific amount of noise in the measured quantity. In the case of an SFF system, measurement noise can be caused by unwanted optical reflections, noise induced by the camera sensor or other electronics and more. Among other quantities, measurement noise is one of the contributors to measurement uncertainty. Thus, for an accurate determination of measurement uncertainty, the measurement noise must be determined. One of the proposed methods, in ISO 25178-700 [5], to estimate the measurement noise is the subtraction method. By subtracting two consecutive measurements of the same subject under similar ideal conditions, the resulting depth map only contains measurement noise.

The estimated measurement noise N_M is then calculated using Equation 2.7, where S_q is the RMS of the values of the subtracted measurements, as defined in ISO25178-2 [62] and Equation 2.6. For Equation 2.6, $z(x, y)$ is defined as the measured height at location (x, y) and A is the measurement area. Since any form of filtration, analogue or digital has an influence on the measurement noise, the measurement noise is highly dependent on the focus measure operator and its window size that was used for the measurement.

$$S_q = \sqrt{\frac{1}{A} \iint_A z^2(x, y) dx dy} \quad (2.6)$$

$$N_m = \frac{1}{\sqrt{2}} S_q (z_1(x, y) - z_2(x, y)) \quad (2.7)$$

Topographic spatial resolution and instrument transfer function

The Topographical spatial resolution in surface metrology refers to the smallest discernible feature or detail that can be accurately measured and represented on a surface. It indicates the level of detail that an instrument can capture and is determined by factors such as measurement technology, sensor resolution, and sampling interval. ISO 25178-700 [5] does not provide details on calibration methods to determine the topographic spatial resolution. As, according to ISO 25178-600:2019, 3.1.20 [59], the topographic spatial resolution can be quantified by several parameters such as but not limited to: the lateral resolution, the width limit for full height ratio, the Rayleigh criterion, the Sparrow criterion or the Abbe resolution limit.

The most suitable method for determining the topographic spatial resolution, according to ISO25178-600:2019, depends on the application and method of measurement. These parameters provide only one figure to determine a system's ability to resolve detail. A more useful way to describe a system's response to the variations in spatial frequencies is the Instrument Transfer Function (ITF). In simpler terms, it represents how well an instrument can detect and faithfully reproduce different spatial features of a surface. For surface metrology instruments, such as profilometers or SFF instruments, the surface texture data is often obtained in the form of a profile or a depth map. The ITF characterises how the instrument responds to different spatial frequencies present in this depth map.

Ideally, an instrument should have a flat or constant ITF, meaning it would respond uniformly to all frequencies and accurately capture the surface features. However, in reality, all instruments have limitations, and their ITF may exhibit variations with frequency, causing some frequency components to be measured less accurately than others.

One way to determine the approximate ITF is to model it based on the parameters of the optical system. A method to theoretically quantify an instrument's response based on a series of varying isolated sinusoidal topography patterns is provided in the work of P. de Groot et al. [63]. They also state that not only the optical components influence the ITF. As clarified in Subsection 2.4.1 in the ideal situation, the camera's pixel size is much smaller than the airy disk size of the optics to avoid undersampling in accordance with the Nyquist sampling limit. Yet, some optical instruments, usually with low magnification, are 'pixel limited' which means that their pixels are larger than the airy disk size. In this case, it can be assumed that the width of the pixel is the same as the lateral sampling interval of the instrument. In this situation, it is straightforward to determine the theoretical ITF using the Fourier transform of Equation 2.8, where ν is the spatial frequency and D is the sampling interval or pixel resolution.

$$f_{CAM}(\nu) = \frac{\sin(\pi\nu D)}{\pi\nu D} \quad (2.8)$$

However, in a pixel limited system, surface patterns with a spatial frequency exceeding half the sample frequency (Nyquist), defined by the pixel size, may result in interference and aliasing, potentially introducing inaccuracies in the measurements. In the case that the pixels are sufficiently small compared to the airy disk of the optical system, the modeling of the ITF is a complex method in itself and still only provides a theoretical maximum response for the instruments. However, in reality, an instrument can exhibit various optical aberrations that limit the ITF. Therefore, as explained in [63], a calibration by means of 'material measures' is in line with the traditional calibration framework for dimensional metrology. In short, calibration artefacts are traditionally used to determine the measurement characteristics.

The most suitable set of material measures for ITF determination comprises certified sinusoidal gratings spanning a range of amplitudes and frequencies that fall between the instrument's measurement noise and its maximum slope limits. This set of material measures could be used independently of the measurement method. However, producing such an extensive set of material measures is highly impractical. Therefore, a variety of other material measures have been proposed to determine the ITF. For example:

- A binary pseudo-random pattern [64]
- A chirped sinusoid pattern [65]
- An fully random surface [66]
- A Topographical star pattern [67]

These material measures are discussed in [63] and their respective advantages and disadvantages are compared. However, a definite way to accurately determine the ITF for SFF instruments, at the time of writing of this dissertation, is yet to be established.

2.4.6 Measurement target

In order to validate the proposed methods in this dissertation, A specific target has been designed based upon a portable characterization target (PCT) [68, 69] (Figure 2.19). It measures 100 mm by 100 mm and uses different shapes and features to do a complete characterisation of a measurement system. The target was printed in TiAl6V4 using powder bed fusion to have a representative surface for AM in terms of surface roughness, colour and reflectivity.

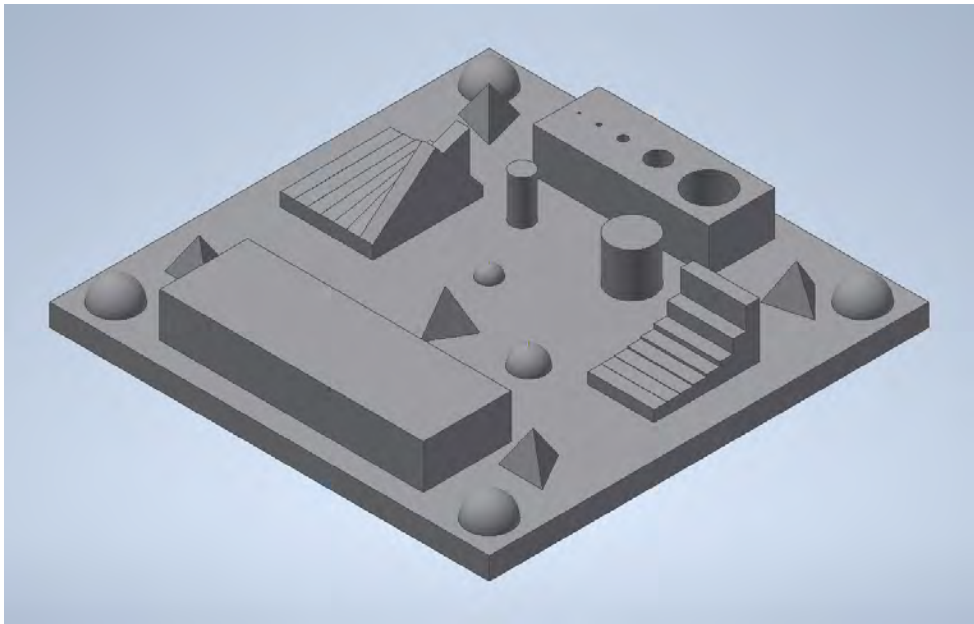


Figure 2.19: The 3D printed calibration target based on the PCT of [68, 69]

The target contains the following items with a similar function as described in [68]:

- 6 hemispheres: In the measurement of a spherical surface, it is possible to find the best fitting sphere. This fitted sphere has a diameter and centre point. With the information on the different spheres it is possible to gain knowledge about the measured form and dimensionality errors across the entire target.
- 2 cylinders: Using cylinders it is possible to find errors in the measured form by fitting a circle. Additionally knowledge is gained about the steepness of the angles that can be measured from any direction.
- 6 Tetrahedrons: used for corner localisation and dimensionality error over the whole target.
- two cuboids: Used to assess uni-directional and bi-directional plane spacing errors.
- A staircase: This item can be used to gain knowledge on the height resolution by fitting planes on each level and measuring the inter-plane distances.

- A collection of angled blocks: These can be used to determine the angle error of measurements by fitting planes through the top surfaces of the blocks in measured point cloud.
- A set of cylindrical holes: To determine the form of measured holes and determine the smallest hole that can be measured.

To fully use this 3D printed target and its artefacts for the purpose for which it was designed, it should first be calibrated. Due to the unavailability of a device capable of measuring this large target to the required precision, the actual form of the different artefacts was not known for this research. For example a printed sphere includes the printing errors and thus might not be spherical. This can then lead to inaccurately determined measurement errors. Therefore, only a single artefact (tetrahedron) was used to validate the methods that were tested in this research. Other artefacts were measured during the research but not analytically compared during the research.

2.5 Conclusion

This chapter presented a comprehensive introduction to the fundamental idea of shape-from-focus (SFF), covering its basic optical principles and methodology. We delved into crucial considerations when developing and deploying a tunable-lens-based SFF setup, including the selection of components and parameters for focus measure operators. The significance of calibration and characterization, in line with reference standards, was thoroughly examined and emphasised as a pivotal aspect for achieving precise and dependable measurements using any measurement system.

2.5.1 Final component selection

* We ended up selecting the following components for this research:

- **Camera:** Allied Vision U-130B
- **Tunable Lens:** Optotune EL-10-30C with Optotune Driver 4i
- **Objectives:** EO Techspec CF 2x (#88-352), EO Techspec CF 5x (#88-353), Mitutoyo 3X Compact Objective (#56-990), EO MercuryTL 0.75x Telecentric Objective (#36-192)
- **Translation stages:** 2x Zaber X-LSQ300B

Optimising shape-from-focus processing using phase correlation

The previous two chapters aimed to provide the reader with sufficient background information to comprehend the scientific contributions that were accomplished. This chapter is the first contribution to SFF and introduces an improvement in the processing step of SFF to improve the quality of generated depth maps.

The scientific contribution described in this chapter was published in: *Gladines, J.; Sels, S.; De Boi, I.; Vanlanduit, S. A phase correlation based peak detection method for accurate shape from focus measurements. Measurement, 2023, Volume 213, 112726, ISSN 0263-2241, <https://doi.org/10.1016/j.measurement.2023.112726>.*

3.1 Introduction

As has been established in Chapter 2, the limited measurement speed is the most important drawback of the shape-from-focus (SFF) method for online AM monitoring. As an example, the profile measurement of a 3 by 3 cm target using a commercial device (Keyence VHX-1000) required roughly 3h with a 1.6 by 1.4 mm FOV. An important contributor to the measurement speed is the need to capture and process multiple images, typically somewhere in the range of 50 to 200 images. The capturing of these images can be improved by using high-speed cameras in combination with electronically tunable lenses or specific high-speed translation stages. Therefore, gains need to be made in SFF processing to improve the measurement speed. As stated in Chapter 2, the typical processing chain consists of applying a focus measure operator (FMO) [70, 71, 72] to each of the captured images and then reducing the focus measured image volume to a 2D depth map by locating the maximum pixel focus for each pixel within the set of focus measured images. Since the introduction of shape-from-focus, most research in terms of processing has concentrated on improving the quality of the depth map, by using much more complex processing algorithms at a much higher computational cost. The problem with depth map quality is caused by image noise (a combination of quantization noise and thermal noise from the capturing process), magnification effects and quantization errors due to the discrete set of focus levels. This results in noise in the focus measure

and causes the depth map to be erroneous and inaccurate [73]. Furthermore, the signal-to-noise ratio of the focus measure operation is reduced when measuring objects with low surface texture. This makes it difficult to find the true location of the maximum pixel focus for each pixel.

One simple approach to reduce noise in the focus curve is to use a larger window size for the focus measure operator. This reduces the effects of image noise and low surface texture, yet results in blurred and overall lower quality depth maps [41] and does not overcome the discrete set of focus levels. Other methods enhance the robustness of focus measure operators to noise by including the 3D neighbourhood around a pixel in the focus measure operation [74]. Curve fitting methods are another way to circumvent the noise from the focus measure operation. They try to find the mathematical function to best describe the focus curve from the measured data points. In addition to being more robust to noise, these methods can also overcome quantization noise, introduced by the discrete set of focus levels. Since pixel focus values traditionally follow a Gaussian-like curve, Gaussian fitting of the measurement data was proposed to improve accuracy [75]. Over the years, many other methods like polynomial fitting [76] or polynomial regression [77] have been proposed. Other, more accurate yet more complex methods using Gaussian process regression [41, 42] and neural networks [78, 79] also exist, yet they have many more parameters and a high training and computational cost.

Here, we propose a simple method that provides more accurate depth maps than easy-to-implement methods such as the index of the maximum focus value (argmax), Gaussian-fit [75], quadratic-fit [73] and centroid detection [80] to be at least equally computationally inexpensive. We introduce a reduction method based on a fast phase correlation algorithm [81, 82, 83]. Using Amplitude correlation or normalized cross correlation could be an alternative strategy as amplitude correlation is usually more robust to random noise. Yet, amplitude variations in the focus curves are expected based on variations in surface texture and illumination and could impact the accuracy of amplitude correlation. The rest of this chapter is organised as follows: in Section 3.2 the process of finding the maximum pixel focus is explained in more detail. Section 3.3 discusses the new phase-correlation-based method for reducing SFF data, The validation methods and experimental setup are described in Subsection 3.4.1. Finally, Section 3.5 reviews the results of the analysis of synthetic and measurement data in comparison to the existing methods.

3.2 The focus curve

The pixel focus values usually follow a Gaussian-like curve (Figure 3.1a). Unfortunately, due to image noise, low surface texture and due to the discrete set of images in measurements, a real focus curve contains more noise (Figure 3.1b). Thus, finding the true focus point is not as simple as finding the index of the maximum point in the focus curve.

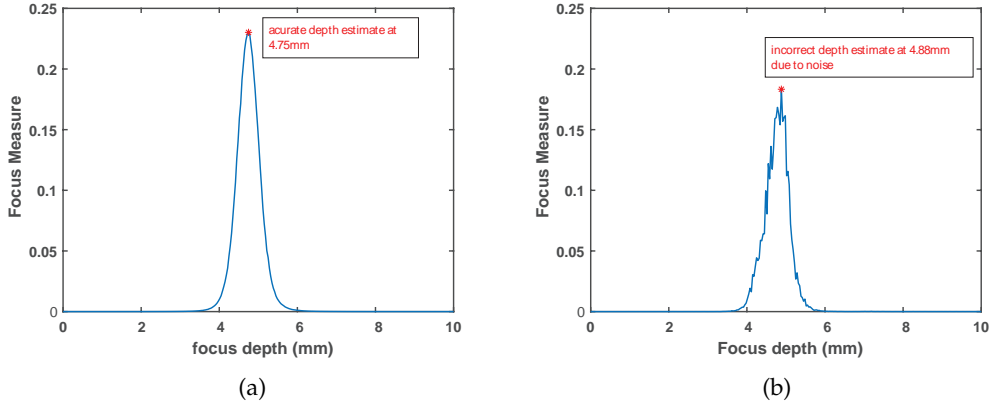


Figure 3.1: (a) An ideal Gaussian-like focus curve, created by averaging the focus curves of multiple pixels from a measurement of a flat surface. (b) The noisy single pixel curve from the centre of the flat surface. The measurements were taken using the setup described in Subsection 3.4.2

Since a focus curve of a single measurement point or pixel appears Gaussian-like, curve fitting with a Gaussian function leads to improved depth maps as proposed by Nayar et al. [75]. To reduce the computational overhead from curve fitting, Gaussian fitting on SFF depth maps was proposed in [75] with only three points: the maximum of the focus curve and a point at a specific distance left and right of the maximum. It is stated in [75] that the determination of this distance to the maximum has to be determined empirically. The important notice is that all points must lie on the peak of the focus measure. The three selected points on the focus curve y of a single measurement point can then be used to find the average value for the Gaussian fit using the following equations [56]:

$$c = \frac{(y_1 - y_2) \cdot (x_2 - x_3) - (y_2 - y_3) \cdot (x_1 - x_2)}{(x_1^2 - x_2^2) \cdot (x_2 - x_3) - (x_2^2 - x_3^2) \cdot (x_1 - x_2)} \quad (3.1)$$

$$b = \frac{(y_2 - y_3) - c(x_2 - x_3) \cdot (x_2 + x_3)}{(x_2 - x_3)} \quad (3.2)$$

$$\sigma = \sqrt{\frac{-1}{2c}} \quad (3.3)$$

$$\mu = b \cdot \sigma^2, \quad (3.4)$$

with (x_1, y_1) , (x_2, y_2) , (x_3, y_3) being the three points on the focus curve of used to fit the Gaussian, σ and μ being the standard deviation and the average of the Gaussian. The improved measure for pixel depth is μ . One might notice that Equation 3.3 can produce complex numbers. Yet The outcome of Equation 3.3 is squared in Equation 3.4 which returns them back to real numbers.

The same three points can also be used for a quadratic fit with Equations (3.5), (3.6) and (3.7), where z is the specific pixel depth.

$$a = \frac{(y_3 \cdot x_2 - x_3 \cdot y_2 + y_1 \cdot x_3 - y_1 \cdot x_2)}{((x_2(x_3^2)) - (x_3(x_2^2)))} \quad (3.5)$$

$$b = \frac{y_2 - a(x_2^2) - y_1}{x_2} \quad (3.6)$$

$$z = \left(\frac{-b}{2a}\right) + x_1 \quad (3.7)$$

Another common approach to true peak detection is centroid detection (Cent) which can be calculated using Equation 3.8.

$$z = \frac{\sum_{d=0}^{N-1} y_d \cdot k}{\sum_{d=0}^{N-1} y_d} \quad (3.8)$$

with z being the depth of the pixel, N being the number of images, y_d being the result of the focus measure of a certain measurement point of the image at position d in the volume and k being the corresponding relative focus distance of that image. In the following section, we introduce a new method to find pixel depths based on phase correlation.

3.3 Shifted phase correlation

Phase correlation (PC) is a method that is usually employed in image registration and alignment [81, 82]. It can precisely discern the relative distance between two images on a sub-pixel level, even when the images contain a lot of noise. It uses frequency information of the data that is extracted by applying a Fast Fourier Transformation. In our case, the PC algorithm is used to find the relative distances in 1D data instead of 2D images. Applying phase correlation to 1D datasets is not uncommon as shown in [84, 83]. After applying the focus measure operator to the input images, a discrete Fourier transform is applied to the focus volume. This allows the extraction of phase information from the pixel focus value curve. The method takes advantage of the fact that noise is uncorrelated compared to pixel focus values, which makes the method more robust to noise. Even though PC is a precise method, when the relative distances between signals increase, the precision decreases. This decrease in precision is because for higher frequencies the phase angle can wrap leading to uncertainty in the true phase of these signals. Therefore we opted to first shift the data so the peaks are roughly aligned. Then we execute the phase correlation algorithm to precisely find the distances between the peaks and lastly reverse the initial integer shift (Figure 3.2). The next paragraphs describe a step-by-step explanation of the shifted phase correlation (SPC) method.

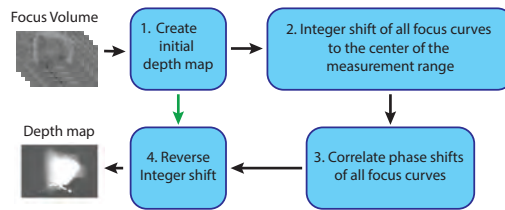


Figure 3.2: Flow chart, visualising the process of processing the focus volume to a depth map using SPC. The green arrow shows that the data from the initial depth map is used to reverse the shift if the focus curves. For PC, steps 1, 2 and 4 are skipped.

1. Initial depth map:

As a first step, an initial rough depth map is created by finding the integer index for the maximum focus values for every pixel using argmax . This initial depth map is first filtered using a 10 by 10 median filter to replace outlier pixels with values similar to their surroundings as the example shown in Figure 3.3. This filtered map will then be used to shift the peaks of the focus curves to the centre of the range.

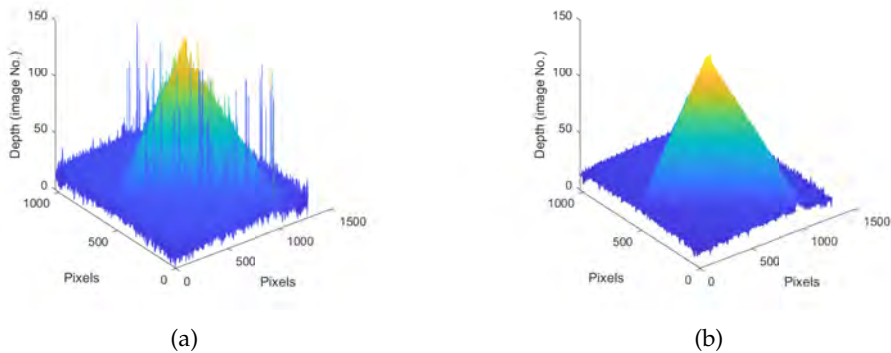


Figure 3.3: (a) An example initial depth map, with incorrect pixels due to noise in the focus curves, from the tetrahedron on the 3D-printed calibration target in Figure 3.7a, (b) The median filtered initial depth map, to be used for the integer shift.

2. Integer shift:

The corrected initial depth map is then used to circularly shift the data to approximately align all peaks in the centre of the measurement range (Figure 3.4). This ensures that the relative shift of the focus curve of all pixels is small, which will result in a more accurate depth estimate.

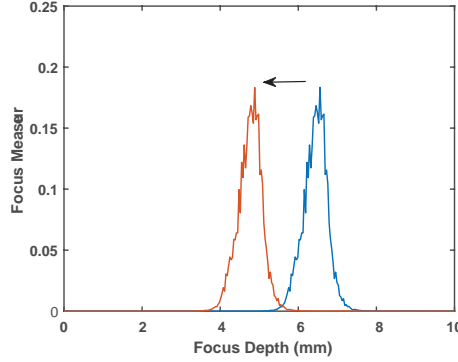


Figure 3.4: Focus curve of a pixel from a true measurement (blue curve), is circularly shifted over 50 samples to the left (red curve) so the peak of the curve is approximately centred in the measurement range.

3. Phase correlation:

To calculate the relative sub-pixel shift between pixels, a phase correlation algorithm is used. We represent the ideal focus curve in the centre of the measurement range by $F(d)$ where d represents the focus depth. Based on the Fourier Shift theorem, we can assume the following relationship for any of the other pixels $F'(d)$.

$$F'(d) = F(d + \Delta d) \quad (3.9)$$

where Δd is the relative shift between the focus curves. To find Δd we first need to compute the fast Fourier transform of $F(d)$ and $F'(d)$:

$$\mathfrak{F}(m) = \sum_{n=0}^{N-1} F(d_n) e^{-\frac{2\pi i}{N}(n-1)(k-1)}, \quad m = 1, 2, \dots, M \ll N \quad (3.10)$$

$$\mathfrak{F}'(m) = \sum_{n=0}^{N-1} F'(d_n) e^{-\frac{2\pi i}{N}(n-1)(k-1)}, \quad m = 1, 2, \dots, M \ll N \quad (3.11)$$

where N equals the number of images that are being used for the measurement, m represents the Fourier spectral lines that are calculated for this analysis and M is an arbitrarily chosen value with the following restriction $M \ll N$ as only the first few spectral lines will contain information due to the nature of the focus curve signal. For each integer value of n , we can then calculate the Δd with the following equation:

$$\Delta d(n-1) = (\angle \mathfrak{F}'(n) - \angle \mathfrak{F}(n)) \frac{Nn\delta d}{2\pi}, \quad n = 2, \dots, M \ll N \quad (3.12)$$

The first spectral line ($n=1$) is disregarded as this is the DC component of the Fourier transform. Theoretically, we can calculate multiple spectral lines $n = 2, \dots, M$ and select the median value as δd . Using more spectral lines can increase the accuracy

of the phase correlation step. In reality however, we only calculate the Δd for based on the second spectral line $n = 2$. The noise in the focus curves will have a larger influence on the higher order components making them less reliable, especially when Δd increases. This calculation is executed for every pixel resulting in a depth map that shows the non-integer relative shift between the pixels.

4. Inverse shift:

As a final step, the integer shift that was applied to the data must be reversed. This is realised by adding the inverse filtered initial depth map to the result of the phase correlation step. This is represented by the green arrow in Figure 3.2.

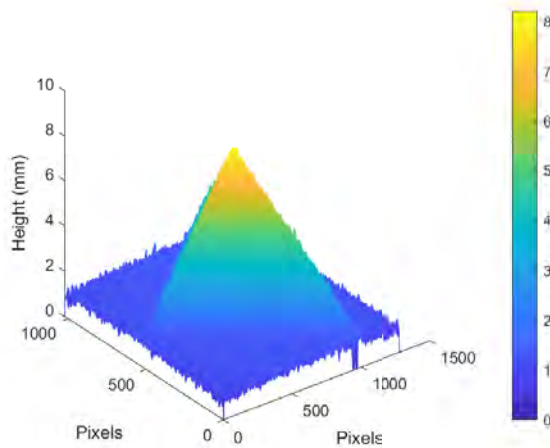


Figure 3.5: Final improved depth map with the shifted phase correlation method

3.4 Experimental setup

The proposed method is tested using a lab experiment to determine the accuracy of the produced depth maps. The evaluation methods are described in Subsection 3.4.1 and Subsection 3.4.2 discusses the experimental procedure and the hardware that was used.

3.4.1 Evaluation methods

To evaluate the effectiveness of the proposed shifted phase correlation method, we compare its performance to the described, well-known and commonly used techniques, namely: the index of the maximum focus value, also known as argmax , Gaussian fit [75], quadratic fit [73], centroid finding [80] as well as to regular phase correlation without the initial shift. The performance of these methods is tested by comparing generated depth maps to a common reference. The analysis is first carried out for synthetic data. Next, to verify each method's robustness to noise, zero mean Gaussian white noise with a 0.005

variance was added to the synthetic source images. New depth maps were then generated from these noisy source images and subsequently compared to the same reference. Lastly, the methods are compared for their performance on real-world measurements. The synthetic data is generated using a simulation tool [85, 86] that takes a textured image and camera parameters and applies a point spread function (PSF) to simulate focus in accordance with a given depth map. With this tool, a sequence of 60 images, each 300x300 pixels, was generated to simulate a focus volume as if it would have been measured on a sinusoidal shape. The depth map that was used to generate the synthetic data, (Figure 3.6), can also be used to analyse the quality of the reproduced depth maps quantitatively.

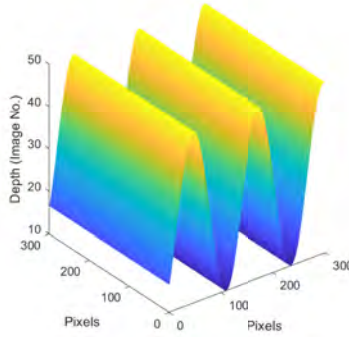


Figure 3.6: Reference depth map of the synthetic data.

Three commonly used evaluation metrics [41, 87, 71, 79], are employed to examine the condition of the reproduced depth maps to the reference. The first metric is the Root Mean Square Error (RSME), which averages the squared absolute differences between the estimated depth map and the reference:

$$RSME = \sqrt{\frac{1}{XY} \sum_{x=1}^X \sum_{y=1}^Y (\hat{D}(x, y) - \mathcal{D}(x, y))^2}, \quad (3.13)$$

with $\hat{D}(x, y)$ and $\mathcal{D}(x, y)$ respectively being the generated depth map and the reference and X and Y being the width and height of the depth map in pixels. The RMSE measures discrepancy or error between two datasets. Thus a lower RSME implies a better resemblance to the reference. Secondly, we calculate the correlation coefficient (CORR) between the generated depth map and the reference. A higher correlation coefficient indicates a better similarity of the depth map to the reference. The correlation coefficient is calculated in the following way:

$$CORR = \frac{\sum_{x=1}^X \sum_{y=1}^Y (\hat{D}(x, y) - \bar{D})(\mathcal{D}(x, y) - \bar{\mathcal{D}})}{\sqrt{\sum_{x=1}^X \sum_{y=1}^Y (\hat{D}(x, y) - \bar{D})^2 \sum_{x=1}^X \sum_{y=1}^Y (\mathcal{D}(x, y) - \bar{\mathcal{D}})^2}}, \quad (3.14)$$

Lastly, we can employ the Peak Signal-to-Noise ratio (PSNR) [16], which is defined as the ratio between the highest possible value of a signal and the power of the corrupting noise, expressed in decibels. A higher PSNR suggests the estimated depth map is of better quality.

$$PSNR = 20 \log(MAX_d) - 10 \log\left(\frac{1}{XY} \sum_{x=1}^X \sum_{y=1}^Y (\hat{D}(x, y) - \mathcal{D}(x, y))^2\right), \quad (3.15)$$

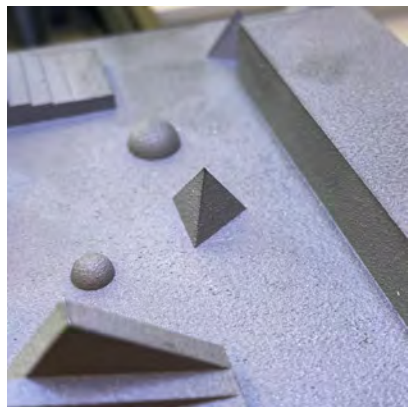
where MAX_d is the maximum possible value that can be represented in the depth map.

3.4.2 Used hardware and measurement procedure

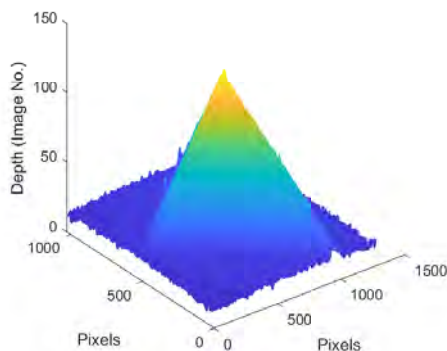
As described above, the performance of the methods is also analysed with real-world data. Measurements of the tetrahedron on the calibration plate (Figure 3.7a) were used for this purpose. The measurements were made with a setup consisting of the following components:

- Mako U-130B 1.3Mpix Monochrome Camera
- Optotune EL-10-30C Tunable lens [88] for focusing
- Mitutoyo 3x finite conjugate microscope objective

Although no real reference depth map of the tetrahedron is available, we can still evaluate the effectiveness and robustness to noise of the methods by creating a low noise high-quality depth map using a combination of multiple measurements. Systematic errors are reduced by averaging 9 measurements of the same object with the camera position of each measurement slightly offset from previous measurements. The 9 measurements were aligned using phase correlation before averaging. Additionally, the base images of these 9 measurements are also the result of averaging 5 images to reduce measurement noise. Therefore we can use the same evaluation metrics to compare a single non-averaged measurement to this low noise depth map (Figure 3.7b).



(a)



(b)

Figure 3.7: (a) The original real-world tetrahedron, with 10 mm base and 8.165 mm height, on the calibration plate, (b) the low noise depth map created with the method described in Subsection 3.4.1.

We present and discuss the results of these experiments in the following section and give a normalised overview of the computation times for these different methods.

3.5 Results and discussion

3.5.1 Comparison using synthetic data

Firstly, we consider the depth maps of the synthetic data set without noise (Figure 3.8). It is difficult to visually detect differences in quality between the depth maps generated by the different methods. Comparing these depth maps to the reference depth map (Figure 3.6), one can immediately notice some patterned artefacts. These artefacts can be attributed to the selected FMO, Tenengrad Variance [43], and the size of the focus measurement window (5×5 pixels).

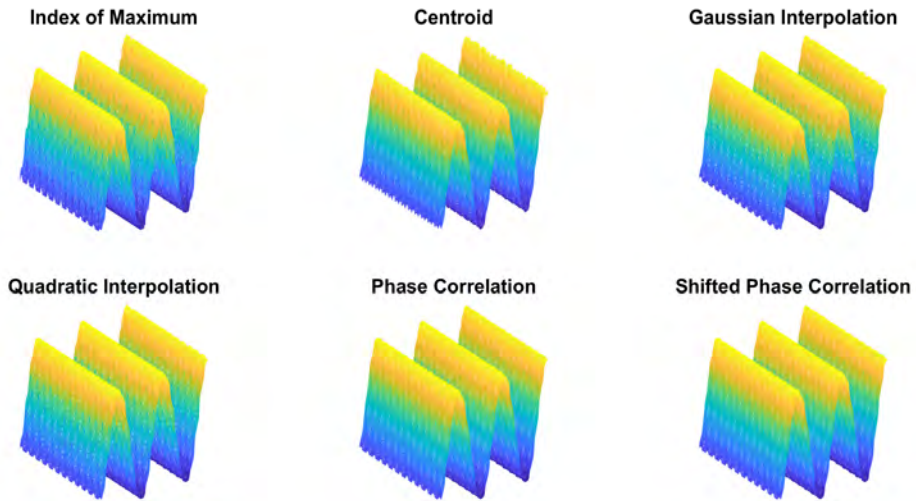


Figure 3.8: The recovered depth maps from synthetic data without noise. This data was processed with TENV with a 5-by-5 pixel window.

Even if the results hardly differ visually, the evaluation measures show the differences between the various methods (Figure 3.9). Considering the Root Mean Square Error (RMSE) of the no-noise synthetic data depth maps, one can easily see that the Gaussian fit (Gauss) and quadratic fit (Quadr) only perform a little better (0.2%) than the initial depth map (Argmax). Centroid finding (Cent), regular phase correlation (PC) and the shifted phase correlation (SPC) perform much better (about 40% compared to Argmax). The same trend can be seen in the correlation coefficient, where the PC and SPC methods perform best and the initial depth map performs the worst.

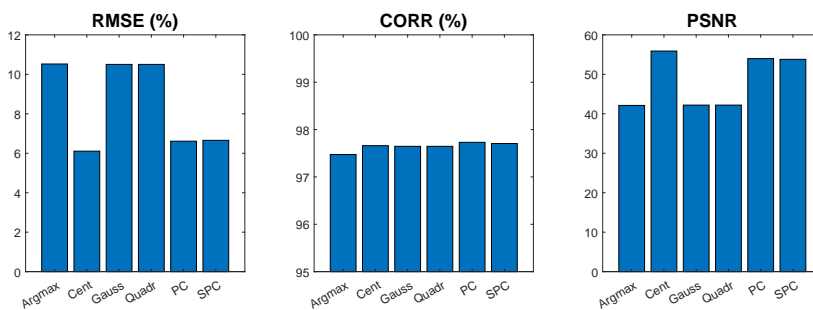


Figure 3.9: Evaluation of the depth maps from synthetic data (Figure 3.8) compared to the reference. The y-scale of the correlation coefficient plot ranges from 0.95 to 1 to magnify the differences between the methods.

3.5.2 Comparison using synthetic data with noise

Secondly, to test each method’s robustness to noise we added zero mean Gaussian white noise with a 0.005 variance to the synthetic focus stack before focus measuring and depth map generation. Adding white Gaussian noise to the source images of the focal stack adds high-frequency information to these images. FMOs are designed to extract high-frequency information from images since that is usually where the in-focus pixels are. Thus the added noise ripples through to the focus curves as well as the computed depth maps, shown in Figure 3.10. Differences between the depth maps now become more apparent, especially when compared to Figure 3.8. One element that can be seen in the depth maps in Figure 3.10 is the outliers, causing spikes. Especially in the first depth map generated by locating the index of the maximum. The depth map based on centroid detection has become very noisy as can be seen from Figure 3.11, that the quality of the depth map based on centroid finding has suffered the most from adding the noise. Centroid finding was one of the best-performing methods for clean data, yet performs even worse than the initial depth map for all evaluation measures. The possible cause for this behaviour is that the added noise non-symmetrically adds gravity to the points left and right of the peak in the focus curve, causing the centroid calculation to be severely offset. In some cases, squaring the signal y_d in Equation 3.8 can make centroid detection more robust to noise. We have tried this approach, yet did not notice any improvement in depth map quality.

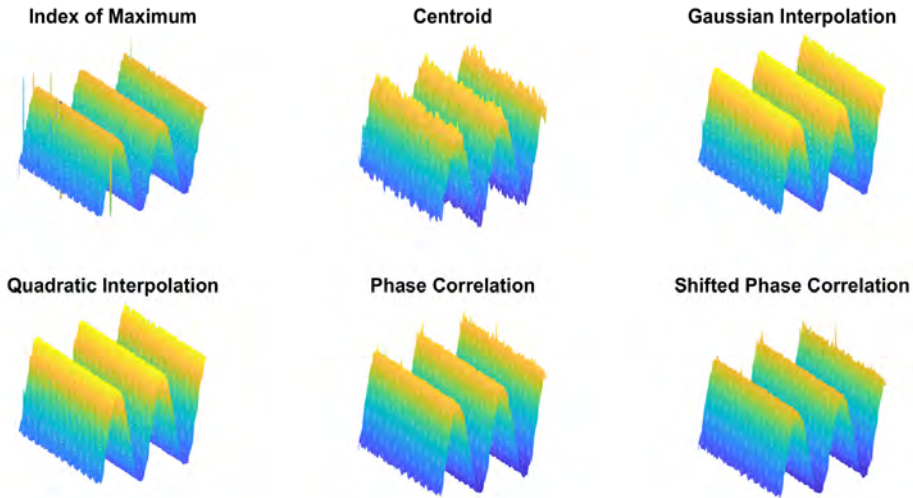


Figure 3.10: Depth maps generated from synthetic data using the compared methods with a 0.005 variance zero mean Gaussian white noise applied

All other methods behave very similarly to noisy data compared to clean data. Gaussian fit and quadratic fit perform slightly better than the initial depth map (0.3% for RSME), however, the phase correlation and shifted phase correlation outperform any of the other methods (almost 38% on RSME compared to Argmax). Additionally, it becomes clear that the shifted phase correlation produces the highest-quality depth maps. They are about 35% better compared to the initial depth map and about 5% better than regular

phase correlation. SPC also performs better than PC in terms of Root Mean Square Error (RSME) and Correlation Coefficient (CORR), although the difference there is less pronounced (0.3%).

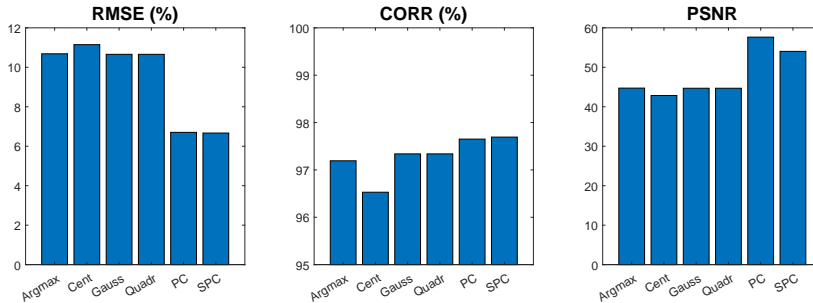


Figure 3.11: Evaluation of the depth maps from synthetic data with noise (Figure 3.10) compared to the reference (Figure 3.6). The y-scale of the correlation coefficient plot ranges from 0.95 to 1 to magnify the differences between the methods.

3.5.3 Comparison using real-world measurements

To validate the performance of our approach on real-world data, a single measurement of the tetrahedron in Figure 3.7a was compared to the averaged measurement that was created as described in Subsection 3.4.2. The same TENV focus measure operator with a 5×5 window was used for data reduction.

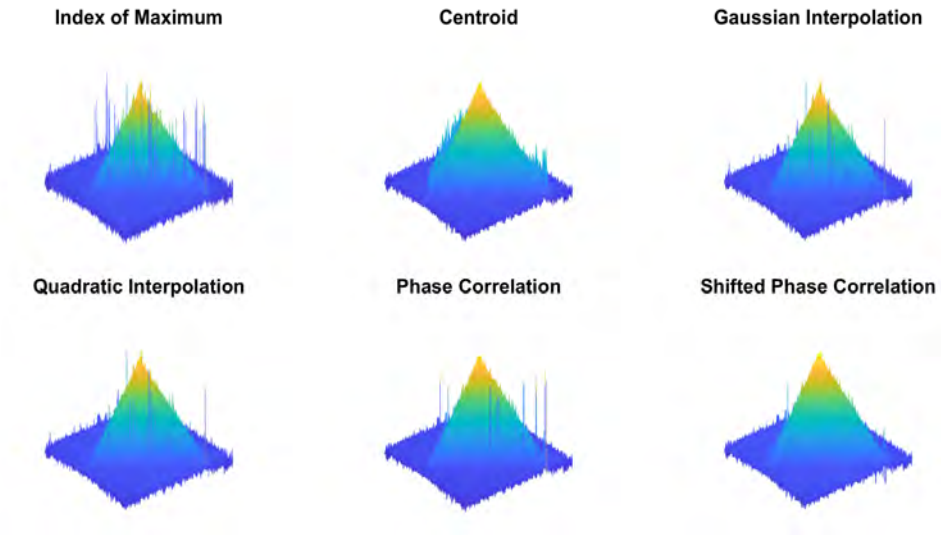


Figure 3.12: Depth maps from real-world measurements. This data (150 images) was processed with the TENV focus measure operator with a 5-by-5 pixel window.

The depth maps obtained from the real-world object, as presented in Figure 4, demon-

strate the effectiveness of our proposed method. The depth map produced using the index of the maximum focus value exhibits some noisy measurement points due to the inherent noise in the focus measure curves. In contrast, the depth map generated with centroid peak detection appears satisfactory at first glance, but it suffers from significant errors in the measurement along the edge between the tetrahedron and the flat part of the sample. On the other hand, the depth maps obtained through Gaussian and quadratic interpolation, as well as the map generated using standard phase correlation (PC), exhibit striking similarities and are noticeably less noisy than the first two maps. However, the depth map obtained with shifted phase correlation (SPC) stands out as it clearly contains the least amount of noise compared to the other depth maps. The evaluation metrics (Figure 3.13) prove what can be seen in the depth maps. For a real-world situation, the SPC method outperforms all other methods by 32% compared to the initial depth map or by 27% compared to standard methods like Gaussian-fit. The SPC depth map shows the highest correlation to the reference (99.81%). Contrary to the visual interpretation of the depth maps, the quality of the maps produced by both PC and SPC are very similar as can be seen by the PSNR measure, where the standard PC map looked more similar to the traditional methods like Gaussian and quadratic fit. Those methods perform almost 12% better than the index of the maximum method but not as well as the PC and SPC methods.

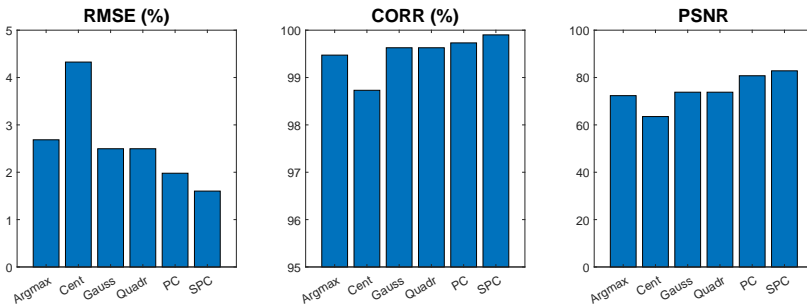


Figure 3.13: Evaluation measures of the depth maps of real-world measurements (Figure 3.12) compared to the reference (Figure 3.7b). The y-scale of the correlation coefficient plot ranges from 0.95 to 1 to magnify the differences between the methods.

Regarding the computational cost of each method, Table 3.1 provides the computation times for each method to process the synthetic data in Matlab 2021b on Windows 10 21H2. The PC that was used contains an AMD Ryzen 9 3900X CPU, an Nvidia GTX2080Ti GPU and 64GB DDR4 RAM. It is clear that the argmax method is by far the fastest method. However, it is certainly not the most precise method. The common methods, Gaussian fit and Quadratic fit are a bit slower compared to the argmax method. Both Gaussian and quadratic fitting require the maximum focus value plus two additional points on each focus curve to calculate the interpolation step. These additional steps are responsible for the additional computation time for these methods. Phase correlation and shifted phase correlation appear computationally more expensive. Although a fast Fourier transform is a highly optimised algorithm in Matlab, the calculation of it on this data is more complicated than the other methods. In the case of the shifted phase correlation method, 54 % of the computation time can be attributed solely to the circular shift, a part of the method that was not optimised during this research.

Table 3.1: Table with processing times for the compared methods when processing 60 images of 300 by 300 pixels

Method	Computation Time (s)
Argmax	0.0017
Centroid	0.0319
Gaussian Fit	0.0082
Quadratic Fit	0.0076
Phase Correlation	0.0259
Shifted Phase Correlation	0.0794

3.6 Conclusion

In this chapter, we introduced a new approach for the reduction of shape-from-focus (SFF) data to depth maps based on phase correlation. The main objective was to develop an easy-to-implement method with improved noise resistance and depth map quality compared to existing methods such as Gaussian or quadratic fitting and centroid finding. To validate the performance of the proposed method, depth maps were generated using the different methods and compared in terms of the deviation of the depth map to a common reference, depth map quality and robustness to noise. The comparative analysis was performed with synthetic data and measured data from a real object. The results of the experiments in this part show that the proposed phase correlation (PC) and shifted phase correlation (SPC) methods outperform the traditional methods in terms of measurement accuracy and robustness to noise. While the proposed method demonstrates improved performance, it does have a significant drawback in the form of increased complexity, particularly in the SPC method. Consequently, this results in a slightly higher computational cost. However, when considering the overall measurement time, including the image acquisition period, the computational overhead remains relatively low. Nevertheless, there is room for further research to optimise this method and potentially reduce the computational overhead even further.

Focus measure operator speed-up for shape-from-focus using GPU with PyTorch

In the previous chapter, we discussed an approach to optimise the processing of shape-from-focus data with the aim of providing lower noise and higher-quality depth maps with a limited increase in computational overhead. In this chapter, we will focus on improving the processing speed of from a focus volume to a depth map.

4.1 Introduction

Many image sensor applications like shape-from-focus (SFF) [75, 89] require accurate focus metrics. For example, focus metrics are also used for auto-focus [90, 91] purposes or for edge detection. This means estimating or calculating how well-focused an object point is in an image. As we have seen in Chapter 2, Section 2.2, the image of a point source, projected by a lens, is spread over a larger area when moved out-of-focus. Combining multiple spread-out object points in an out-of-focus image results in a blurrier image. If we look at it from a contrast perspective, an out-of-focus image has lower contrast than an in-focus image. The purpose of a focus measure operator is then to quantify the blurriness or lack thereof per image or per pixel in the case of SFF. An FMO uses a combination of image filters and other mathematical operations to quantify pixel sharpness [72, 92]. Focus measure operators are an active topic of research, as new FMOs are still being proposed [72, 70] as well as new methods using deep neural networks for focus measure [93, 94]. Figure 4.1 shows an example of the result of focus measuring an image with five bolts spread over a depth range. Of these five bolts, only the middle one is fully in focus. In the focus-measured image, one can clearly distinguish more light grey and white pixels, around the middle bolt. A lighter pixel is estimated to be more in focus than a darker pixel.

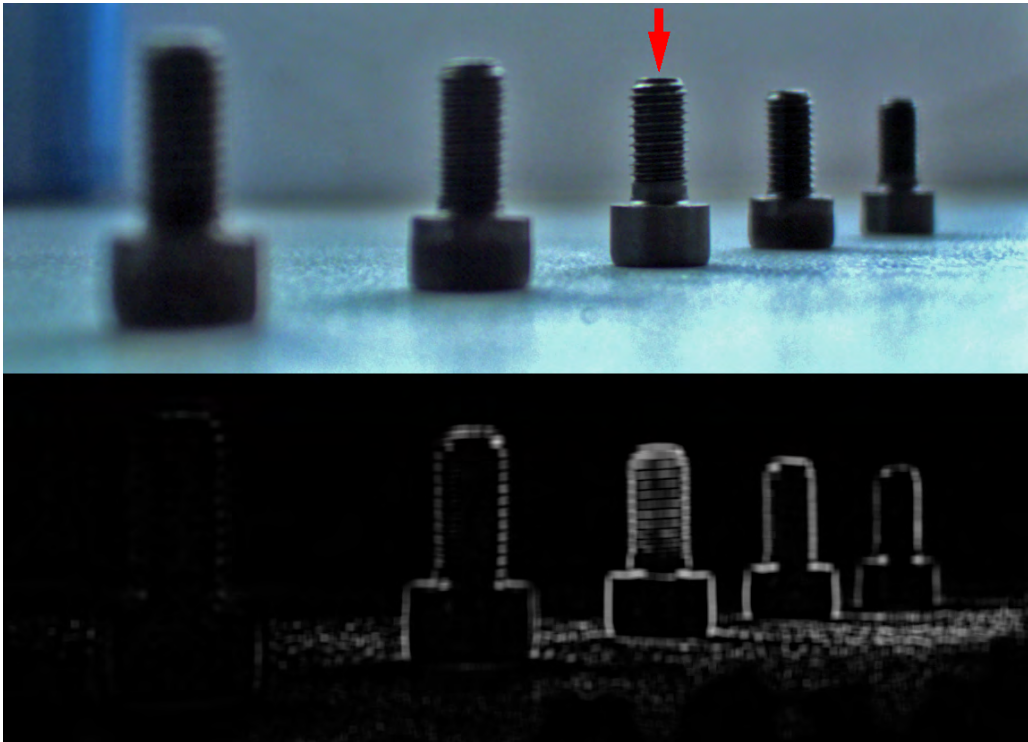


Figure 4.1: Example of the functionality provided by an FMO. The top image contains five bolts of which the middle one is most in focus (arrow). The application of an FMO (modified grey-level variance) gives the resulting bottom picture. This clearly shows that the middle bolt is in focus.

Focus measure operators are often described using their mathematical equation [43]. In practical terms, however, FMOs are implemented using different image processing filters such as averaging filters, median filters and standard deviation filters i.e... Many of the used image processing filters are implemented using a 2D convolution with a specific filter kernel. In 2D convolution filters, the filter kernel is applied to every pixel by means of a sliding window function Figure 4.2. The easiest implementation, albeit the least efficient is by using two nested for loops [95]. An FFT algorithm can already speed up the convolution operation for smaller kernels as explained in chapter 18 of *The Scientists and Engineers Guide to Digital Signal Processing* [96]. By converting the input to the frequency domain, the input image can be multiplied by the impulse response of the filter kernel. This corresponds to a convolution in the spatial domain and is much faster than the sliding window approach.

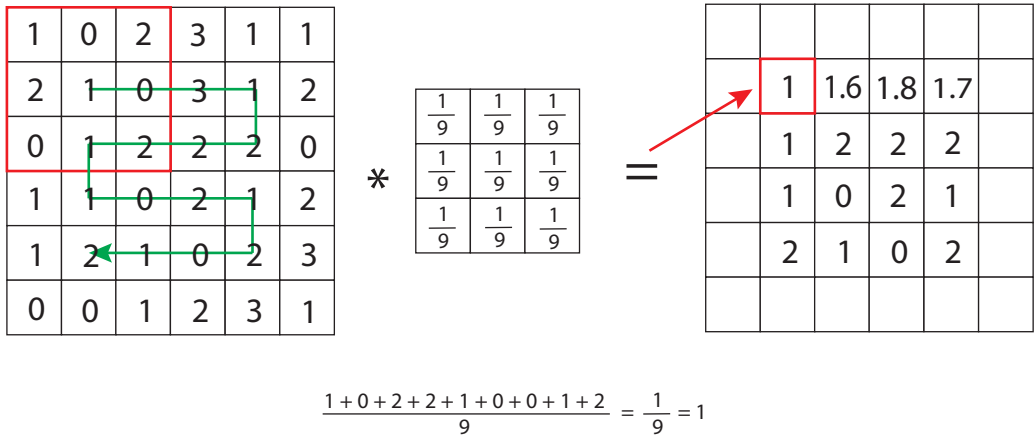


Figure 4.2: Example of an averaging filter as a convolution with a 3x3 kernel in image processing, implemented as a sliding window function. The green arrow shows the direction in which the kernel is evaluated across the image. All pixel values from the image are multiplied by the accompanying element in the kernel and then added to obtain the result.

Until recently, almost every image processing library available for Python implemented convolution filters to execute all computations on the central processing unit (CPU) of the computer. This is an acceptable method of computing when a single or even a few images need to be processed. However, when a large number of images are required to be processed using the same filter, a CPU needs a considerable amount of time to accomplish that task. When trying to optimise the measurement speed of an SFF setup, long processing times are detrimental. Modern computers typically contain two processing units CPU and GPU each dedicated to a specific set of tasks. CPUs typically consist of 1 to 12 very fast processing cores, that are highly optimised for fast sequential computing. A GPU, compared to a CPU contains hundreds to thousands of processing units. Even though the processing units of a GPU are slower, the combined processing power of the complete GPU is much higher compared to the CPU if the task at hand can be split up into smaller tasks and executed in parallel. The topic of CPU vs. GPU image processing and filtering is a well-studied research topic [97, 98, 99, 100]. It has generally been accepted that GPUs are better suited for these computations. This is especially advantageous for a task like image processing for shape-from-focus, where often 50+ images require simultaneous processing. Programming code to run on a GPU is very difficult. In this chapter, we will show how with the use of a modern neural networking library called PyTorch [101] it is relatively simple to implement FMOs to execute on GPU with a clear improvement in the processing speed for SFF data. PyTorch is a popular choice for GPU implementations of algorithms because it provides a user-friendly, dynamic computational graph, making it easier for novice developers to define and optimize deep learning models and other algorithms.

4.2 Implementation

Directly programming for the GPU is a complex task in itself. Therefore NVIDIA released CUDA [102], short for Compute Unified Device Architecture in 2007 as a software layer on top of the Physical GPU layer and the driver. CUDA allows for easy programming for the GPU in the C-programming language. So the user can more easily access the memory and multiple processing units. CUDA is specifically linked to NVIDIA, A generic equivalent to CUDA is OpenCL. It is generic in the sense that the same code is able to run on different GPU architectures albeit usually less efficient than a CUDA implementation.

While directly programming in CUDA is an option, it is still extremely complex to implement an optimised set of convolution filters among other things. Thus for this work, we have chosen to use a Python library called PyTorch. PyTorch is a relatively recent (released in 2016) development in the field of machine learning, generally used to implement deep neural networks. It provides an optimised implementation of the 2D convolution function. Since neural networks often use convolutional layers to apply filtering with weights and biases, learned in the training process, to either images or other feature maps. The library uses convolution algorithms written directly in C++ for optimization. PyTorch is also developed to efficiently run code on CPU or GPU with the CUDA extension. The library is written in such a way that it moves the data from CPU to GPU memory and uses the CUDA cores on an NVIDIA GPU to do the calculation. This way the exact same top-level code can be run on CPU or GPU. How the exact parallelisation step is executed by pyTorch is unknown. Two possibilities exist for the parallelization. All the focus measure operations over the specified kernel size could be parallelised or the focus measure convolution operation could be calculated for multiple images in parallel, or a combination of both. For this to be known an in depth analysis of the C++ implementations of pyTorch and CUDA should be carried out. For the implementation, we have used Python version 3.7 with Pytorch 1.9.0 and CUDA version 10.2. Apart from an implementation in PyTorch, we have also implemented the same focus measure operators using Numpy and OpenCV for comparison.

In this section, we will select two different focus measure operators to implement in Python with PyTorch. We will explain how they are implemented and discuss the main differences between the CPU and GPU implementations.

4.2.1 Selected focus measure operators

Two different focus measure operators are implemented in Python with CPU and GPU convolutional filters from a published Matlab source implementation[56]. The first FMO is Modified Grey-Level Variance (GLVM) and is a statistical operator that estimates pixel focus based on the variation in grey-level between neighbouring pixels. The second selected FMO is Tenengrad Variance (TENV). It measures the response to a horizontal and vertical Sobel mask. Thus, both TENV and GLVM have different mathematical approaches to measure pixel sharpness. These FMOs were selected in Subsection 2.3.2 based on their depth map quality and basic processing speed. There is a possibility that alternative FMOs may be more suitable for parallelisation. This aspect was not explored in the current research, presenting an opportunity for future investigation.

GLVM or modified grey-level variance

GLVM is a statistical approach to measure focus level. Mathematically it can be described as:

$$\varphi_{x,y} = \sum_{(i,j) \in \Omega(x,y)} (I(i,j) - \mu(i,j))^2$$

With I being the input image and $\mu(i,j)$ is the mean value of the neighbourhood $\Omega(x,y)$ around pixel (i,j) . One approach to grasp the working principle of this algorithm is to look at it from a frequency content point of view. An image contains both low and high-frequency information. Pixels in focus contain a lot of high-frequency information whereas pixels out of focus contain almost no high-frequency information. Applying a mean filter to an image results in a blurred version of the image ($\mu(i,j)$). This blurred version of the image can be thought of as only containing the low-frequency content of the image. Subtracting this blurred image from the original thus retains only the high-frequency information or a measure for all pixels in focus. When this process is executed on the CPU for all images in a focus volume, it is done sequentially. On the GPU this process is executed for all images simultaneously (Figure 4.3).

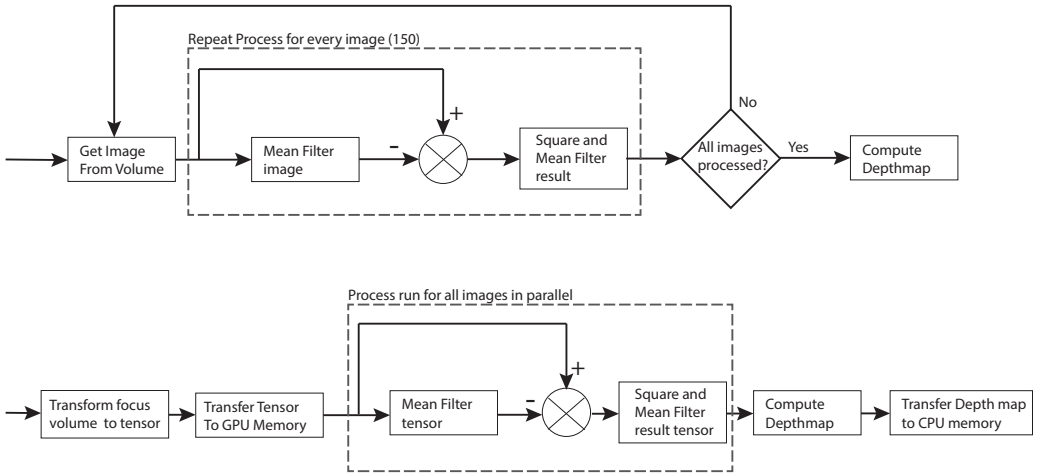


Figure 4.3: Implementation of the GLVM focus measure operator in CPU (top) and GPU (bottom). In CPU the FMO is executed a number of times depending on the number of images in the volume. In the GPU the process is executed at once, however, some overhead is created by moving the images from CPU to GPU memory

It can be seen from Figure 4.3, that a second mean filter is applied to the result of the variance calculation, which is not reflected by the GLVM equation. This mean filter is implemented in the Matlab source code [56], and was transferred to the python code. The result of the GLVM focus measure contains the high frequency information of the image as explained above. This not only includes the contrast rich in focus regions, but also the image noise. Applying the mean filter to the result, ensures that the focus measure is smoothed and the noise is filtered.

TENV or Tenengrad variance

The Tenengrad Variance FMO works in a different way compared to GLVM. Where GLVM is mainly a statistical approach to a focus measure, Tenengrad variance directly uses gradients to determine the focus measure. It uses the Sobel filter, a filter primarily used for edge detection [103]. It consists of a three-by-three isotropic filter kernel that is convoluted with the image [91]. Being isotropic, it delivers a different response in the x and y direction. The full FMO can be described mathematically as follows:

$$\varphi_{x,y} = \sum_{(i,j) \in \Omega(x,y)} (G(i,j) - \bar{G})^2$$

Where \bar{G} represents the average of the x and y response of the Sobel operator on the input image $G(i,j)$. it is calculated as $\bar{G} = \sqrt{G_x^2 + G_y^2}$. Basically, the gradients are extracted from the image in x and y directions and are squared and then added together to create an equal response of the filter in either direction. The result is then filtered using a standard deviation filter of a particular kernel size. When the standard deviation of the Sobel-filtered image is large, pixels are considered more in focus. The process flow for the implementation of this FMO is shown in Figure 4.4

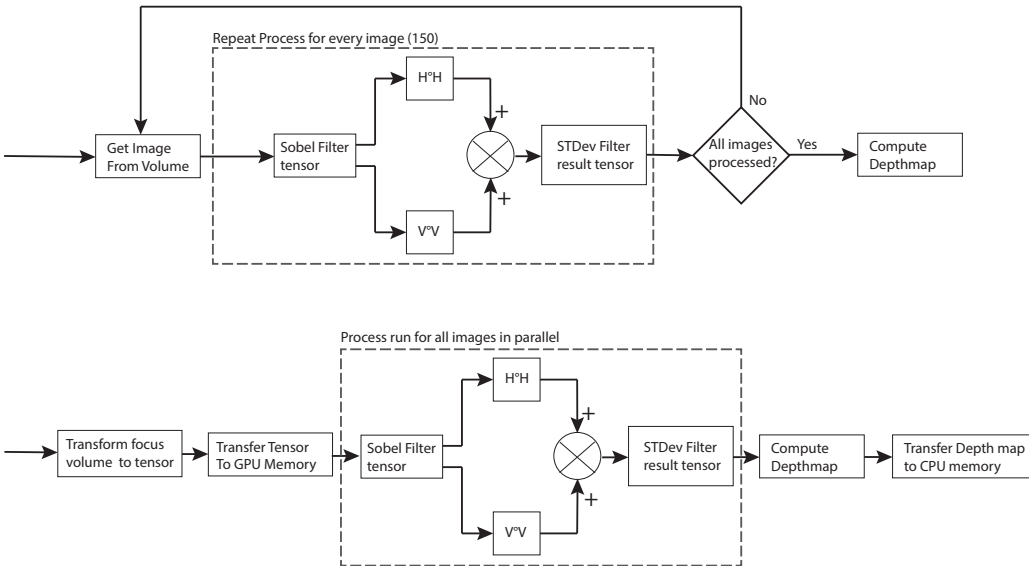


Figure 4.4: Implementation of the TENV focus measure operator in CPU (top) and GPU (bottom). In CPU the FMO is executed a number of times depending on the number of images in the volume. In GPU the process is executed once, however, some overhead is created by moving the images from CPU to GPU memory

4.3 Experimental setup

In order to validate the effectiveness of the proposed implementation of these focus measure operators with PyTorch, an experiment was conducted. A series of tests were run on a custom build PC with an AMD Ryzen 9 x3900 CPU with 64GB of DDR4 RAM, an Nvidia RTX2080ti GPU with 11GB of GDDR5 video RAM and a 1TB PCIe v3.0 NVME SSD.

The first test we conducted was a comparison of processing speed vs. the kernel size of the FMO. Typical kernel sizes for SFF vary between 7x7 and 15x15. We have run the test for kernel sizes between 7x7 and 101x101. Kernel sizes larger than 31 are impractical and hardly ever used, but give more insight into the limits of using a GPU/PyTorch for focus measure operations. Secondly, we have tested the speed improvement over different amounts of images ranging from 10 to 300. Where the typical SFF measurement uses in the range of 50 to 200 images, we have tested outside that range to validate whether the transfer of images from CPU to GPU memory impacts the performance. For all measurements, we have carried out a type A uncertainty analysis by averaging 5 measurements and calculating the standard deviation

4.4 Results and discussion

The tables and graphs in this section represent the results of the measurements described above. Table 4.1 lists the average processing times for different kernel sizes for the six implementations of the focus measure operators, two implementations with NumPy and OpenCV, two with Pytorch on CPU and two with PyTorch on GPU. The standard deviation of these measurements is given in Table 4.2

	7x7	9x9	15x15	31x31	51x51	101x101
GLVM CPU Numpy/OpenCV	8,145	9,065	9,067	9,106	11,719	13,616
TENV CPU Numpy/OpenCV	16,811	17,777	17,756	17,785	20,343	22,795
GLVM CPU PyTorch	5,492	5,626	7,694	18,488	42,159	151,671
TENV CPU PyTorch	8,712	8,886	10,910	21,726	45,216	154,711
GLVM GPU PyTorch	1,298	1,356	1,835	4,282	9,818	36,017
TENV GPU PyTorch	1,247	1,312	1,514	2,724	5,418	36,082

Table 4.1: Average processing times in seconds for a batch of 150 images with the implemented algorithms in function of the kernel size.

	7x7	9x9	15x15	31x31	51x51	101x101
GLVM CPU Numpy/OpenCV	0,022	0,035	0,036	0,039	0,057	0,051
TENV CPU Numpy/OpenCV	0,040	0,033	0,035	0,046	0,014	0,066
GLVM CPU PyTorch	0,172	0,195	0,160	0,084	0,131	0,207
TENV CPU PyToch	0,200	0,125	0,114	0,100	0,119	0,168
GLVM GPU PyTorch	0,012	0,030	0,044	0,021	0,046	0,345
TENV GPU PyTorch	0,033	0,027	0,021	0,043	0,038	0,334

Table 4.2: Standard deviation on processing times for the measurements of Table 4.1

What is clear from Table 4.1, is that the average processing times for the Numpy/OpenCV implementation are much longer compared to the PyTorch implementations, except for impractically large kernel sizes. Therefore we have focussed on the PyTorch implementations for the remainder of this experiment. Table 4.3 records the average processing times for the different PyTorch implementations compared to the number of images in a focus volume, with the Standard deviations of these measurements reported in Table 4.4

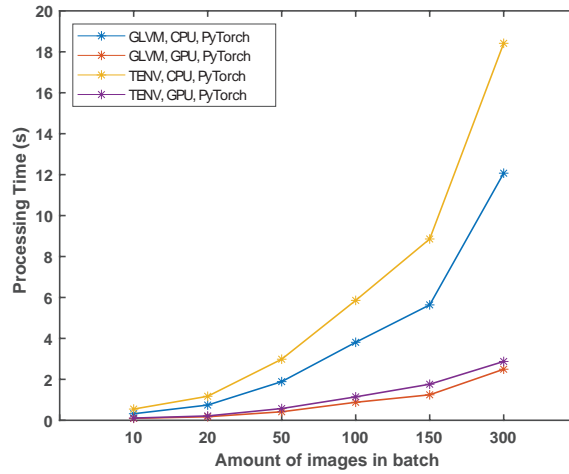
	10	20	50	100	150	300
GLVM CPU PyTorch	0,319	0,744	1,888	3,810	5,637	12,071
TENV CPU PyToch	0,548	1,173	2,984	5,857	8,857	18,415
GLVM GPU PyTorch	0,095	0,173	0,416	0,879	1,245	2,494
TENV GPU PyTorch	0,108	0,213	0,574	1,145	1,762	2,874

Table 4.3: Average processing times in seconds for the implemented algorithms with a 9x9 kernel size in function of the amount of images processed simultaneously

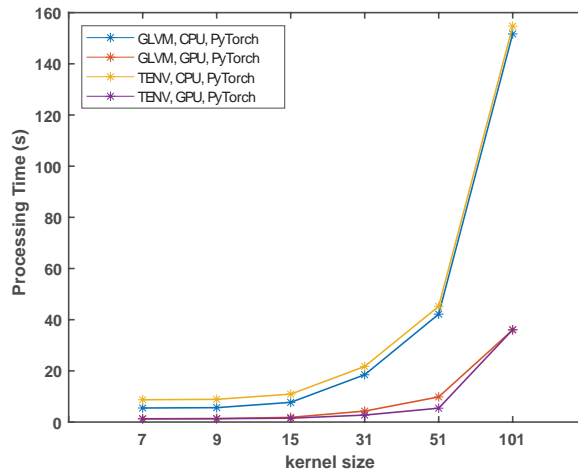
	10	20	50	100	150	300
GLVM CPU PyTorch	0,032	0,044	0,042	0,100	0,132	0,131
TENV CPU PyToch	0,055	0,032	0,026	0,067	0,202	0,125
GLVM GPU PyTorch	0,016	0,008	0,039	0,133	0,037	0,099
TENV GPU PyTorch	0,005	0,007	0,014	0,020	0,023	0,104

Table 4.4: Standard error on processing times for the measurements of Table 4.3

From these measurements, we can infer that enabling the GPU with PyTorch proves to be very beneficial for FMOs when used for shape-from-focus. As explained in [18], a typical shape-from-focus measurement uses approximately 150 images (1280 by 1024 pixels) to be processed with a kernel size of 9 or 11. With these parameters, the CPU processing method for GLVM in PyTorch, on average, takes about 5.64 seconds (Table 4.1). With GPU processing this is reduced to about 1.245 seconds, which reflects a speed increase of 4.44 times. For TENV the CPU method in PyTorch takes about 8.86 seconds whilst with the GPU this only takes 1.76 seconds, a reduction of 5 times. The average improvement in processing speed is about 4 times depending on the FMO, kernel size and amount of images in a batch.



(a)



(b)

Figure 4.5: Processing time comparison between CPU and GPU implementations for GLVM and TENV Focus Measure Operators in Python vs. the number of images processed (a) and the kernel size (b)

The graph in Figure 4.5a shows the processing time vs. the amount of images. It clearly shows that for very small amounts of images, the processing times for both CPU and GPU methods are almost equally fast, with all execution times below 1 second. So for autofocus purposes, running the FMO on a GPU might cause too much overhead. For larger amounts of images, as in the case of SFF, the benefit of processing on GPU becomes larger as the GPU methods all stay below 3 seconds of execution time even at 300 images. One thing to note here is that the processing of 300 images in parallel on the GPU requires a significant amount of video memory. Processing 300 images with the Tenengrad Variance FMO required almost the full 11GB of GDDR5 video memory

available in the RTX2080Ti. This can be optimised by using other data types than the standard float32 for PyTorch tensors but is currently not supported by the conv2d function in PyTorch version 1.9.0. Using lower precision data types would also improve the GPU processing speed as well as reduce transfer time to move the data from CPU to GPU memory.

The graph in Figure 4.5b shows the processing time vs. the kernel size. The number of images processed is 150. The graph shows a similar trend towards bigger kernel sizes. For relatively small kernel sizes of 7 by 7 to 15 by 15, there is almost no increase in processing time. With larger kernels, from 31 by 31 and larger, the processing time increases exponentially and becomes impractical. Interestingly the implementations using Numpy and OpenCV were slower than their PyTorch counterparts for smaller kernels, 7 by 7 to 15 by 15, but from 31 by 31 to 101 by 101 proved to be much faster (Figure 4.6). This leads to the conclusion that the convolution implementation in libraries like Numpy and OpenCV suffer from more code overhead

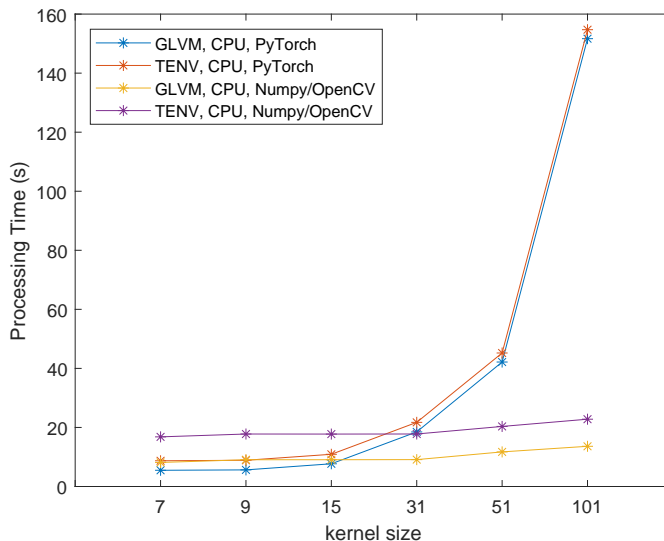


Figure 4.6: comparison between two different CPU implementations of the tested FMOs. One implementation is a combination of Numpy and OpenCV functions, the other is the exact same implementation in PyTorch as the GPU implementations except was run on CPU.

Adding a high-performance GPU to a system brings additional cost. Since GPUs are now a common element in systems, the added cost is relatively low. As described above, the vast amount of memory used when datasets become extremely large can be a concern. But with every release of graphics cards the amount of video memory is increasing and using other data types in processing can reduce the memory usage. Although the speed-up in processing is limited to only 3.5 to 6 times, in absolute terms this speed-up can potentially enable some new technologies. Because the processing of large high-resolution datasets can be done in almost one second. This makes near real-time 3D reconstruction using shape-from-focus possible.

4.5 Conclusion

We have implemented two different FMOs in Python using PyTorch and tested their performance on CPU and GPU. The top-level code was written in such a way that the exact same code could be run on both types of processors. We conclude that using Deep Learning Libraries like PyTorch provide efficient methods to convert existing FMOs used for shape-from-focus to processing on GPU. Processing on the CPU is sufficient for autofocus purposes. With a processing time reduction of 3.5 to 4.5 times GPU processing of shape recovery through shape-from-focus allows for near real-time 3D imaging, if combined with a measurement system capable of capturing the required amount of images in a similar time frame. This implementation is most likely not the most optimised solution for this problem, but due to the ease of programming a very fast method for already some gain in processing time. This work could potentially be optimized by using a camera connected to a frame grabber card which feeds directly into CPU memory. While the current setup first takes the information into CPU memory and requires a transfer to GPU memory. This direct interface to GPU is thus an item to consider for future research.

Combining shape-from-focus with laser triangulation

The previous chapters of this dissertation discussed novel methodologies to improve the quality and speed of shape-from-focus processing. The following two chapters will discuss adaptations to the shape-from-focus capturing process to make it more suitable for integration in the additive manufacturing process.

The scientific contribution described in this chapter was published in: *Gladines, J.; Sels, S.; Blom, J.; Vanlanduit, S. A Fast Shape-from-Focus-Based Surface Topography Measurement Method. Sensors* **2021**, *21*, 2574. <https://doi.org/10.3390/s21082574>

5.1 Introduction

As discussed in Chapter 1, the incorporation of additive manufacturing into the conventional production process necessitates accurate metrology for the manufactured parts. Numerous methods are available for determining the shape of an unidentified object, although most of these techniques are primarily designed for inspecting and measuring finished parts. To enhance the quality of additive manufactured products, there is a growing interest in adapting these shape recovery techniques for application in in-line or even online metrology.

It has been established that the ability of shape-from-focus (SFF) to capture fine details makes it an ideal candidate for precision online metrology for additive manufacturing. However, as discussed in Chapter 2, due to the high number of images (approximately 50-200) and the large amount of processing required to create a depth map, the technique can be considered time-consuming. The total measurement speed can be improved in multiple ways. As discussed in Chapter 4, many of the existing focus measure operators are ideal candidates for optimization through processing on GPU. Algorithms based on image filtering using convolutions can be greatly sped up through parallel processing on GPU [100, 98]. A second possibility to improve measurement speed would be to reduce the number of required images to produce a depth map. By limiting the measurement range to a smaller area around the target depth, the amount of images to capture can be reduced. With fewer images to capture and process, the measurement time can be

reduced. In the case of AM, the CAD file, of the part to be printed, can be used to determine the target depth. In case shape to measure is not known, a rough estimate of the part dimensions must first be determined. In this chapter, we discuss a two-step approach of first using a fast 3D profiling technique like laser triangulation (LT) as shown in Figure 5.3 to provide coarse depth information to limit the required amount of images for SFF. The solution we propose can improve the measurement time independent of the hardware used. The following sections will first present the proposed method followed

by a description of the setup created for testing this method. Subsequently, we will elaborate on the two-step measurement principle and the experiment to evaluate the proposed method. Lastly, the measurement results will be presented and discussed in the results and conclusion.

5.2 Proposed Method

Building on the findings presented in Chapter 2, SFF can deliver precise measurements, yet requires high magnification objectives to reach μm accuracy and precision. The use of high magnification objectives typically results in a small field of view (FOV) of the camera. The consequence of the small FOV is that the measurement of a larger area requires multiple sub-measurements to be combined or stitched. Another consequence of a small FOV is that for these sub-measurements the measurement equipment is most of the time not used over its full depth measurement range. This implies that we can limit the measurement range of the SFF to the range required for each sub-measurement.

We can explore this concept from the perspective of a single pixel in a focus volume. The evaluation of pixel focus from a specific pixel within a focus volume results in a Gaussian-like curve (Figure 3.1a). An ideal Gaussian distribution, as represented in Figure 5.1a, simulates such a focus curve. The objective of Shape-from-Focus (SFF) is to identify the maximum point of this focus curve. By analysing Figure 5.1a, it becomes evident that areas where the focus value is lower than e.g. 0.7 do not contain substantially useful information for determining the peak. This assumption is supported by the fact that Gaussian interpolation, as explained in Chapter 3, Section 3.2, employs only three points: the noisy maximum response and one point on each side of that maximum. Hence, it can be inferred that points outside the useful range do not require capturing or processing. In short, we can potentially reduce the measurement time by thresholding the capturing of images around the pixel's maximum focus point Figure 5.1b if the range of depth values in the FOV of the camera is smaller than the depth range of the SFF setup.

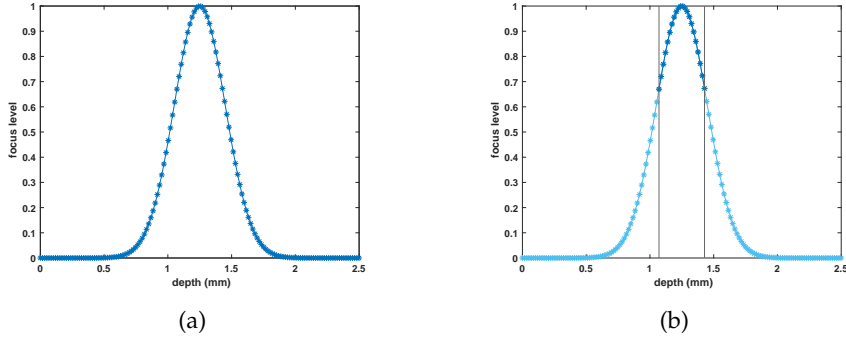


Figure 5.1: (a) Simulation of a normalised pixel focus curve by a Gaussian distribution. Every point represents a captured image in a theoretical focus volume. (b) Thresholded profile, with sufficient points to determine pixel depth.

5.2.1 Measurement system setup

For the method we are proposing, we have built a specific SFF setup containing an electronically tunable lens (ETL) [88] in combination with a 2x finite conjugate microscope objective from which a 50 mm extension tube could be removed to create a 1x objective and a 1.3 MPixel (1280 by 1024 pixels), C-mount camera (Allied Vision U-130B). This combination results in a FOV of 4.27 mm by 5.35 mm or an optical magnification of 1.15x. This means that each $4.8 \mu\text{m}$ pixel of the camera sensor represents $4.17 \mu\text{m}$ on the object.

The combination of the ETL with this microscope objective allows variation of the focus distance over a range of 2.5 mm. The driver of the lens allows to change the focal length of the lens over a maximum of 4143 steps. Dividing 2.5 mm by 4143 results in a theoretical step height for SFF of 600 nm. As demonstrated in Chapter 2, the accuracy of an SFF measurement does not significantly improve above 200 steps. For this method, we opted to divide the focus tuning range into 150 steps, for an approximate step size of $17 \mu\text{m}$ as a good compromise between height resolution and measurement speed.

In order to create depth maps of larger areas the target needs to be translated under the SFF camera system. We therefore used a pair of Zaber X-LSQ300B translation stages mounted orthogonally for XY-translation of the target. So to obtain a depth image of the full target multiple depth images have to be stitched together with some overlap for blending (Figure 5.2). Image stitching was performed based on the absolute translations made by the translation stages and not by feature detection and transformation.

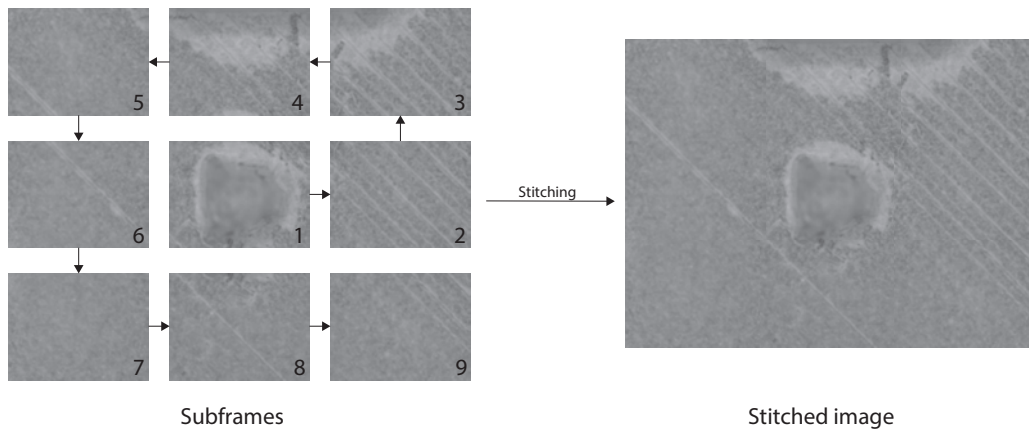


Figure 5.2: Principle of image stitching as implemented for this research. Subframes (left) are taken counterclockwise with an overlap of 150 pixels and then stitched together to create an image of a larger area (right).

For unknown objects, it is impossible to predetermine the thresholded measurement range with the SFF system alone. Another topography method capable of creating depth maps much faster but also coarser can be used to get a rough estimate of the object's profile. The lower accuracy of the coarse depth map can then be translated to a margin around the estimated depth range to reduce the possibility of incorrect measurements. Thus, in order to utilise this method effectively, it is necessary to obtain approximate height information of the object before conducting measurements with shape-from-focus (SFF). There are various options available to acquire this preliminary height information. In our case, we have chosen to employ Laser Triangulation (LT), also known as Sheet of Light (SoL) or laser ranging sensors [104], although, alternative methods such as structured light profilometry or other rapid profilometry techniques would also be suitable for this purpose.

Our setup was built similar to Figure 5.3 around a PhotonPhocus MV1-D2048-3D04 3D camera with a 12 mm lens, a line laser and a zaber X-LSQ300B translation stage for the third dimension. The camera was placed at a 15° angle to the laser line. This custom laser triangulation setup can thus be optimized for this purpose. Yet any change to the setup of the LT sensor requires a series of intricate calibrations to be performed to extract meaningful measurements. Any mistake in calibration will result in less optimal results for this part of the method. An of the shelf triangulation sensor that is chosen to suit the specific needs of the setup will allow to work with finer margins using the proposed method.

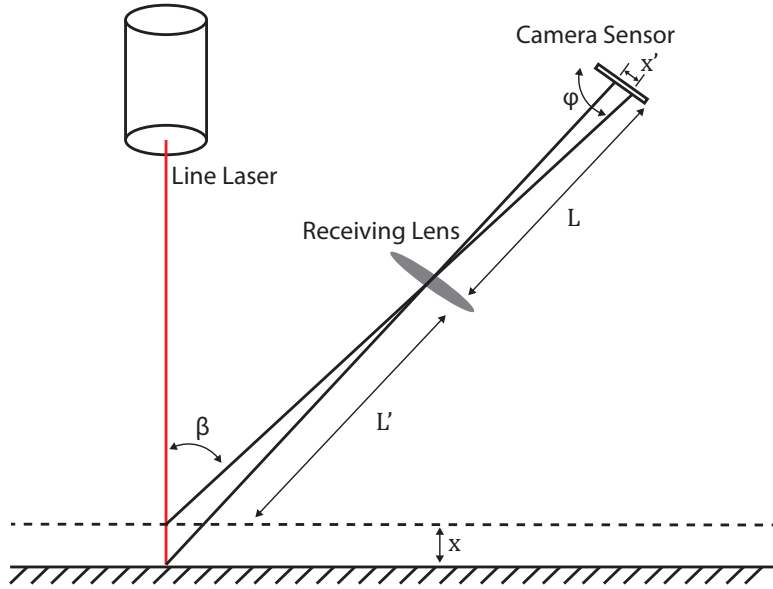


Figure 5.3: The principle of laser triangulation, where the position of a reflected laser line on a camera sensor is a function of the profile height. Based on an image from Sun B. and Li B. [12].

With L and L' being the lens to object and lens to sensor distance, ϕ being the angle between the lens and the camera sensor which is 90° for our setup, β being the angle between the camera and the laser line. x and x' are the physical change in object height and its corresponding change of the laser spot on the sensor. The trigonometric relationship between x and x' is determined by [12]

$$x = \frac{Lx' \sin(\phi)}{L' \sin(\beta) - x' \sin(\phi + \beta)} \quad (5.1)$$

If we take x' equal to the camera sensor's pixel size of $5.5 \mu\text{m}$ we can calculate the theoretical depth resolution of our setup. For us this results in a theoretical limiting depth resolution of $20 \mu\text{m}$ for the LT setup. The real depth resolution is much worse as it is also influenced by laser scattering, optical aberrations and precision of calibration. The actual depth resolution was about $50 \mu\text{m}$. The lateral resolution of the LT setup is defined by the camera resolution, the FOV of 50° and the step size of the translation stage. For our setup, we estimate the lateral resolution at $100 \mu\text{m}$. A drawback of using laser triangulation to provide a coarse depth map is occultations. Because the camera is at an angle to the laser beam, occultations of the laser reflections on the target occur. The greater the angle the bigger these occultations. So height resolution of the LT system is always a trade-off with the occultations that will cause some areas to have no data. Although, this can be resolved by placing multiple cameras. This is beyond the scope of this work, so it was not included in this research.

5.2.2 Two-step shape-from-focus

The complete measurement system is thus composed of two individual measurement systems. One LT system for coarse measurements and one SFF system for precision measurements. The translation stages are common to both systems (Figure 5.4). As SFF requires optics with a small FOV and small depth of field (DOF) and Laser triangulation requires optics with a large FOV and a large DOF it is not possible to combine the measurement systems using one camera and shared optics. Therefore it was required to also calibrate both the SFF and LT system in terms of their extrinsic location.

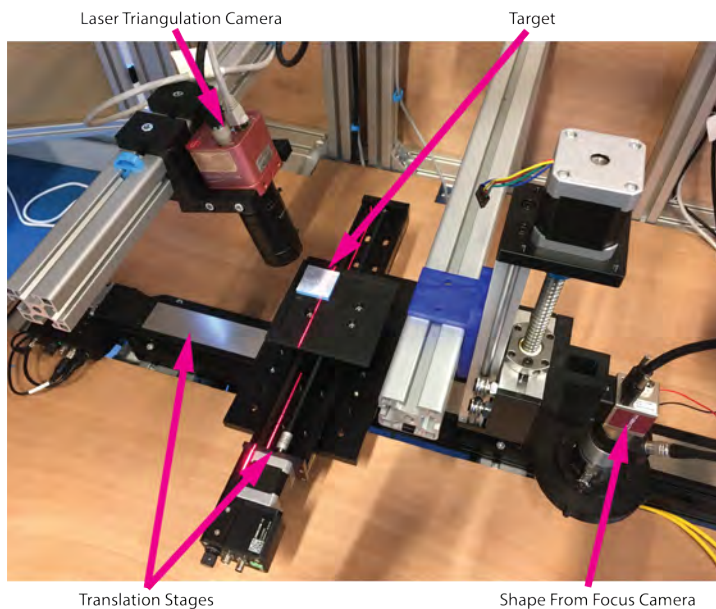


Figure 5.4: Image of the measurement setup with two 3D measurement systems and with the target on a sample plate mounted on top of two translation stages for xy-movement of the target.

The measurement principle, depicted in Figure 5.5, is characterised by its simplicity. The LT system initially scans the target, generating a coarse point cloud. This point cloud is subsequently transformed into a depth map and scaled to match the resolution of the final SFF depth map. The LT depth map is then cropped and transformed to match the final FOV of the complete target. Now the current small field of view of the SFF camera can be extracted from the coarse depth map. Next, the information from the extraction of the coarse depth map is used to determine the minimum and maximum depth boundaries for the SFF scan. With the conventional SFF method, the creation of a subframe would take 150 images measured over a range of 2.5 mm. With this two-step approach, this measurement range is thus reduced to e.g. 1 mm. So instead of 150 images, only 59 images need to be captured and processed.

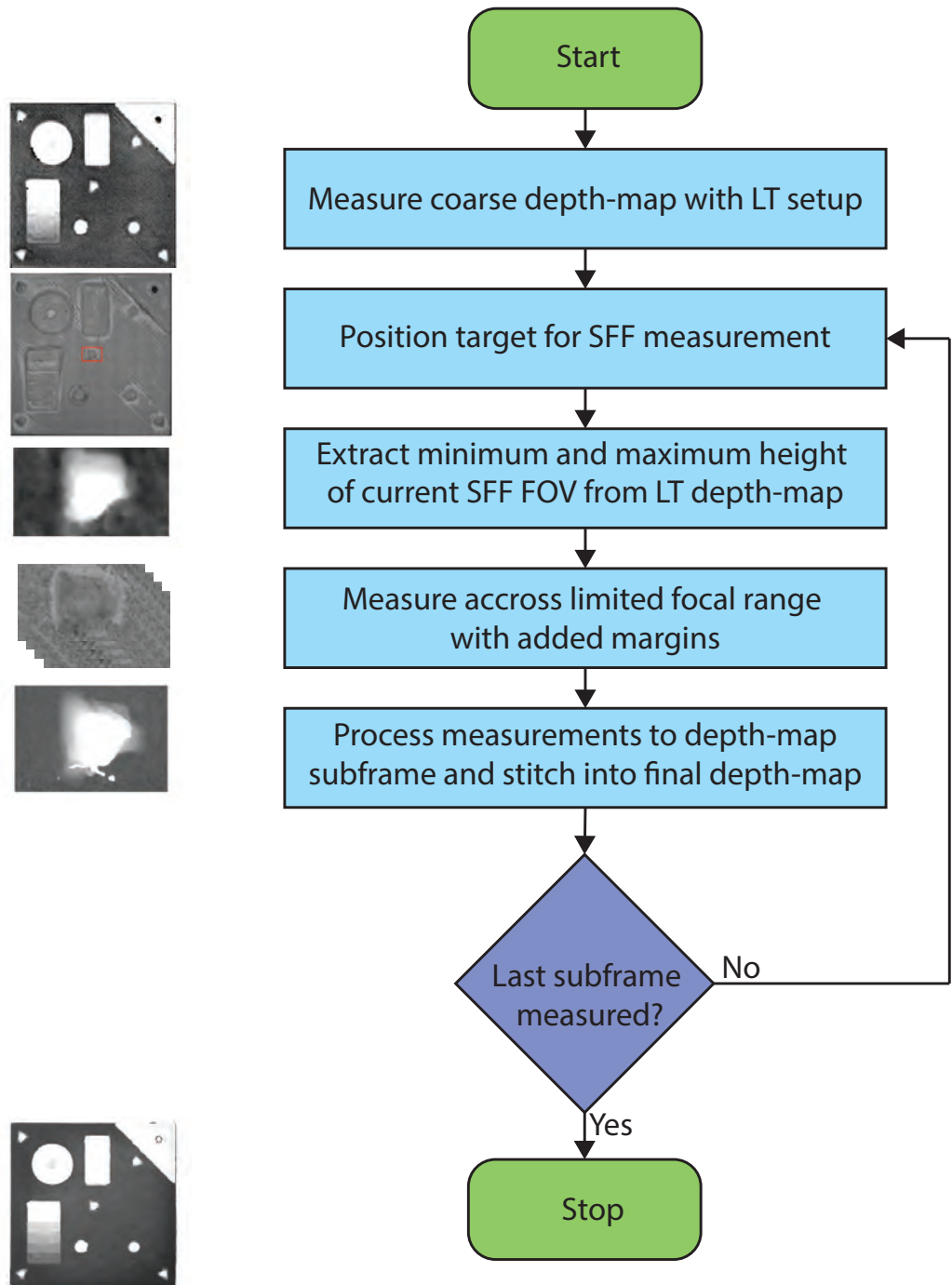


Figure 5.5: Flowchart of the measurement principle of combining LT and SFF techniques to speed up stitched SFF measurements

Once the section is scanned using SFF with the limited depth range, the reduced data set is processed with the same focus measure algorithm. Subsequently, the translation stages move the target allowing another section of it to become visible to the SFF system. The process then recommences from selecting the current FOV section on the coarse depth map generated by the LT system.

5.2.3 Experimental setup

To validate the proposed method, an experimental test was conducted, comparing it to the traditional shape-from-focus method in terms of measurement speed and quality. The evaluation was performed using a plastic 3D printed target, measuring 40 by 40 mm, as the reference (Figure 5.6). The target was printed in Colorfabb NGEN and was coated in Ardrex 9D1B spray to aid the measurement process

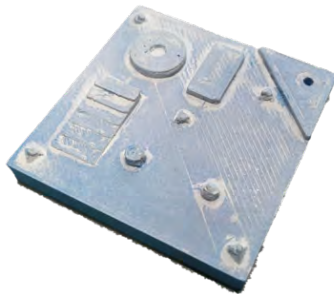


Figure 5.6: 3D printed measurement target of 40 mm by 40 mm with rectangular, spherical and cylindrical features. This target was printed using a conventional fused filament 3D printer in NGEN and coated with Ardrex 9D1B spray to aid the measurement process.

This target was first measured as a reference using a Keyence VK-X1000 confocal laser scanning microscope in focus variation mode with a 5x objective. The target was subsequently measured using the traditional SFF method as well as with the proposed method on the setup described above. To create the depth maps from the captured images, we have used the Modified Gray Level Variance (GLVM) implementation in Matlab by Pertuz, S. et al. [56]. The measurement quality of both the traditional shape-from-focus (SFF) method and the proposed method was compared to the reference measurement by analysing their respective depth maps. Additionally, the speed of image capture and processing, as well as the total measurement time, were recorded for both methods to facilitate a comprehensive speed comparison. In the following section, we present the results of the experiment and provide a detailed discussion of the outcomes.

5.3 Results and discussion

Table 5.1 shows the imaging, processing and total measurement time for the SFF system with and without prior depth knowledge. It is obvious that the addition of a coarse depth map to reduce the measurement range of the SFF system has a benefit on both capturing and processing. Where the normal SFF process would require the capture and processing of 25,350 images, applying this principle reduced the image capture to 14,411. An excellent reduction of a little over 43%. Since the average number of images for a section of the depth map is 85 instead of 150, the processing time is also reduced from 844 seconds to 436 seconds, which is a reduction of about 48%. The reduction in processing time should be similar to the reduction in the amount of images since the processing time scales linearly with the number of images (Figure 5.7).

At an average frame rate of 50 frames per second (fps), the capture of 25,350 frames required a total capturing time of 507 seconds using the conventional SFF method. Consequently, the reduction of 43% in image capture results in a 288-second capture time for the proposed measuring method. The total measurement time for the conventional SFF was 1350 seconds, whereas the two-step approach reduced it to 724 seconds. This reduction in measurement time corresponds to a significant improvement of 46% on the SFF system. When considering the measurement time and pre-processing of the laser triangulation measurement, an additional 45 seconds need to be accounted for in the two-step approach. However, even with this inclusion, the total measurement time is still significantly reduced from 1,350 seconds to 769 seconds. This reduction amounts to a remarkable 43% decrease compared to the traditional method.

	n	t_c (s)	t_p (s)	t_m (s)
Regular SFF	25350	507	844	1350
Two-step SFF	14411	288	436	724

n is the total amount of images captured.

t_c is the imaging time.

t_p is the processing time on CPU.

t_m is the total measurement time.

Table 5.1: Measurement and processing times for Conventional SFF and the proposed two-step SFF method. The processing method used was GLVM, implemented in Matlab R2019b [56] and run on a AMD Ryzen 3900x CPU.

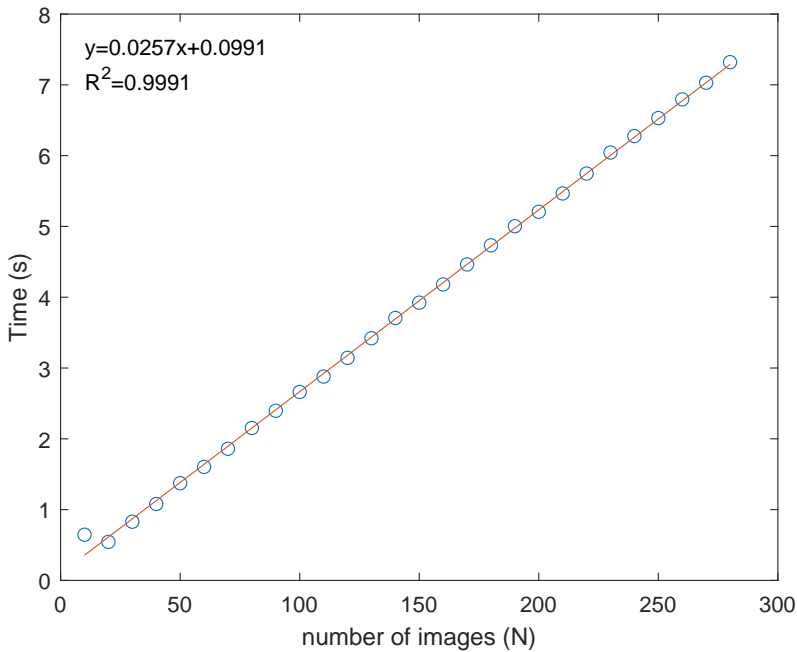


Figure 5.7: Processing time for a shape-from-focus dataset (1280x1024 pixels) reduction to depth map using the GLVM focus measure operator, implemented in Matlab R2020, as a function of the number of images (N).

To ensure that the reduction in measurement time does not compromise measurement accuracy, reference measurements were conducted using a Keyence VK-X1000 in focus variation mode. The reference measurements have an accuracy of approximately 500nm and took about 3 hours to complete due to the much higher resolution of the Keyence VK-X1000. The measurements of our system were then compared with these reference measurements using the software CloudCompare[105]. For the comparison, the depth maps were converted to point clouds. The respective point clouds were cropped to all show the same FOV of the target. After a coarse manual alignment of the point clouds, the alignment was optimised using Iterative Closest Points (ICP)[106]. After alignment, the point-to-point distance of a measurement to the reference was taken and a mean and standard deviation to the reference were calculated. This process is shown in Figure 5.8. The measurements were averaged over 5 individual measurements with a random offset applied to the starting position of the measurement to rule out any lucky measurements. For comparison, the same process was also applied to the point cloud from the LT system. Figure 5.9 shows the final depth maps created by the different measurement systems converted to point clouds in CloudCompare.

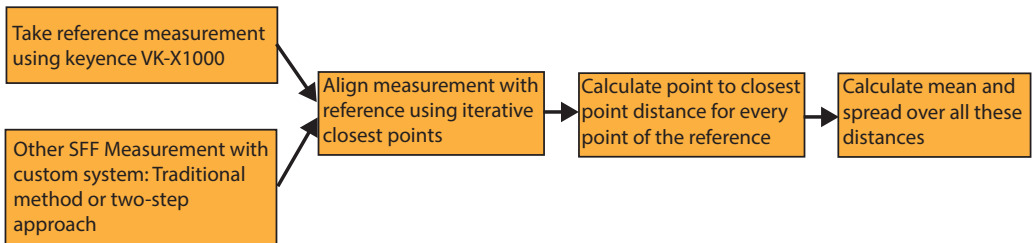


Figure 5.8: Visual representation of the comparison process, to assess the differences between measurements of our custom system with the reference measurements from the Keyence VK-X1000 using CloudCompare.

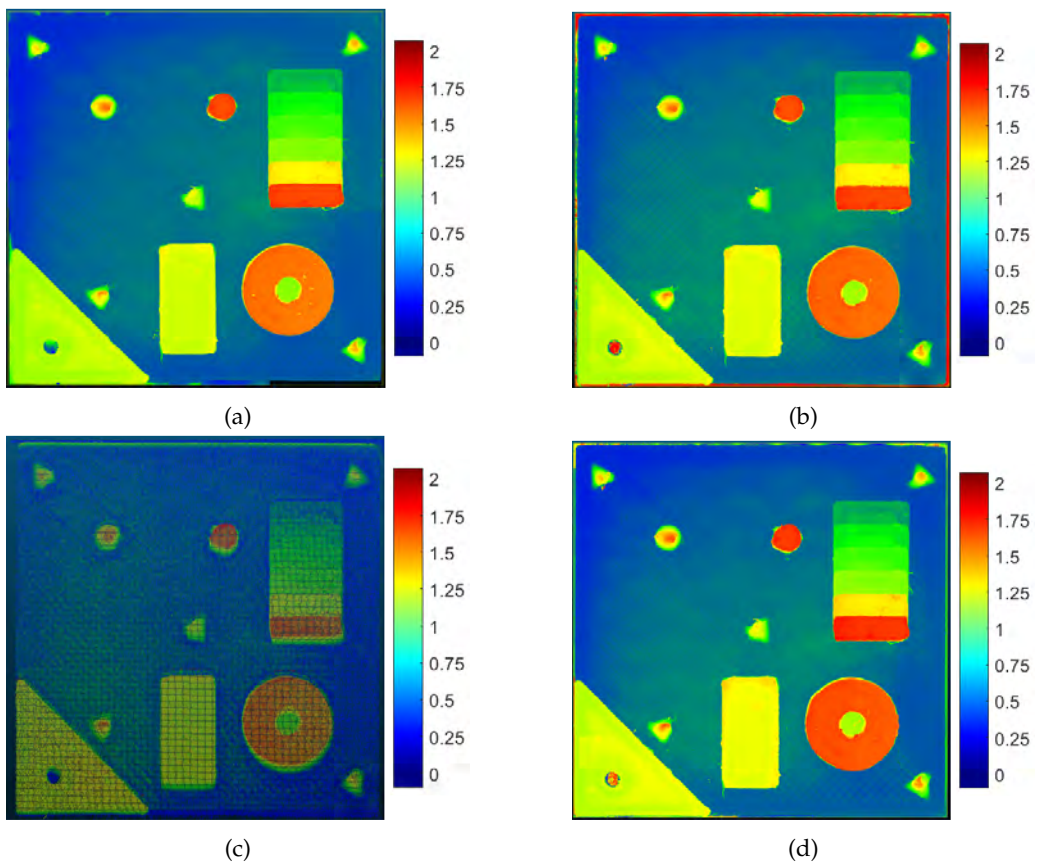


Figure 5.9: Point clouds generated from the depth-maps of the different measurements using CloudCompare (a) Keyence VK-X1000 reference, (b) Shape-from-focus without thresholding, (c) Laser Triangulation, (d) Shape-from-focus with thresholding from LT information. The LT measurement (c) is darker because it contains fewer measurement points compared to the other measurements.

	μ (mm)	σ (mm)
Regular SFF	0.3×10^{-3}	0.033
Two-step SFF	0.1×10^{-3}	0.026
LT	2.0×10^{-3}	0.120

μ is the mean of the difference to the reference.

σ is the standard deviation of the difference to the reference.

Table 5.2: Measurement result of the comparison of the different measurements (standard SFF, two-stage SFF and LT) with the reference, measured with Keyence VHX-1000.

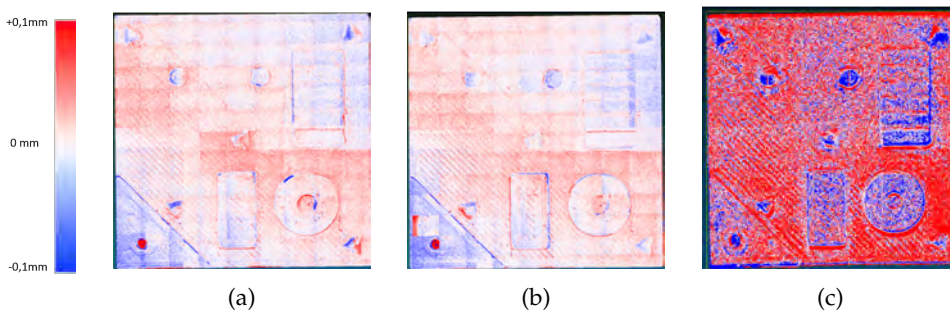


Figure 5.10: Comparison by subtracting the reference measurement of the different measurements to show the deviations in red and blue. (a) conventional SFF method, (b) the proposed two-step approach and (c) the laser triangulation measurement(c). The deviations from the reference are similar for (a) and (b), while (c) shows larger deviations and also some systematic error.

From Figure 5.10 and the data in Table 5.2 it is clear that the application of the novel method had no negative influence on the accuracy of the SFF scan. The mean deviation from the reference of 0.3×10^{-3} mm and 0.1×10^{-3} mm has the same order of magnitude for both measurements. The same conclusion can be made for the standard deviation of the measurements, with 0.033 mm and 0.026 mm. The minor difference of 7 μ m in standard deviation is negligible compared to the standard deviation of the laser triangulation measurement. However, the accuracy of the results must also be treated with caution. The standard deviation is relatively large compared to the mean of the comparison. A potential cause could be an issue with the measurement precision. Alternatively it could be caused by outliers in the data. A more detailed analysis is required to find the root cause. Figure 5.10 also shows some systematic error on the LT measurement. The lower area's are consistently estimated to high (red) where the higher area's are mostly estimated to low(blue). This could potentially be caused by the use of a custom LT system that requires manual calibration. A commercial calibrated system should not have the same issue. Since the LT image is only used as a rough estimate of the shape, this systematic error is not critical to the functioning of the proposed method. However, it does influence the margins that can be taken on the limits of the focus volume to be captured and thus by extension on the potential gain of the method.

The gain in measurement time with this proposed two-step approach is dependent on two important parameters. Firstly due to the lower accuracy of the coarse measurement, a margin must be applied to the boundaries set to limit the capturing range. For example, if the coarse measurement has a depth resolution of $50\ \mu\text{m}$ the margin should ideally be at least $50\ \mu\text{m}$ above and $50\ \mu\text{m}$ below. If we apply this to the example given above the actual measurement range is 1.1 mm instead of 1 mm. So with the margin applied the total amount of images to be captured is 66 for 1 mm. A larger margin leads to less gain in measurement time.

The second important parameter is the ratio between the measurement range of the SFF system and the amount of sub images of the full target that need to be measured across the full range. If a relatively flat object is measured, the gain in measurement time will be large because most of the subframes of the depth map will require a limited set of images to be created. If a very rough object is measured that requires every subframe to be measured across the entire measurement range, then there is no gain in measurement time.

The proposed two-step approach combines the benefits of the precision method with the speed of any other method. Additionally developing the coarse method like LT to have a similar resolution as the SFF system would usually require an equally small FOV and therefore an increase in measurement time. The addition of extra components to a measurement setup also requires extra investment. However, the additional cost of the extra components is estimated to be small compared to the total measurement cost of measuring for prolonged periods of time. The cost of the Laser triangulation system is in the order of magnitude of 10000 Euro. Whereas the measurement cost of running this equipment is estimated to be at minimum 100 Euro per hour. After already 200 hours of measurement time the extra investment cost would already be earned back. Adding a second measurement system for improvement of the original system, can in certain situations be a limitation. E.g. for mobile applications, adding the second measurement system introduces a lot of extra complexity. This method was specifically developed to be used for in-line or online metrology purposes, where the added complexity is not an issue.

5.4 Conclusion

We have introduced a two-step approach to improve the measurement speed of shape-from-focus (SFF). We have shown that by applying coarse depth information to SFF, the measurement time for stitched measurements can be reduced by limiting the measurement ranges of the individual sub-frames. This approach has led to an overall improvement in measurement time of 43% on a test target. It has been shown that the proposed method does not impact the accuracy of the measurement. However, from an accuracy perspective, the standard deviation of the comparison to the reference measurements was rather large. This could be the result of outliers or a measurement precision problem on the instrument. Therefore, it could also be interesting to also calculate the standard deviation between repeated measurements, for example to get an indication of the measurement noise. The method is independent of the hardware used. The total time reduction is however dependent on multiple parameters. First of all the added margin to the limits set by the coarse measurement. The applied margin is limited by the accu-

racy of the fast 3D profilometry technique. Using a more accurate system for the coarse measurements allows the use of narrower margins and therefore a bigger reduction in measurement time. Secondly, the measurement time reduction is dependent on the ratio between the field of view of the SFF system and the height ranges of the target within this field of view. If the target has height variations over the full SFF range in every section to be imaged, the total reduction in measurement time can be zero. However, the field of view and measurement range of the SFF system could also be adapted or optimised for specific parts to provide the maximum reduction. Lastly, due to the lower resolution of the laser triangulation scan some objects of the target might go undetected. So those features will not be included while determining the measurement range for the SFF scan which might result in errors. As introduced earlier, when the shape to be measured is already known, it is possible to bypass the use of a rapid profilometry method (such as LT in this context) for measurement. In instances like Additive Manufacturing (AM), the rough depth map can be derived from the known shape, where the CAD file, for example, can serve as the source of the rough depth map. In case of in-line inspection for AM, the part would usually be measured at regular intervals. In that case, the previous measurement could also be used to provide the rough depth map as input to the two stage approach.

A possible improvement for this method would be to use the measurement from the LT system as an initial value on a point basis when improving the accuracy by Gaussian fitting on the measurement points. The LT measurement could also be used to determine the validity of the depth estimation by SFF. Using high-speed cameras and a different way of controlling the ETL can also lead to additional gains in measurement time.

A continuous motion shape-from-focus based profilometry method

Traditional precision shape-from-focus on large surfaces requires images to be captured while the measurement object is stationary. This does not coincide with the continuous motion nature of additive manufacturing based on fused filament fabrication or laser metal deposition. This chapter examines a possible adaptation to state-of-the-art shape-from-focus to overcome this issue.

The scientific contribution described in this chapter was published in: *Gladines, J.; Sels, S.; Hillen, M.; Vanlanduit, S. A Continuous Motion Shape-from-Focus Method for Geometry Measurement during 3D Printing. Sensors* **2022**, *22*, 9805. <https://doi.org/10.3390/s22249805>

6.1 Introduction

Additive manufacturing (AM) is a constantly developing production method, with a lot of effort going into zero-defect manufacturing [107]. Nowadays, most 3D additive manufacturing machines, also known as 3D printers, are mainly open-loop systems [108, 109, 110]. This can result in the scrapping of parts due to defects that only become apparent when the printing process is complete and the part is thoroughly inspected. Early detection of defects or abnormalities could save material and parts. For accurate inspection and defect detection, a precise 3D scanning method is required. Recently, some studies have closed the printing loop by employing state-of-the-art 3D reproduction methods, such as laser triangulation [24, 22, 23] or fringe projection [10, 11, 25]. Shape-from-focus (SFF) [75, 43], also known as focus variation microscopy (FV), is a method that is, as discussed in Chapter 2, also capable of measuring at μm level accuracy and precision [40, 111]. It has an advantage over laser triangulation and fringe projection, in that it can also deliver an all-in-focus texture map of the surface, making it easy to detect surface defects. It can also accurately measure surface roughness [40]. SFF has already been presented as an on-machine solution for accurate surface topography measurements by Santoso T. et al. [7]. This traditional shape-from-focus method is still being researched [112, 94] and it has already successfully been applied to additive manufactured parts in offline quality inspections [18]. However, state-of-the-art SFF implementations cannot be applied for online measurements in conventional AM machines. An SFF measurement requires tens

of images to be captured with the 3D-printed part at the same position relative to the camera/lens to produce a depth map. Precision measurements of larger surfaces using SFF thus require the stitching of multiple discrete measurements, while the nature of AM is to print in one continuous motion.

In this chapter, a method is proposed that adapts the current SFF technique into a scanning method. This would allow for larger areas to be measured to the same accuracy and precision during printing (Figure 6.1). By moving the camera or sample during a repeated scan across the focus range of the SFF setup, essentially the same data as with a discrete measurement can be collected. However, the data is organised differently: images will be shifted and the information can be split across multiple images. Through the use of image stitching and aligning methods, the gathered data can be re-arranged for processing with current SFF methods. The problem presented in this chapter has already been solved for white light interferometry [113], albeit in a different manner. In the work of A. Olzak et. al. the optical axis of the camera is tilted, so the object points at different heights intersect the maximum coherence plane at different times. The same approach could potentially also be implemented for SFF, where object points at different height would intersect with the stationary focal plane at different times. This would eliminate the need to control the focus distance and thus eliminate the tunable lens from the measurement system. Tilting the camera would increase the risk of occlusions. The rest of this chapter outlines the employed measurement setup and its operational control, the processing methods that were applied and the validation of the proposed method.

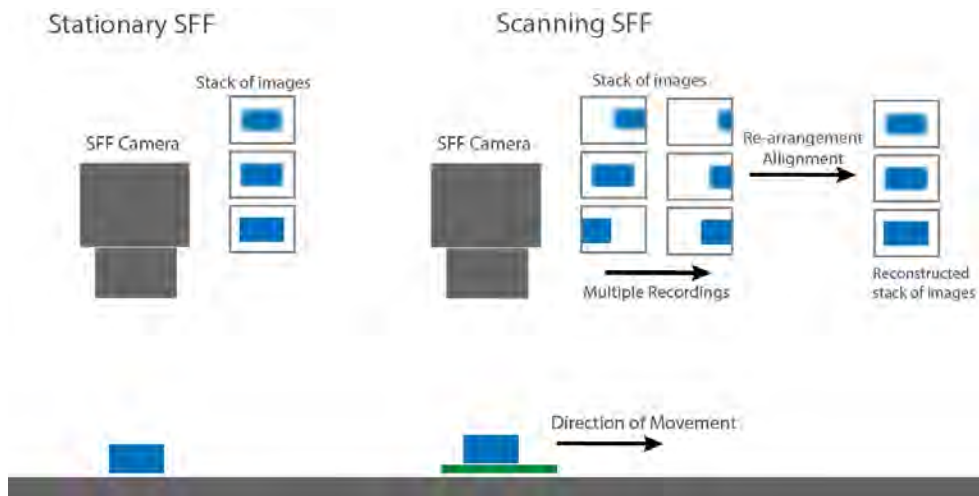


Figure 6.1: The concept of scanning SFF (right), where the sample or camera is translated during the measurement, compared to the traditionally stationary SFF. (left)

6.2 Design of the setup and experiment

With current direct energy deposition (DED) additive manufacturing machines printing at lateral resolutions below 50 μm , to do in-line inspection, one would need a system capable of measuring with a precision of 25 μm or below. The typical scanning speeds for DED systems are in the range of 5 mm/s to 20 mm/s [114]. Thus for online inspection, one would need a metrology system capable of measuring in that speed range. The following sections describe the measurement setup that was built for this purpose and the development of the proposed scanning SFF method.

6.2.1 Measurement system setup

The measurement setup is presented in Figure 6.2. It allows for precise depth profile measurements using shape-from-focus. The setup consists of three main parts: the camera (1.3MP Mako U-130B Mono) with electronically tunable lens (Optotune EL-10-30C [88]) and finite conjugate objective lens (Mitutoyo 3x Objective CF), a translation stage (Zaber X-LSQ300B) and a signal generator or DAC (NI USB-6343DAQ). The camera with a tunable lens and objective lens provides a 9 mm by 11 mm field of view (FOV) with a narrow depth of field for use with shape-from-focus. The focus can be controlled over a range of 10 mm. The combination of optics and camera results in a pixel scale of 8.5 μm per pixel and an optical resolution of approximately 25 μm . The translation stage allows for larger areas to be measured. In an ideal situation, the translation stage provides a stable platform moving at a constant speed. However, in our case, the translation stage introduced some periodic wobble in x and y direction between the different images in the focus volume. This makes aligning the images more difficult and could potentially cause some degradation in the resulting depth map. In the current form of this method, we have ignored this effect, yet, resolving this problem could improve the method. The signal generator provides a trigger signal to the camera as well as an analogue signal to control the tunable lens. The lighting consists of a ring light and an additional LED light to provide some oblique illumination. Adding oblique illumination provides extra contrast on the 3D-printed surface for the FMO to work. The tunable lens allows for varying the focus distance in order to create a stack of 1024-by-1280-pixel images at different and equally spaced focus distances.

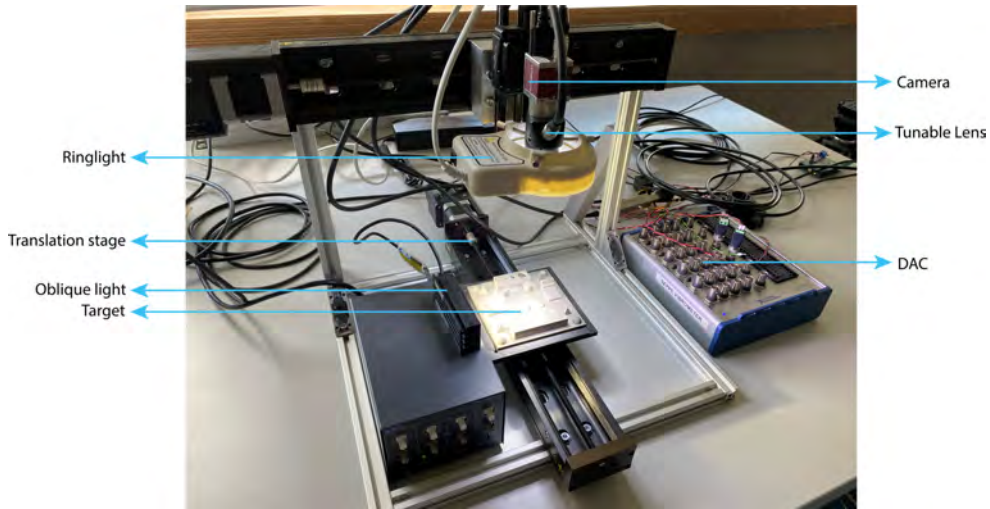


Figure 6.2: Measurement setup: The object is placed on a translation stage and is illuminated by two lights, the object is recorded by a camera with a tunable lens and microscope objective while moving.

As explained in Chapter 5 and Section 6.1, in the traditional sense of the shape-from-focus, when imaging a larger field of view, the camera is placed at different discrete positions and the individual measurements are stitched together. In the proposed method the camera or sample will be constantly moving as it would during additive manufacturing. Measuring with the shape-from-focus at speeds of, e.g., 15 mm/s and above requires a fast control of the focus distance. Traditional shape-from-focus uses a precision translation stage to change the focus distance. However, these precision translation stages usually have a maximum speed of about 2–3 mm/s [115]. The proposed method would require translation speeds over 30 mm/s. As an alternative, an electronically focus tunable lens (ETL) can be used. The EL-10-30C we have selected for this research can be controlled with frequencies of 50 Hz and above, which, with a focus range of 10 mm, corresponds to 500 mm/s in our setup. To use the lens at these speeds, the traditional way of controlling the lens through the driver with serial commands is too slow. The lens driver must be controlled using an analogue signal. For SFF to function properly, the exact focus distance must be known for every captured image. Therefore, the camera must also be hardware-triggered using a trigger signal that is synchronised with the lens control signal. Both signals are supplied by the signal generator.

The controller of the tunable lens accepts an analogue signal between 0 and 5 V to control the current to the lens over a range of 292 mA. This analogue signal is sampled at 10-bit, thus allowing for a maximum of 1024 different steps in the current control range of the lens. Ideally, one would control the lens with a sawtooth signal and trigger the camera with a square wave signal. However, this would require perfect synchronisation between the lens signal and the actual trigger of the camera. Since the delay between the trigger signal applied to the camera and the actual capturing of the image is unknown, one cannot trust it to be constant. Therefore, we chose to control the lens with a staircase signal with the number of steps being equal to the number of images required in a focus stack. The camera is then triggered by the falling edges of a square-wave signal. The

falling edges are centred onto the steps of the staircase signal to the lens driver. Both signals are presented in Figure 6.3.

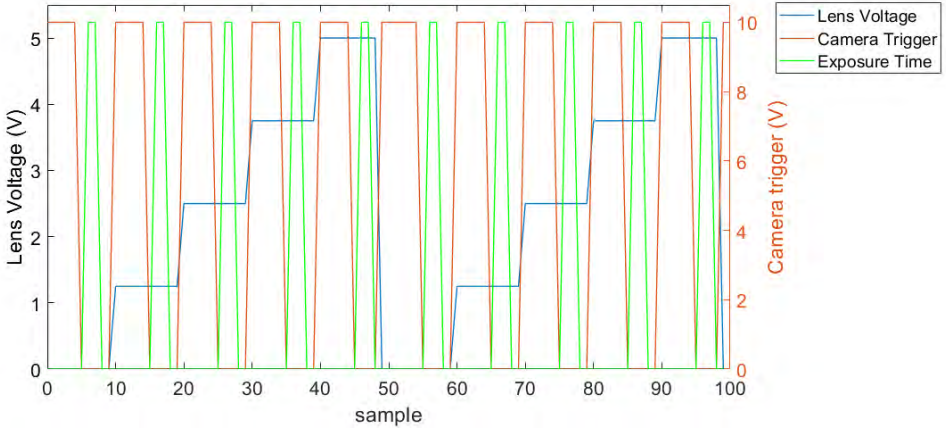


Figure 6.3: An example of a trigger signal to the camera (right axis, orange) on top of the analogue staircase signal to the tunable lens (left axis, blue). The camera is triggered on the falling slope, which in itself is in the centre of the voltage step of the tunable lens. This example would twice capture 5 frames at 5 different focus distances.

The frequencies of the staircase signal and the trigger signal depend on the translation speed of the camera or sample. The maximum translation speed in mm/s is defined by a few parameters: The FOV of the measurement system, the frame rate of the camera, the number of frames in a focus volume and the amount of overlap between consecutive volumes. For the proposed method to work effectively, it is necessary for a portion of captured images to overlap, allowing for the stitching of successive depth maps (Figure 6.5). In the time it takes the camera to create the number of images for one depth map calculation, the camera translation may not exceed more than 50% of the width or height of the camera FOV, depending on the direction of movement. The limit to the amount of the translation l for consecutive focus volumes is given by Equation (6.1), where w is the width or height of the FOV.

$$l \leq \frac{w}{2} \quad (6.1)$$

For example, in an imaging system with an FOV of 9 mm by 11 mm, the theoretical maximum amount of translation between focus volumes is 5.5 mm if translating in the direction width of the FOV and 4.5 mm if translating in the direction of the height of the FOV. This theoretical maximum translation distance of 50% is practically unusable for stitching measurements since this results in no overlap between the images of consecutive focus volumes. Thus, a portion of these images must overlap. The amount of translation l with respect to the amount of overlap is given by Equation (6.2). Where P is the percentage of overlap and w is the width or height of the camera FOV.

$$l = \frac{w - (w \cdot P)}{2} \quad (6.2)$$

If the maximum frame rate of the camera r and the number of images required in a focus stack N is known, one can calculate the maximum translation speed s for a measurement using Equation (6.3):

$$s = \left(\frac{r}{N}\right) \cdot l \quad (6.3)$$

From these equations, one may notice that a larger FOV with the same camera allows for faster translation speeds while measuring at a lower optical resolution. The measurement speed can also be increased by employing a higher imaging frame rate or by reducing the number of images required in a focal stack. The number of images that are required can be reduced by using various interpolation methods [75, 76, 77]. An example is given for the maximum translation speed with our setup:

A camera with an FOV width of 11 mm and a frame rate of 150 fps can capture 50 frames in 0.333.. seconds, resulting in a theoretical measurement speed of 15 mm/s, given a 9.1% overlap between focus stacks. Doubling the frame rate of the camera to 300 fps or reducing the number of required images in a stack to 25 allows the system to measure at 30 mm/s.

Figure 6.3 also shows the exposure time of the camera (green). It is important to mention that the exposure time of the camera must be short enough to avoid object points to move on the sensor during the exposure. The maximum exposure time is easily calculated from the pixel scale (8.5 μm) and the translation speed. Dividing the pixel scale in mm by the translation speed in mm/s defines the maximum exposure time. This results in a maximum exposure time of 573 μs for measuring at a speed of 15mm/s on our system. The next step in the measurement method is the processing of the images to a depth map, which is described in the following section.

6.2.2 Image processing

Traditionally, with the shape-from-focus technique, the stack of differently focused images are all captured with the object and camera at a fixed relative position; thus, no image alignment is required. In this chapter, we consider the case where the part moves relative to the camera during the SFF measurement process. This means that the recorded images in the SFF measurement process are shifted relative to each other. This required the images to be properly registered and aligned before the focus measure operator (FMO) could be applied to build the depth map.

The alignment is based on the integer pixel shift calculated from the translation speed. For example, if one is measuring while the object is moving at 15 mm/s with a stack of 50 images captured in 0.333 seconds, each image is shifted by approximately 0.1 mm with respect to the previous image, which translates to 11.64 pixels. As a result, the total image shift from top to bottom is 4.995 mm or 582 pixels. To align the images, the amount of shift in pixels for each image is thus calculated back from the speed of the translation and that shift is then inversely applied to the image (Figure 6.4).

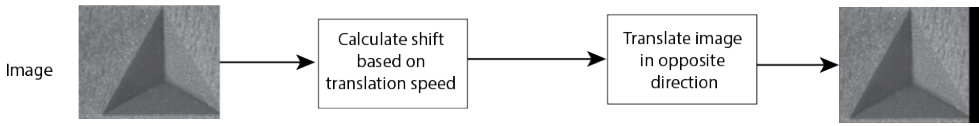


Figure 6.4: Alignment process of the focal stack, based on translation speed of the camera.

After the registration process is completed, the images are ready for a traditional focus measure operation and conversion to a depth map [56]. However, since the object translated over 50% of the FOV at most, only 50% of the focus stack can deliver useful depth information. Therefore, images from the multiple focus stacks need to be stitched for a larger FOV. When translating over slightly less than 50% of the FOV, there will be some overlap between images of consecutive stacks. Phase correlation can be used for registration and stitching [82, 116]. Registration on the frames with only a few pixels in focus proved difficult at full resolution. By first reducing the resolution of the images to a quarter of the original resolution, the correct transformation matrix for registration could be calculated. Figure 6.5 presents the process of stitching two stacks before applying the focus measure operation.

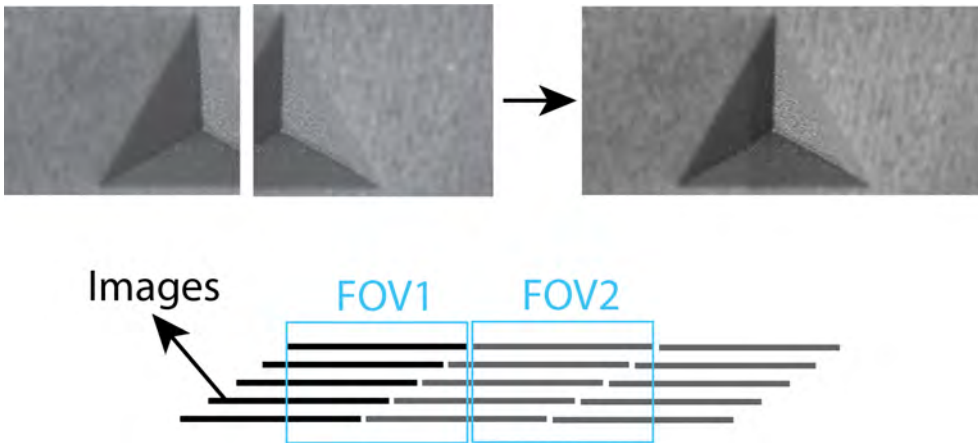


Figure 6.5: Stitching images of multiple stacks using phase correlation before focus measuring for full FOV measurements.

6.2.3 Experimental setup

In order to validate whether the proposed method has an impact on the quality of the produced depth maps, an experiment is designed. One of the features of the measurement target as presented in Subsection 2.4.6, a tetrahedron with a 10 mm base and a height of 8.165 mm, is measured with the camera in a stationary position as well as in a scanning motion using the proposed method (Figure 6.6).

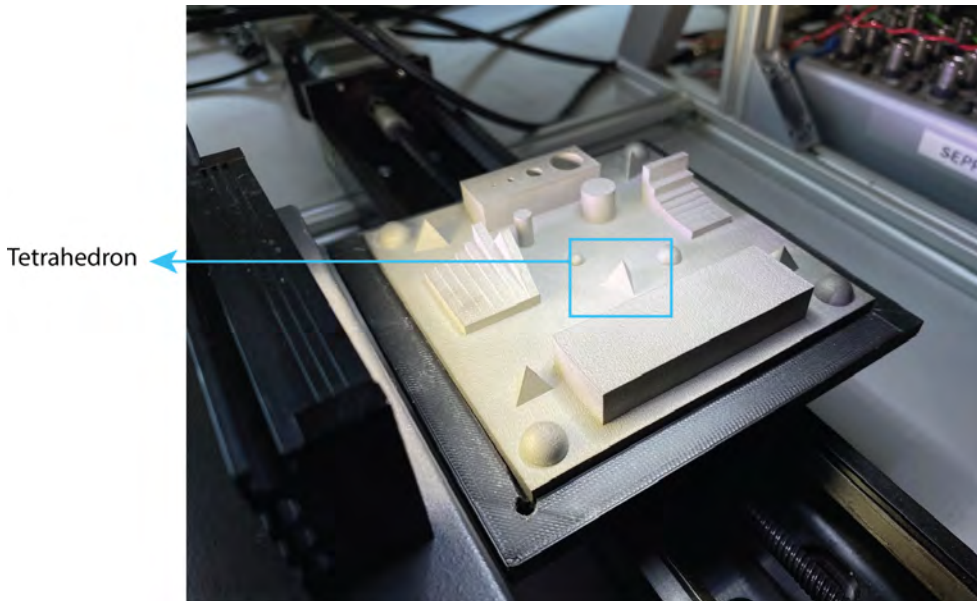


Figure 6.6: The calibration target and the tetrahedron feature that is used to validate the proposed method.

The quality comparison between the depth maps is then executed based upon the analytical measures Root-Mean-Square-Error (RSME), Correlation Coefficient (CORR) and Peak-Signal-to-Noise-Ratio (PSNR) [71, 79, 41, 87]. Both depth maps will contain the same sections of the calibration target and will be compared to a reference. A reference for the exact form of the 3D-printed tetrahedron is not available, so a true comparison is difficult. It would require a higher precision instrument to obtain an accurate reference measurement, and that measurement would also not be completely free of measurement errors. Therefore, we opted to use a depth map generated from the calibration target's CAD file for the analysis. Comparing the measurements to the CAD design of the part does not result in the true errors introduced by the measurement method. This comparison also includes the deviations in the 3D-printed PCT caused by the printing process. Therefore it is crucial to approach the interpretation of the measurement results with care. Since the deviations of the printing process are equal for both measurements, one can assume that the degradation of the depth map quality, between the stationary measurement method and the scanning method, can be attributed to the measurement method. The results of this experiment are discussed in the following section.

6.3 Results and discussion

Figure 6.7 shows the recovered depth maps of both the stationary method as well as the proposed scanning method. Compared to the reference, both maps look very similar. However, on the map from the scanning SFF method, more noise is visibly noticeable and some warping on the edge of the tetrahedron can be observed. This will result in some degradation compared to the stationary SFF method.

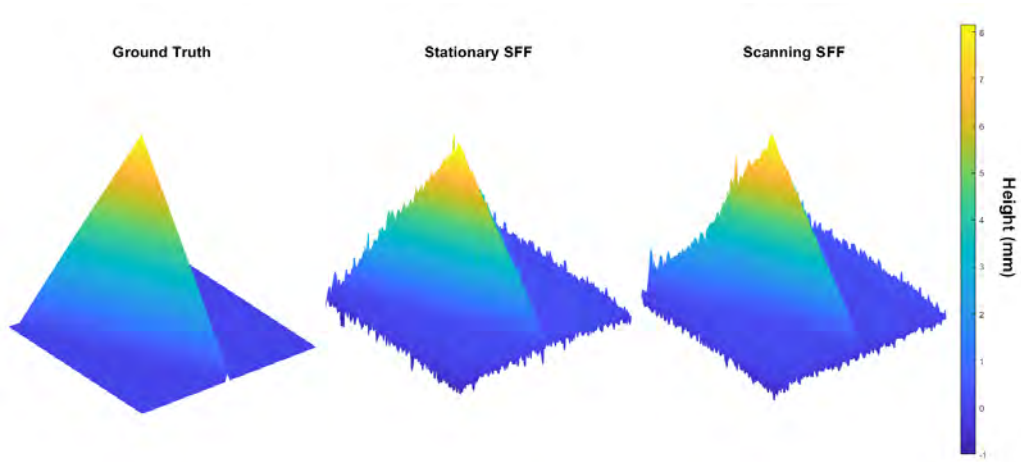


Figure 6.7: Depth map of the CAD design of the PCT and the recovered depth maps using the stationary SFF method and the proposed scanning SFF method.

From the graph in Figure 6.8, it is clear that the proposed method causes some additional degradation. The graph represents the analytical comparison between the reference, which is an extract from the CAD design, the stationary SFF method (1), and the proposed scanning method (2). Since the comparison is made to the CAD design, the measured degradation is, as explained, a combination of errors introduced by the 3D printing process of the PCT and errors introduced by the measurement. Since the errors from the 3D printing process and the optical aberrations of the measurement system are the same for both measurements, the degradation between the stationary SFF and scanning SFF measurement shows the degradation due to the new measuring method. The root-mean-square-error (RSME) degrades by 0.1 mm or 1.22%, relative to the height of the object, and the correlation between the measurement and the reference degrades by just 0.62%. This shows that the impact of the method is considered small.

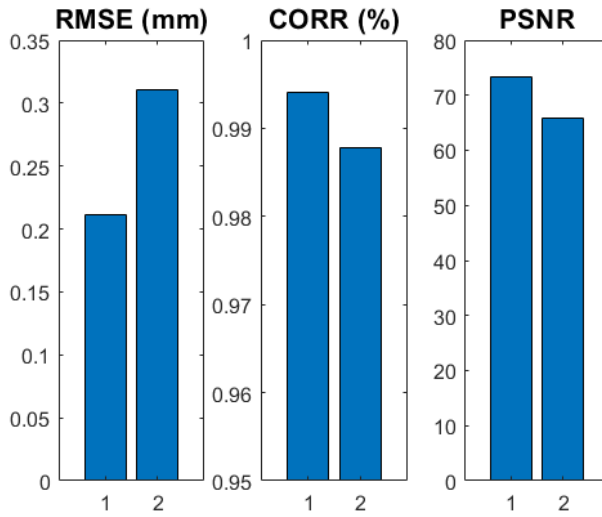


Figure 6.8: Analytical results of the average of 10 comparison measurements between the stationary SFF measurement (1), the scanning SFF measurement (2) and the reference.

Figure 6.9 contains the distribution of errors for each measurement point from the two measurements divided into six groups. From the bar graphs, one may notice that the proposed method introduces some additional errors because there are more points with a higher deviation from the reference.

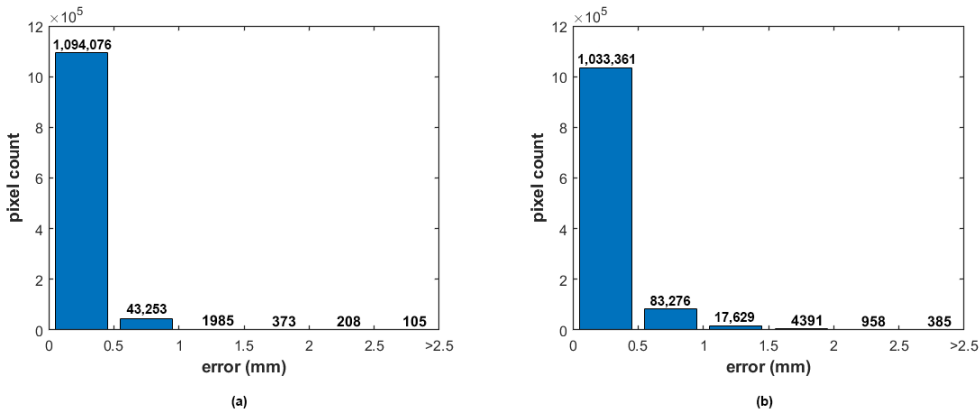


Figure 6.9: The distribution of errors for each measurement point for both the stationary (a) and scanning SFF (b) method. It also shows the degradation caused by the measurement method.

Looking at the difference map between the measurements and the reference (Figure 6.10), one may notice that most deviations with the proposed method are introduced at one side of the measurement. A possible cause of this could be the illumination that changes slightly during a scanning measurement. This can be caused by the oblique illumination

that was only added on the left side, another possible cause could be the perspective error of the finite conjugate microscope objective, a telecentric lens could then potentially solve that issue. More research is needed to discern the root cause of these deviations.

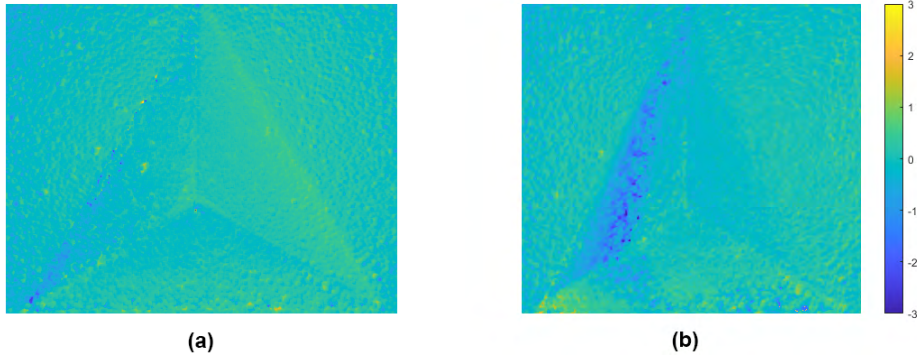


Figure 6.10: The error maps of both measurements, scaled between -3 mm and 3 mm deviation. (a) stationary measurement; (b) scanning measurement

These results suggest that the proposed method can potentially be used for the in-line control of 3D printers. However, like any other optical metrology solution, it has some limitations. One limitation of the method is the limited height measurement range compared to other methods. For μm precision measurements, the FOV needs to be small. Due to the optical design of most microscope objectives, higher magnification leads to a reduced focusing range of the ETL. Thus, the measurement resolution and range will always be a trade-off. The next limitation is the measurement speed. Although capable of measuring at speeds of 15 mm/s with the proposed components, for some applications this is not fast enough. As explained in Subsection 6.2.1, measurement speed and precision are also a trade-off.

6.4 Conclusion

A new method was proposed and introduced for using the shape-from-focus in continuous motion, such that it may be used for in-line additive manufacturing inspection. It uses a fast tunable lens controlled by an analogue signal, combined with a hardware-triggered camera. The method was tested by comparing the quality of a measurement using the proposed method with a stationary measurement, both measured with the same system. The measurement results demonstrate some degradation (1.22%) in measurement quality by applying the proposed method. From this, we can conclude that the method could be applicable for in-line inspection in 3D printing applications. The proposed method could also potentially be used for other applications, such as inspections of movable objects on conveyor belts or by extension any situation where the object is moving relative to the camera. Although this work proves that the method works, it has some practical limitations. First and foremost, there is a trade-off between speed and measurement precision. Secondly, occlusions may hinder part measurement, as is the

case with any optical inspection method. Lastly, the depth measurement range is mostly small compared to other 3D profilometry methods.

One prospect of future research is, the issue on the additional deviations in the measurements. The cause of the deviations needs to be researched. Another item to consider for future research is the possibility of improving the quality of the measurement by improving the alignment of the images in the focus volume. The current alignment is coarse because the motion of the translation stage that was used for the measurement is non-constant. This non-constant speed is introduced by the use of a stepper motor with flexible coupling. The alignment can potentially be improved by using phase correlation or other registration techniques. A further improvement of the method may be to include information from the CAD file of a previous or coarse measurement into the measurement process, similarly to the method described in Chapter 5. This adds a lot of complexity to the analog control of the tunable lens, in order to keep the relationship between the lens focus distance and the images.

General conclusions

7.1 Conclusions

Although the shape-from-focus profile metrology method has been proven to be accurate and precise enough to be utilised as a precision method for in-line or online additive manufacturing metrology, its time-consuming and discrete nature is not compatible with the process of AM. This research aimed to overcome these issues. To reach that goal, a custom tunable-lens-based SFF setup was built, multiple research steps were taken and different methods were developed. Combined, these developments and methodologies form a low-cost SFF system that is capable of measuring and processing SFF measurements in a continuous scanning motion at speeds comparable with current AM technology.

This research began with a comprehensive literature study of metrology methods in general. Chapter 1 underlined the potential of SFF as a non-contact, high-resolution measurement technique capable of capturing intricate surface details, rendering it particularly suited for the evaluation of complex geometries and fine features inherent to AM parts. However, this chapter also recognised the limitations of SFF, including the trade-off between acquisition time and precision. These insights laid the foundation for subsequent chapters, directing attention toward mitigating these limitations.

Subsequently, we dived into the fundamental principles of SFF, providing an essential knowledge base for successive developments. We carefully looked into the detailed aspects of creating a tunable lens-based SFF setup. This involved choosing components, fine-tuning parameters, and highlighting the crucial role of calibration and characterization to achieve reliable and precise measurements. Building the custom SFF setup allowed the study to encompass optics, camera technology, computer vision, and metrology.

Initially, a novel approach for data reduction based on phase correlation was introduced. The primary goal was to enhance the accuracy and noise resistance of depth map generation, surpassing the capabilities of established methods such as Gaussian fitting and centroid finding, while maintaining low computational complexity. In contrast to proposed accurate and noise-robust methods that require extensive model training or involve complex and inefficient computations. Experimental validation using synthetic and real-world data demonstrated the enhanced performance of the proposed phase correlation (PC) and shifted phase correlation (SPC) methods in terms of measurement accuracy and

robustness to noise. However, it also acknowledged a slight increase in computational complexity, in particular for the SPC method.

The computational burden associated with transforming a focus volume into a depth map using a computer's CPU was identified as a limitation of publicly accessible implementations of focus measure operators and SFF processing. Although the use of a computer's GPU has been established for decreasing processing time, integrating algorithms to leverage GPU processing can be intricate. However, the implementation of focus measure operators using PyTorch, a framework designed for neural networks with efficient GPU libraries, offered a solution without necessitating direct GPU programming. This resulted in an increase of 3.5 to 4.5 times in processing speed. Yet, the use of this framework also constrained the increase in processing speed.

Using the aforementioned developments, the duration of a single high-quality SFF measurement could be reduced considerably, enabling the measurement of a substantially large surface without excessively affecting the additive manufacturing process. Another approach to decrease the overall measurement time of large-area SFF measurements using a different measurement strategy was presented. This involved combining laser triangulation as a rapid yet coarse measurement technique with the precision of SFF in a two-step process, enabling dynamic adjustment and reduction of the SFF's focal range. While this method can optimise measurement time for diverse objects, the extent of time reduction depends on the complexity of the object and the measurement system parameters.

While the aforementioned advancements succeeded in decreasing the total measurement time through careful measurement planning, they still maintained the discrete character inherent in the current SFF method. The ultimate goal of the final development was to address this discrete nature, as it does not harmonise with the continuous motion inherent in additive manufacturing. By scanning the surface while measuring with the tunable-lens-based setup, essentially the same information is captured, yet arranged differently. To combine the scanning motion with the capturing and focusing, the tunable lens had to be controlled using an analogue staircase signal synchronised to a square wave trigger signal for the camera. After stitching and re-alignment of the focus volume, a similar 3D profile could be created compared to a traditional stationary measurement. While it has been proven that this method works, one of the identified weaknesses, was the increase in RSME and decrease in the overall quality of the measurement. The cause of this decrease was not researched, however, perspective error from the finite conjugate objective is suspected to be a possible cause.

By integrating the phase correlation processing method with GPU-based focus measurement and the continuous scanning approach, it becomes possible to significantly expedite the measurement process using the same setup, achieving an approximately 24-fold increase in speed. With the custom-built setup, measuring a 100 mm by 100 mm test sample typically required 425 sub-measurements, each taking about 10 seconds, resulting in a total measurement time of 4250 seconds, equivalent to 1 hour, 10 minutes, and 50 seconds, when using the slower discrete SFF method.

However, with the same setup scanning at a rate of 15 mm/s, it can measure the same area in 25 passes of 100 mm, with each pass taking approximately 7 seconds. This results in a significantly reduced total measurement time of approximately 175 seconds or nearly three minutes.

In general, this study enhances the progression of the SFF technique for its applications in additive manufacturing (AM) and concurrently presents viable answers to the complexities of dimensional metrology. For those new to SFF, this manuscript provides an initial guide to comprehending the method and its fundamental principles, enabling informed choices in the creation of SFF metrology systems. Future investigations could explore the practical implementation of SFF as an online metrology approach in AM.

7.2 Future work

While this research explored different methodologies to enhance SFF as a technique, several avenues for future investigation emerged. For instance, the methods proposed in this thesis were solely tested with two distinct focus measure operators and a limited range of kernel sizes, as exploring all potential methods and parameters would prove time-intensive. Additionally, the impact of post-processing on depth maps, such as noise reduction through guided image filters or point cloud simplification was not explored due to time constraints.

Additionally, at the time of writing, there is no obvious criterium to select the best FMO and ideal settings for a specific application, the approach we took was to evaluate the existing FMO's based on RSME of the output with respect to a reference. E.G., there could potentially be a relationship between the optimum kernel size and the surface roughness and texture of the material. This was not investigated during this research, thus could be an interesting prospect for future research. This research could also investigate the influence of the surface roughness on the measurements and compare that to alternative measurement methods.

It was mentioned in Subsection 2.4.3 that multiple types of illumination (ring light, coaxial lighting oblique illumination) can be used for SFF. Additionally it was mentioned that the wavelength of light used can influence the measurements. The contributions of these types of illumination and the wavelengths used on the accuracy of the measurements can be further optimized.

As mentioned in Chapter 4, improvements are likely to be made, by removing the CPU and CPU memory completely from the data chain when capturing and processing measurements. Directly capturing images using a frame grabber card and feeding the images directly into the GPU's memory can potentially gain vast amounts of processing time. Additionally as noted in Chapter 4, some FMOs might be better suited for implementation on GPU. This also presents an opportunity for future investigation.

The introduction of Chapter 6 notes the possibility to tilt the camera to implement a scanning method for SFF, while also eliminating the tunable lens. This has the potential to be an intriguing avenue for future investigation.

Another prospect for future exploration lies in the absence of a definitive method for determining the instrument transfer function (ITF) and consequently, the topographic spatial resolution of SFF devices. The current proposed methods for determination of the ITF, according to the literature, tend to deliver inconsistent results. A reliable ITF would facilitate the comparison of different instruments, parameters and measurement strategies.

The SFF method employed in this research relies on a tunable lens, requiring multiple images to be captured. An intriguing advancement could be a snapshot camera based on focus variation. One potential strategy could be to use chromatic aberration to our advantage. The wavelength-dependent focal distance of a lens typically induces chromatic aberration. Conventional lens designs incorporate various types of glass to mitigate this effect. When an objective's chromatic aberration can be characterized, a snapshot multi-spectral camera could potentially provide a solution for single shot shape from focus, as different wavelengths of light would focus on different heights. Exploring the feasibility of this approach would require in-depth research into optical design.

Although the experiments were conducted on a custom-built system, the absence of tests within an actual additive manufacturing (AM) machine leaves room for realistic validation of the proposed methods under more authentic conditions like higher temperature and possible vibrations. The high temperature and possible temperature fluctuations of a metal additive manufacturing machine may influence the focus levels of the tunable lens. Secondly, given the simplicity of the setup for SFF, the possibility can be explored to add the SFF setup (Camera and tunable lens) to an existing optical port of an additive manufacturing machine. During this research a method to interface the measurements system from an AM machine was tested. This interface involved sending binary signals from the AM machine to start and stop measurements and from the measurement system to the AM machine to provide status information. This approach can also be further explored.

As had been established, the selection of the camera and the optical components determine the accuracy of the measurement system. Thus, a single measurement system in an AM machine would be a compromise between fast and accurate 3D profiles of the printed objects. A better approach would be to implement two or more SFF camera systems each developed with a specific goal. E.g. fast, less accurate measurements for the overall shape measurements or slower but more accurate measurements for specific features of the build. Combining the measurements of multiple systems into a common point cloud is another topic that requires research.

Ultimately, for the integration of SFF as an online method for AM inspection, a critical step involves aligning and comparing measurements with computer-aided design (CAD) data. One large aspect of this integration is the method of displaying and saving measurement data. As it stands the current custom system has 1.3 million data points per FOV of 8 mm by 6 mm. Measuring larger areas then leads to enormous data files containing measurement information. A more sophisticated way to save measurement points with higher density around edges and features might bring a solution to this issue. Then there is the potential to adapt and optimise measurement strategies for inspection and fault detection, thus enhancing SFF's applicability and effectiveness in AM.

Bibliography

- [1] S. Nobuo and R. Peter, *Metrology Handbook: The Science of Measurement*. Mitutoyo (UK) ltd., 2 ed., 2016. 7
- [2] R. Leach, M. Ferrucci, and H. Haitjema, *Dimensional Metrology*, pp. 1–11. Berlin, Heidelberg, Germany: Springer, 2019 ed., 2020. 7
- [3] Bipm, “International vocabulary of metrology-basic and general concepts and associated terms (vim) 3rd edition,” tech. rep., Bipm, 2012. 7, 8
- [4] S. Shirmohammadi, L. Mari, and D. Petri, “On the commonly-used incorrect visual representation of accuracy and precision,” *IEEE Instrumentation & Measurement*, vol. 24, pp. 45–49, 2 2021. 8
- [5] ISO Central Secretary, “Geometrical product specifications (gps) - Calibration, adjustment and verification of areal topography measuring instruments,” standard, International Organization for Standardization, Geneva, CH, Mar. 2022. 8, 20, 36, 38, 40, 42
- [6] S. Sels, S. Vanlanduit, B. Bogaerts, and R. Penne, “Three-dimensional full-field vibration measurements using a handheld single-point laser Doppler vibrometer,” *Mechanical Systems and Signal Processing*, vol. 126, pp. 427–438, jul 2019. 10
- [7] T. Santoso, W. P. Syam, S. Darukumalli, and R. Leach, “Development of a compact focus variation microscopy sensor for on-machine surface topography measurement,” *Measurement*, vol. 187, p. 110311, jan 2022. 10, 89
- [8] M. A. Akhloufi, Y. Guyon, C. I. Castanedo, and A. Bendada, “Three-dimensional thermography for non-destructive testing and evaluation,” <http://dx.doi.org/10.1080/17686733.2016.1229245>, vol. 14, pp. 79–106, jan 2016. 10
- [9] J. L. Vilaça, J. C. Fonseca, and A. M. Pinho, “Non-contact 3D acquisition system based on stereo vision and laser triangulation,” *Machine Vision and Applications*, vol. 21, pp. 341–350, 2010. 10
- [10] B. Ribbens, S. Vanlanduit, J. J. J. Dirckx, and P. Cools, “Fringe projection simulation software for 3D shape measurements,” in *10th IMEKO Symposium Laser metrology for precision measurement and inspection in industry 2011*, pp. 185–191, 2011. 10, 89
- [11] S. Sels, *Linking real-world measurements and sensor data with 3D CAD models*. Antwerp: University of Antwerp, Faculty of Applied Engineering, 2019. 10, 89
- [12] B. Sun and B. Li, “A rapid method to achieve aero-engine blade form detection,” *Sensors (Switzerland)*, vol. 15, pp. 12782–12801, jun 2015. 10, 11, 79

- [13] X. Zhou, H. Zhao, and P. Zhang, "Optical 3D shape measurement for dynamic object using color fringe pattern projection and empirical mode decomposition," *Optical Measurement Systems for Industrial Inspection VI*, vol. 7389, no. June 2015, p. 73890D, 2009. 10
- [14] B. Ribbens, J. Peeters, B. Bogaerts, G. Steenackers, S. Sels, R. Penne, and G. V. Barel, "4d active and passive thermography measurement system using a kuka kr16 robot and time-of-flight imaging," in *13th Quantitative Infrared Thermography Conference*, pp. 670–677, 2016. 10
- [15] B. Bogaerts, R. Penne, S. Sels, B. Ribbens, and S. Vanlanduit, "A Simple Evaluation Procedure for Range Camera Measurement Quality," *Lecture Notes in Computer Science (including subseries Lecture Notes in Artificial Intelligence and Lecture Notes in Bioinformatics)*, vol. 10016 LNCS, pp. 286–296, oct 2016. 10
- [16] F. Menna, E. Nocerino, M. M. Nawaf, J. Seinturier, A. Torresani, P. Drap, F. Remondino, and B. Chemisky, "Towards real-time underwater photogrammetry for subsea metrology applications," *OCEANS 2019 - Marseille, OCEANS Marseille 2019*, vol. 2019-June, jun 2019. 10, 55
- [17] Z. Chen, H. Liao, and X. Zhang, "Telecentric stereo micro-vision system: Calibration method and experiments," *Optics and Lasers in Engineering*, vol. 57, pp. 82–92, jun 2014. 10
- [18] J. Gladines, S. Sels, J. Blom, and S. Vanlanduit, "A fast shape-from-focus-based surface topography measurement method," *Sensors*, vol. 21, apr 2021. 10, 70, 89
- [19] P. Favaro, S. Soatto, M. Burger, and S. J. Osher, "Shape from defocus via diffusion," *IEEE Transactions on Pattern Analysis and Machine Intelligence*, vol. 30, pp. 518–531, mar 2008. 10
- [20] F. J. Brosted, J. J. Aguilar, J. Santolaria, and R. Lázaro, "Geometrical Verification based on a Laser Triangulation System in Industrial Environment. Effect of the Image Noise in the Measurement Results," in *Procedia Engineering*, vol. 132, pp. 764–771, Elsevier Ltd, jan 2015. 10
- [21] N. Swojak, M. Wiczorowski, and M. Jakubowicz, "Assessment of selected metrological properties of laser triangulation sensors," *Measurement: Journal of the International Measurement Confederation*, vol. 176, may 2021. 10
- [22] P. Kienle, L. Batarilo, M. Akgül, M. H. Köhler, K. Wang, M. Jakobi, and A. W. Koch, "Optical Setup for Error Compensation in a Laser Triangulation System," *Sensors*, vol. 20, p. 4949, sep 2020. 10, 89
- [23] G. Genta, P. Minetola, and G. Barbato, "Calibration procedure for a laser triangulation scanner with uncertainty evaluation," *Optics and Lasers in Engineering*, vol. 86, pp. 11–19, nov 2016. 10, 89
- [24] W. Boehler and A. Marbs, "Investigating Laser Scanner Accuracy," *The International Archives of Photogrammetry Remote Sensing and Spatial Information Sciences*, vol. 34, pp. 696–701, 2003. 10, 89
- [25] Y. Hu, Q. Chen, S. Feng, and C. Zuo, "Microscopic fringe projection profilometry: A review," *Optics and Lasers in Engineering*, vol. 135, 12 2020. 11, 89

- [26] S. Van der Jeught and J. J. Dirckx, "Real-time structured light profilometry: a review," *Optics and Lasers in Engineering*, vol. 87, pp. 18–31, 2016. Digital optical & Imaging methods in structural mechanics. 11
- [27] S. V. der Jeught and J. J. J. Dirckx, "Real-time structured light-based otoscopy for quantitative measurement of eardrum deformation," *Journal of Biomedical Optics*, vol. 22, p. 1, 1 2017. 11
- [28] J. A. Buytaert, B. Ribbens, S. Vanlanduit, and J. J. Dirckx, "Aberration-free moiré profilometry—analysis, simulation and implementation of the optimal setup geometry," *Optics and Lasers in Engineering*, vol. 50, no. 8, pp. 1119–1129, 2012. Fringe Analysis Methods & Applications. 12
- [29] ISO Central Secretary, "Geometrical product specifications (gps) - Nominal characteristics of non-contact (focus variation) instruments," standard, International Organization for Standardization, Geneva, CH, Mar. 2015. 13, 34
- [30] A. P. Pentland, "A New Sense for Depth of Field," *IEEE Transactions on Pattern Analysis and Machine Intelligence*, vol. PAMI-9, no. 4, pp. 523–531, 1987. 13
- [31] M. Moeller, M. Benning, C. Schönlieb, and D. Cremers, "Variational Depth from Focus Reconstruction," *IEEE Transactions on Image Processing*, vol. 24, pp. 5369–5378, dec 2015. 13
- [32] F. Mahmood, M. T. Mahmood, and J. Iqbal, "3-D shape recovery from image focus using no-reference sharpness metric based on inherent sharpness," in *International Conference on Control, Automation and Systems*, vol. 2017-October, 2017. 13
- [33] L. Newton, N. Senin, C. Gomez, R. Danzl, F. Helmlí, L. Blunt, and R. Leach, "Areal topography measurement of metal additive surfaces using focus variation microscopy," *Additive Manufacturing*, vol. 25, pp. 365–389, jan 2019. 13
- [34] L. J. Angot-Petit, "Small scale surface profile recovery using a tunable lens based System," *IS and T International Symposium on Electronic Imaging Science and Technology*, pp. 39–48, 2017. 13, 35, 40
- [35] David Flack and John Hannaford, *Fundamental Good Practice in Dimensional Metrology*. National Physical Laboratory, 2009. 13
- [36] C. Bermudez, P. Martinez, C. Cadevall, and R. Artigas, "Active illumination focus variation," in *Optical Measurement Systems for Industrial Inspection XI* (P. Lehmann, W. Osten, and A. A. G. Jr., eds.), vol. 11056, p. 110560W, International Society for Optics and Photonics, SPIE, 2019. 14
- [37] Sensofar, "Sensofar s neox sensor," 2023. 14
- [38] S. K. Nayar, "Shape from focus system," in *Proceedings 1992 IEEE Computer Society Conference on Computer Vision and Pattern Recognition*, pp. 302–308, 1992. 19
- [39] P. Grossmann, "Depth from focus," *Pattern Recognition Letters*, vol. 5, pp. 63–69, 1 1987. 19
- [40] R. Danzl, F. Helmlí, and S. Scherer, "Focus variation - A robust technology for high resolution optical 3D surface metrology," *Strojnicki Vestnik/Journal of Mechanical Engineering*, vol. 57, no. 3, pp. 245–256, 2011. 19, 89

- [41] M. T. Mahmood, Y. K. Choi, and S. O. Shim, "Estimating shape from focus by Gaussian process regression," *Conference Proceedings - IEEE International Conference on Systems, Man and Cybernetics*, pp. 1345–1350, 2012. 24, 48, 54, 96
- [42] H. S. Jang, G. Yun, M. T. Mahmood, and M. K. Kang, "Optimal sampling for shape from focus by using gaussian process regression," *Digest of Technical Papers - IEEE International Conference on Consumer Electronics*, vol. 2020-Janua, pp. 2–5, 2020. 24, 48
- [43] S. Pertuz, D. Puig, and M. A. Garcia, "Analysis of focus measure operators for shape-from-focus," *Pattern Recognition*, vol. 46, no. 5, pp. 1415–1432, 2013. 25, 28, 56, 64, 89
- [44] M. Subbarao, T.-S. Choi, and A. Nikzad, "Focusing techniques," in *Machine Vision Applications, Architectures, and Systems Integration* (B. G. Batchelor, S. S. Solomon, and F. M. Waltz, eds.), vol. 1823, pp. 163 – 174, International Society for Optics and Photonics, SPIE, 1992. 25
- [45] A. Santos, C. O. D. Solórzano, J. J. Vaquero, J. M. Peña, N. Malpica, and F. D. Pozo, "Evaluation of autofocus functions in molecular cytogenetic analysis," *Journal of Microscopy*, vol. 188, pp. 264–272, 1997. 25
- [46] A. Eskicioglu and P. Fisher, "Image quality measures and their performance," *IEEE Transactions on Communications*, vol. 43, no. 12, pp. 2959–2965, 1995. 25
- [47] E. Krotkov and J.-P. Martin, "Range from focus," in *Proceedings. 1986 IEEE International Conference on Robotics and Automation*, vol. 3, pp. 1093–1098, 1986. 25
- [48] J. Pech-Pacheco, G. Cristobal, J. Chamorro-Martinez, and J. Fernandez-Valdivia, "Diatom autofocusing in brightfield microscopy: a comparative study," in *Proceedings 15th International Conference on Pattern Recognition. ICPR-2000*, vol. 3, pp. 314–317 vol.3, 2000. 25
- [49] S. K. Nayar, "Shape from focus," Tech. Rep. CMU-RI-TR-89-27, Carnegie Mellon University, Pittsburgh, PA, November 1989. 25
- [50] A. Thelen, S. Frey, S. Hirsch, and P. Hering, "Improvements in shape-from-focus for holographic reconstructions with regard to focus operators, neighborhood-size, and height value interpolation," *IEEE Transactions on Image Processing*, vol. 18, no. 1, pp. 151–157, 2009. 25
- [51] G. Yang and B. Nelson, "Wavelet-based autofocusing and unsupervised segmentation of microscopic images," in *Proceedings 2003 IEEE/RSJ International Conference on Intelligent Robots and Systems (IROS 2003) (Cat. No.03CH37453)*, vol. 3, pp. 2143–2148 vol.3, 2003. 25
- [52] H. Xie, W. Rong, and L. Sun, "Wavelet-based focus measure and 3-d surface reconstruction method for microscopy images," in *2006 IEEE/RSJ International Conference on Intelligent Robots and Systems*, pp. 229–234, 2006. 25
- [53] L. Firestone, K. Cook, K. Culp, N. Talsania, and K. Preston, "Comparison of autofocus methods for automated microscopy," *Cytometry*, vol. 12, pp. 195–206, 1991. 25

- [54] C.-H. Shen and H. Chen, "Robust focus measure for low-contrast images," in *2006 Digest of Technical Papers International Conference on Consumer Electronics*, pp. 69–70, 2006. 25
- [55] F. Helmlí and S. Scherer, "Adaptive shape from focus with an error estimation in light microscopy," in *ISPA 2001. Proceedings of the 2nd International Symposium on Image and Signal Processing and Analysis. In conjunction with 23rd International Conference on Information Technology Interfaces (IEEE Cat.)*, pp. 188–193, 2001. 25
- [56] S. Pertuz, "Shape From Focus." <https://nl.mathworks.com/matlabcentral/fileexchange/55103-shape-from-focus>, 2019. [Online; accessed 24-July-2019]. 25, 26, 49, 66, 67, 82, 83, 95
- [57] Leica, "Depth of field in microscopy," 2010. 33
- [58] L. Chen, M. Ghilardi, J. J. Busfield, and F. Carpi, "Electrically tunable lenses: A review," *Frontiers in Robotics and AI*, vol. 8, 6 2021. 35
- [59] ISO Central Secretary, "Geometrical product specifications (gps) - Metrological characteristics for areal topography measuring methods," standard, International Organization for Standardization, Geneva, CH, Mar. 2019. 37, 42
- [60] R. Leach, H. Haitjema, R. Su, and A. Thompson, "Metrological characteristics for the calibration of surface topography measuring instruments: A review," *Measurement Science and Technology*, vol. 32, 3 2020. 37
- [61] A. Alburayt, W. P. Syam, and R. Leach, "Lateral scale calibration for focus variation microscopy," *Measurement Science and Technology*, vol. 29, 5 2018. 39, 40
- [62] ISO Central Secretary, "Geometrical product specifications (gps) - surface texture: Part 2: Terms, definitions and surface texture parameters," standard, International Organization for Standardization, Geneva, CH, Mar. 2012. 42
- [63] P. J. de Groot, "The instrument transfer function for optical measurements of surface topography," *JPhys Photonics*, vol. 3, 4 2021. 43
- [64] V. V. Yashchuk, S. Babin, S. Cabrini, W. Chao, U. Griesmann, I. Lacey, S. Marchesini, K. Munechika, C. Pina-Hernandez, and A. Roginsky, "Binary pseudorandom array test standard optimized for characterization of large field-of-view optical interferometers," in *Interferometry XX* (M. B. N. Morris, K. Creath, and R. Porras-Aguilar, eds.), vol. 11490, p. 114900W, International Society for Optics and Photonics, SPIE, 2020. 43
- [65] M. Eifler, J. Hering, A. Keksel, G. Freymann, and J. Seewig, "Towards a continuous frequency band chirp material measure for surface topography measuring instrument calibration," in *Optical Measurement Systems for Industrial Inspection XII* (P. Lehmann, W. Osten, and A. A. G. Jr., eds.), vol. 11782, p. 117820M, International Society for Optics and Photonics, SPIE, 2021. 43
- [66] M. Eifler, J. Hering, J. Seewig, R. K. Leach, G. von Freymann, X. Hu, and G. Dai, "Comparison of material measures for areal surface topography measuring instrument calibration," *Surface Topography: Metrology and Properties*, vol. 8, p. 025019, may 2020. 43

- [67] C. L. Giusca and R. K. Leach, "Calibration of the scales of areal surface topography measuring instruments: part 3. resolution," *Measurement Science and Technology*, vol. 24, p. 105010, sep 2013. 43
- [68] B. Carrier, D. MacKinnon, L. Cournoyer, and J.-A. Beraldin, "Proposed nrc portable target case for short-range triangulation-based 3d imaging systems characterization," in *Three-Dimensional Imaging, Interaction, and Measurement*, vol. 7864, p. 78640L, SPIE, 1 2011. 44
- [69] B. Carrier, D. K. MacKinnon, and L. Cournoyer, "Performance evaluation of 3d imaging systems based on gd&t," *Manufacturing Letters*, vol. 1, pp. 9–12, 10 2013. 44
- [70] H. S. Jang, G. Yun, H. Mutahira, and M. S. Muhammad, "A new focus measure operator for enhancing image focus in 3D shape recovery," *Microscopy Research and Technique*, 2021. 47, 63
- [71] F. Memon, M. A. Unar, and S. Memon, "Image quality assessment for performance evaluation of focus measure operators," *Mehran University Research Journal of Engineering and Technology*, vol. 34, pp. 379–386, 4 2015. 47, 54, 96
- [72] H. G. Jeon, J. Surh, S. Im, and I. S. Kweon, "Ring difference filter for fast and noise robust depth from focus," *IEEE Transactions on Image Processing*, vol. 29, pp. 1045–1060, 2020. 47, 63
- [73] M. Subbarao and J. K. Tyan, "Selecting the optimal focus measure for autofocus and depth-from-focus," *IEEE Transactions on Pattern Analysis and Machine Intelligence*, vol. 20, no. 8, pp. 864–870, 1998. 48, 53
- [74] M. B. Ahmad and T. S. Choi, "Application of three dimensional shape from image focus in LCD/TFT displays manufacturing," *Digest of Technical Papers - IEEE International Conference on Consumer Electronics*, pp. 2–5, 2007. 48
- [75] S. K. Nayar and Y. Nakagawa, "Shape from Focus," *IEEE Transactions on Pattern Analysis and Machine Intelligence*, vol. 16, no. 8, pp. 824–831, 1994. 48, 49, 53, 63, 89, 94
- [76] M. Subbarao and T. Choi, "Accurate Recovery of Three-Dimensional Shape from Image Focus," *IEEE Transactions on Pattern Analysis and Machine Intelligence*, vol. 17, no. 3, pp. 266–274, 1995. 48, 94
- [77] S. A. Lee and B. G. Lee, "Three-dimensional shape recovery from image focus using polynomial regression analysis in optical microscopy," *Current Optics and Photonics*, vol. 4, no. 5, pp. 411–420, 2020. 48, 94
- [78] H. J. Kim, M. T. Mahmood, and T. S. Choi, "An efficient neural network for shape from focus with weight passing method," *Applied Sciences (Switzerland)*, vol. 8, no. 9, 2018. 48
- [79] S. A. Lee, H. S. Jang, and B. G. Lee, "Jitter elimination in shape recovery by using adaptive neural network filter," *Sensors*, vol. 19, no. 11, 2019. 48, 54, 96
- [80] Y. Frommer, R. Ben-Ari, and N. Kiryati, "Shape from focus with adaptive focus measure and high order derivatives," in *Proceedings of the British Machine Vision Conference (BMVC)*, pp. 134.1–134.12, BMVA Press, September 2015. 48, 53

- [81] K. Takita, T. Aoki, Y. Sasaki, T. Higuchi, and K. Kobayashi, "High-Accuracy Sub-pixel Image Registration Based on Phase-Only Correlation," *IEICE Transactions on Fundamentals of Electronics, Communications and Computer Sciences*, vol. E86-A, no. 8, pp. 1925–1934, 2003. 48, 50
- [82] H. Foroosh, J. B. Zerubia, and M. Berthod, "Extension of phase correlation to subpixel registration," *IEEE Transactions on Image Processing*, vol. 11, pp. 188–199, mar 2002. 48, 50, 95
- [83] A. Lamberti, S. Vanlanduit, B. De Pauw, and F. Berghmans, "A novel fast phase correlation algorithm for peak wavelength detection of fiber Bragg grating sensors," *Optics Express*, vol. 22, p. 7099, mar 2014. 48, 50
- [84] A. Alba, J. F. Viguera-Gomez, E. R. Arce-Santana, and R. M. Aguilar-Ponce, "Phase correlation with sub-pixel accuracy: A comparative study in 1d and 2d," *Computer Vision and Image Understanding*, vol. 137, pp. 76–87, 2 2015. 50
- [85] S. Pertuz, "Defocus simulation," 2016. 54
- [86] U. Ali, I. H. Lee, and M. T. Mahmood, "Guided image filtering in shape-from-focus: A comparative analysis," *Pattern Recognition*, vol. 111, p. 107670, mar 2021. 54
- [87] H. S. Jang, M. S. Muhammad, and T. S. Choi, "Optimizing image focus for shape from focus through locally weighted non-parametric regression," *IEEE Access*, vol. 7, pp. 74393–74400, 2019. 54, 96
- [88] Optotune, "Fast Electrically Tunable Lens EL-10-30 Series," 2019. 55, 77, 91
- [89] P. Favaro, "Shape from Focus / Defocus," *Computer*, vol. 16, no. 1, 1989. 63
- [90] M. I. Shah, S. Mishra, M. Sarkar, and C. Rout, "Identification of robust focus measure functions for the automated capturing of focused images from Ziehl–Neelsen stained sputum smear microscopy slide," *Cytometry Part A*, vol. 91, pp. 800–809, aug 2017. 63
- [91] J. L. Pech-Pacheco, G. Cristóbal, J. Chamorro-Martínez, and J. Fernández-Valdivia, "Diatom autofocusing in brightfield microscopy: A comparative study," *Proceedings - International Conference on Pattern Recognition*, vol. 15, no. 3, pp. 314–317, 2000. 63, 68
- [92] J. M. Geusebroek, F. Cornelissen, A. W. Smeulders, and H. Geerts, "Robust autofocusing in microscopy," *Cytometry*, vol. 39, no. 1, pp. 1–9, 2000. 63
- [93] C. Hazirbas, S. G. Soyer, M. C. Staab, L. Leal-Taixé, and D. Cremers, "Deep Depth from Focus," in *Lecture Notes in Computer Science (including subseries Lecture Notes in Artificial Intelligence and Lecture Notes in Bioinformatics)* (C. V. Jawahar, H. Li, G. Mori, and K. Schindler, eds.), vol. Computer V, pp. 525–541, Springer International Publishing, 2018. 63
- [94] H. Mutahira, M. S. Muhammad, M. Li, and D. R. Shin, "A simplified approach using deep neural network for fast and accurate shape from focus," *Microscopy Research and Technique*, vol. 84, pp. 656–667, 2021. 63, 89

- [95] Y. Chen, Y. Xie, L. Song, F. Chen, and T. Tang, "A Survey of Accelerator Architectures for Deep Neural Networks," *Engineering*, vol. 6, no. 3, pp. 264–274, 2020. 64
- [96] S. W. Smith, *The Scientist and Engineer's Guide to Digital Signal Processing*. California Technical Publishing, 1997. 64
- [97] Z. A. Memon, F. Samad, Z. R. Awan, A. Aziz, and S. S. Siddiqi, "CPU-GPU Processing CPU-GPU Processing," *International Journal of Computer Science and Network Security*, vol. 17, no. September, 2017. 65
- [98] X. Chen, Y. Qiu, and H. Yi, "Implementation and performance of image filtering on GPU," *Proceedings of the 2013 International Conference on Intelligent Control and Information Processing, ICICIP 2013*, pp. 514–517, 2013. 65, 75
- [99] B. N. M. Reddy, "Performance Analysis of GPU V/S CPU for Image Processing Applications," *International Journal for Research in Applied Science and Engineering Technology*, vol. V, pp. 437–443, feb 2017. 65
- [100] O. Fialka and M. Čadík, "FFT and convolution performance in image filtering on GPU," in *IV '06: Proceedings of the conference on Information Visualization*, (Washington, DC, USA), pp. 609–614, IEEE Computer Society, 2006. 65, 75
- [101] A. Paszke, S. Gross, F. Massa, A. Lerer, J. Bradbury, G. Chanan, T. Killeen, Z. Lin, N. Gimelshein, L. Antiga, A. Desmaison, A. Kopf, E. Yang, Z. DeVito, M. Raison, A. Tejani, S. Chilamkurthy, B. Steiner, L. Fang, J. Bai, and S. Chintala, "Pytorch: An imperative style, high-performance deep learning library," in *Advances in Neural Information Processing Systems 32*, pp. 8024–8035, Curran Associates, Inc., 2019. 65
- [102] NVIDIA, *Cuda C Programming Guide*. Nvidia Inc., 2015. 66
- [103] M. S. Nixon and A. S. Aguado, "Chapter 4 - low-level feature extraction (including edge detection)," in *Feature Extraction & Image Processing for Computer Vision (Third Edition)* (M. S. Nixon and A. S. Aguado, eds.), pp. 137–216, Oxford: Academic Press, third edition ed., 2012. 68
- [104] Movimed, "What is laser triangulation?." <https://www.movimed.com/knowledgebase/what-is-laser-triangulation/>, 2020. [Online; accessed 07-August-2020]. 78
- [105] D. Girardeau-Montaut, M. Roux, R. Marc, and G. Thibault, "Change detection on points cloud data acquired with a ground laser scanner," in *International Archives of the Photogrammetry, Remote Sensing and Spatial Information Sciences - ISPRS Archives*, vol. 36, 2005. 84
- [106] Y. D. Rajendra, S. C. Mehrotra, K. V. Kale, R. R. Manza, R. K. Dhumal, A. D. Nagne, D. Vibhute, S. Ramanujan, and G. Chair, "Evaluation of partially overlapping 3d point cloud's registration by using icp variant and cloudcompare," in *The International Archives of Photogrammetry, Remote Sensing and Spatial Information Sciences*, pp. 891–897, 2014. 84
- [107] G. May and D. Kiritsis, "Zero defect manufacturing strategies and platform for smart factories of industry 4.0," *Lecture Notes in Mechanical Engineering*, pp. 142–152, 2019. 89

- [108] F. S. Freeman, L. Chechik, and I. Todd, "Beat the machine (learning): metal additive manufacturing and closed loop control," *Physics Education*, vol. 55, p. 055012, 7 2020. 89
- [109] F. J. M. Rivera and A. J. R. Arciniegas, "Additive manufacturing methods: techniques, materials, and closed-loop control applications," *International Journal of Advanced Manufacturing Technology*, vol. 109, pp. 17–31, 7 2020. 89
- [110] V. Renken, L. Lübbert, H. Blom, A. V. Freyberg, and A. Fischer, "Model assisted closed-loop control strategy for selective laser melting," *Procedia CIRP*, vol. 74, pp. 659–663, 2018. 89
- [111] S. Onogi, T. Kawase, T. Sugino, and Y. Nakajima, "Investigation of shape-from-focus precision by texture frequency analysis," *Electronics (Switzerland)*, vol. 10, 8 2021. 89
- [112] U. Ali and M. T. Mahmood, "Energy minimization for image focus volume in shape from focus," *Pattern Recognition*, vol. 126, 6 2022. 89
- [113] A. Olszak, "Lateral scanning white-light interferometer," *Appl. Opt.*, vol. 39, pp. 3906–3913, Aug 2000. 90
- [114] M. F. Erinosh, E. T. Akinlabi, and O. T. Johnson, "Effect of scanning speed on the surface roughness of laser metal deposited copper on titanium alloy," *Materials Research*, vol. 22, 2019. 91
- [115] Thorlabs, "12 mm (0.47") motorized translation stages." https://www.thorlabs.com/newgrouppage9.cfm?objectgroup_id=2163. Accessed: 04-07-2022. 92
- [116] C. D. Kuglin and D. C. Hines, "The phase correlation image alignment method," in *Proc. of Intl. Conf. on Cybernetics and Society*, pp. 163–165, 1975. 95

